8-2000

Laser Spark Ignition Modeling

Ivan George Dors
University of Tennessee - Knoxville

To the Graduate Council:

I am submitting herewith a dissertation written by Ivan George Dors entitled "Laser Spark Ignition Modeling." I have examined the final electronic copy of this dissertation for form and content and recommend that it be accepted in partial fulfillment of the requirements for the degree of Doctor of Philosophy, with a major in Physics.

Dr. Christian G. Parigger, Major Professor

We have read this dissertation and recommend its acceptance:

Dr. James W. L. Lewis, Dr. Lloyd M. Davis, Dr. Horace W. Crater, Dr. Dennis R. Keefer

Accepted for the Council:

Carolyn R. Hodges

Vice Provost and Dean of the Graduate School

(Original signatures are on file with official student records.)

To the Graduate Council:

I am submitting herewith a dissertation written by Ivan George Dors entitled "Laser Spark Ignition Modeling." I have examined the final copy of this dissertation for form and content and recommend that it be accepted in partial fulfillment of the requirements for the degree of Doctor of Philosophy, with a major in Physics.

Dr. Christian G. Parigger, Major Professor

We have read this dissertation
and recommend its acceptance:

Dr. James W. L. Lewis

Dr. Lloyd M. Davis

Dr. Horace W. Crater

Dr. Dennis R. Keefer

Accepted for the Council:

Dr. Anne Mayhew

Interim Vice Provost and
Dean of The Graduate School

(Original signatures are on file in the Graduate Admissions and Records Office.)

LASER SPARK IGNITION MODELING

A Dissertation
Presented for the
Doctor of Philosophy Degree
The University of Tennessee, Knoxville

Ivan George Dors
August 2000

Dedication

To my parents

Acknowledgements

I would like to thank the people who contributed to this work. To start, I would like to thank Dr. C. G. Parigger and Dr. J. W. L. Lewis for the opportunities given to me at the UTSI Center for Laser Applications. Their guidance, enthusiasm, and friendship were much appreciated. I would also like to thank Dr. D. Plemmons, Dr. Y.-L. Chen, and Dr. W. Qin for their experimental investigations, without which this dissertation would not have been possible. Finally, I would like to thank my parents, Tom and Claire, and my brother, Eric, for their invaluable support throughout my academic career.

This dissertation is based on work that is in part supported by the National Science Foundation under Grant No. CTS-9512489, a UTSI graduate research assistantship, and a NASA space grant fellowship.

Abstract

Laser spark phenomena are studied in air and ammonia-oxygen mixtures by the use of a two-dimensional, axially-symmetric, time-accurate computational fluid dynamic model. The initial laser spark temperature distribution is generated to simulate a post-breakdown profile that is consistent with theoretical, experimental, and computational investigations for a nominal 10-ns optical breakdown laser pulse. Thermodynamic properties of various species are extended to 35,000 K to cover the range of the initial temperature distribution. The developed computational model includes a kinetics mechanism that implements plasma equilibrium kinetics in ionized regions, and non-equilibrium, multi-step, finite-rate reactions in non-ionized regions.

The computational model time-accurately predicts species concentrations, free electron number density decay, blast wave formation and propagation, vortex formations, temperature profiles, ignition kernel dynamics, flame front formation and propagation, and flow field interactions of laser spark decay in various non-combustible and combustible gaseous mixtures. The computationally predicted fluid phenomena are shown to agree with various flow patterns characteristic of laser spark decay by direct comparison with experimental records.

Contents

1 Introduction **1**

2 Laser Spark Properties **6**

2.1 Temperature Profile 6

2.2 Thermodynamic Properties 9

2.3 Species Concentrations 18

2.4 Transport Properties 26

3 Computational Modeling **32**

3.1 Transport Equations 32

3.2 Discretization Methods 35

3.3 Solution Methods 39

3.4 Kinetic Mechanisms 41

3.5 Computational Domain 45

3.6 Initial Conditions 48

4 Laser Spark Decay in Air **50**

4.1 Pressure Decay 50

4.2 Kernel Dynamics 58

4.3 Blast Wave Propagation 66

4.4 Shadowgraph Comparison 76

5 Laser Spark Decay in Ammonia-Oxygen Mixtures **83**

5.1 Stoichiometric Laser Spark Ignition 84

5.2 Equivalence Ratio Dependence 89

5.3 Experimental Comparison 96

6 Summary **100**

References **106**

Vita **112**

List of Figures

1 Initial temperature profile representing the energy deposition of the laser pulse subsequent to laser pulse termination. Spatial dimensions along the optic (horizontal) axis and the axis perpendicular are in units of meters. The temperature values are in units of Kelvin. 7

2 Calculated molar specific heat divided by the ideal gas constant for H and H^+ plotted with the least-square fit. The calculated value for H^+ is not visible due to the overlay of the H^+ fit. Temperature values are in units of Kelvin. 13

3 Calculated molar specific heat divided by the ideal gas constant for N, N^+, and N^{++} plotted with the least-square fit. Temperature values are in units of Kelvin. 14

4 Calculated molar specific heat divided by the ideal gas constant for O, O^+, and O^{++} plotted with the least-square fit. Temperature values are in units of Kelvin. 15

5 The molar specific heat divided by the ideal gas constant for H_2, N_2, and O_2 plotted with the least-square fit. Temperature values are in units of Kelvin. 16

6 The molar specific heat divided by the ideal gas constant for NO, OH, and NH plotted with the least-square fit. Temperature values are in units of Kelvin. 17

7 Initial species number densities contained in a laser spark in air subsequent to laser pulse termination. The number density values are plotting in units of particles per cubic meter. The temperature values are in units of Kelvin. 22

8 Initial species number densities contained in a laser spark in a 0.93:1.0 molar mixture of ammonia and oxygen subsequent to laser pulse termination. The number density values are plotting in units of particles per cubic meter. The temperature values are in units of Kelvin. . . . 23

9 Initial pressure profile including ionization and dissociation effects of air subsequent to laser pulse termination. Spatial dimensions along the x-axis (horizontal) and the axis perpendicular are in units of meters. The pressure values are in units of pascals. 24

10 Initial pressure profile including ionization and dissociation effects of a 0.93:1.0 molar mixture of ammonia and oxygen subsequent to laser pulse termination. Spatial dimensions along the x-axis (horizontal) and the axis perpendicular are in units of meters. The pressure values are in units of pascals. 25

11 Viscosity of high-temperature hydrogen, nitrogen, and oxygen gas at 101,325 Pa including dissociation and ionization effects[1]. Viscosity values are in units of kg/m/s. Temperatures values are in units of Kelvin. 28

12 Viscosity of various high-temperature ammonia-oxygen mixtures at 101,325 Pa including dissociation and ionization effects. The homogeneous hydrogen, nitrogen, and oxygen viscosity values are taken from Boulos et al.[1]. Viscosity values are in units of kg/m/s. Temperature values are in units of Kelvin. 29

13 The computational domain at initial size. Boundaries A-C are kept with a constant temperature of 298 K, a constant pressure of 101,325 Pa, and a constant gas concentration depending on the particular simulation. Boundary D coincides with the optic axis (x-axis) and is the line of axial symmetry. The 150 by 75 grid used in the simulations are shown. The distances on the x-axis and the y axis are in units of meters. 46

14 Computationally predicted pressure profile of laser spark decay in air at 100 ns in time. The velocity direction field is represented by arrows. Spatial dimensions along the x-axis are in the units of meters; the vertical dimension shares the same scale. The pressure values displayed are in units of pascals. 52

15 Computationally predicted pressure profile of laser spark decay in air at 1.8 μs in time. The velocity direction field is represented by arrows. The lower graph is the gas pressure [Pa] along the x-axis. Spatial dimensions along the x-axis are in the units of meters; the vertical dimension shares the same scale. The pressure values displayed are in units of pascals. 53

16 Computationally predicted velocity field of laser spark decay in air at 5.6 μs in time. The velocity direction field is represented by arrows. Spatial dimensions along the x-axis are in the units of meters; the vertical dimension shares the same scale. The velocity values displayed are in units of meters/second. 55

17 Computationally predicted velocity field of laser spark decay in air at 32 μs in time. The velocity direction field is represented by arrows. Spatial dimensions along the x-axis are in the units of meters; the vertical dimension shares the same scale. The velocity values displayed are in units of meters/second. 56

18 Computationally predicted velocity field of laser spark decay in air at 1.0 ms in time. The velocity direction field is represented by arrows. Spatial dimensions along the x-axis are in the units of meters; the vertical dimension shares the same scale. The velocity values displayed are in units of meters/second. 57

19 Computationally predicted temperature profile of laser spark decay in air at 100 ns in time. The velocity direction field is represented by arrows. Spatial dimensions along the x-axis are in the units of meters; the vertical dimension shares the same scale. The temperature values displayed are in units of Kelvin. 59

20 Computationally predicted temperature profile of laser spark decay in air at 1.8 μs in time. The velocity direction field is represented by arrows. Spatial dimensions along the x-axis are in the units of meters; the vertical dimension shares the same scale. The temperature values displayed are in units of Kelvin. 60

21 Computationally predicted temperature profile of laser spark decay in air at 5.6 μs in time. The velocity direction field is represented by arrows. Spatial dimensions along the x-axis are in the units of meters; the vertical dimension shares the same scale. The temperature values displayed are in units of Kelvin. 61

22 Computationally predicted temperature profile of laser spark decay in air at 32 μs in time. The velocity direction field is represented by arrows. Spatial dimensions along the x-axis are in the units of meters; the vertical dimension shares the same scale. The temperature values displayed are in units of Kelvin. 63

23 Computationally predicted temperature profile of laser spark decay in air at 1.0 ms in time. The velocity direction field is represented by arrows. Spatial dimensions along the x-axis are in the units of meters; the vertical dimension shares the same scale. The temperature values displayed are in units of Kelvin. 64

24 Temporal plot of the maximum kernel temperature predicted during laser spark decay in air. Temperature values are in units of Kelvin. Temporal values are in units of seconds. 65

25 Temporal plot of the maximum kernel electron number density predicted during laser spark decay in air. Number density values are in units of inverse cubic meters. Temporal values are in units of seconds. 67

26 Comparison of the predicted blast wave radius (black line) with experimental measurements (circles with error bars)[2]. The red lines represent a one-cell-width deviation from the predicted blast wave radius. Blast wave radii are in units of meters. Temporal values are in units of seconds. 69

27 Temporal evolution of the blast front asymmetry quantified by the dimensionaless parameter A (see Equation 64). Temporal values are in units of seconds. 72

28 Pressure history of the point located at the origin of the x-axis and y-axis. Pressure values are in units of pascals. Temporal values are in units of seconds. 75

29 Experimental (top) and computationally predicted synthetic (bottom) shadowgraph of laser spark decay in air at 5 μs in time. 78

30 Experimental (top) and computationally predicted synthetic (bottom) shadowgraph of laser spark decay in air at 100 μs in time. 80

31 Experimental (top) and computationally predicted synthetic (bottom) shadowgraph of laser spark decay in air at 500 μs. 81

32 The molar concentration profile of H_2O at 100 ns. The bottom graph depicts the temperature along the x-axis in units of Kelvin. The distances on the x-axis and the y axis are in units of meters. 85

33 The static enthalpy profile at 2.4 μs. Enthalpy values are in units of J/kg. The distances on the x-axis are in units of meters; the vertical dimension shares the same scale. 87

34 The molar concentration profile of H_2O at 5.6 μs. The bottom graph depicts the temperature along the x-axis in units of Kelvin. The distances on the x-axis and the y axis are in units of meters. 88

35 The molar concentration profile of H_2O at 32 μs. The velocity direction field is represented by arrows. The bottom graph depicts the temperature along the x-axis in units of Kelvin. The distances on the x-axis and the y axis are in units of meters. 90

36 The molar concentration profile of H_2O at 1.0 ms. The velocity direction field is represented by arrows. The bottom graph depicts the temperature along the x-axis in units of Kelvin. The distances on the x-axis and the y axis are in units of meters. 91

37 Simulated NH concentration (left), OH concentration (middle), and temperature profiles(right) for laser spark decay in an ammonia-oxygen mixture with an equivalence ratio of 0.1. The boundaries of each picture measures 7 mm square. The rows represent 3.2 μs, 10 μs, 32 μs, and 100 μs, respectively. All values are scaled for each profile to span the entire pseudo-color scale. Peak values are displayed on top of each profile with concentration in units of 10^{21} m^{-3} and temperature in units of Kelvin. 93

38 Simulated NH concentration (left), OH concentration (middle), and temperature profiles(right) for laser spark decay in an ammonia-oxygen mixture with an equivalence ratio of 0.7. The boundaries of each picture measures 7 mm square. The rows represent 3.2 μs, 10 μs, 32 μs, and 100 μs, respectively. All values are scaled for each profile to span the entire pseudo-color scale. Peak values are displayed on top of each profile with concentration in units of 10^{21} m^{-3} and temperature in units of Kelvin. 94

39 Simulated NH concentration (left), OH concentration (middle), and temperature profiles(right) for laser spark decay in an ammonia-oxygen mixture with an equivalence ratio of 1.0. The boundaries of each picture measures 7 mm square. The rows represent 3.2 μs, 10 μs, 32 μs, and 100 μs, respectively. All values are scaled for each profile to span the entire pseudo-color scale. Peak values are displayed on top of each profile with concentration in units of 10^{21} m^{-3} and temperature in units of Kelvin. 95

40 Experimental OH concentration profiles for laser-ignition of ammonia-oxygen mixtures with fuel equivalence ratios of 0.1 (left), 0.7 (middle), and 1.0(right). The boundaries of each picture measures 7 mm square. The rows represent 3 μs, 10 μs, 30 μs, and 100 μs, respectively.[3] . . 97

41 Experimental NH concentration profiles for laser-ignition of ammonia-oxygen mixtures with fuel equivalence ratios of 0.7 (left) and 1.0(right). The boundaries of each picture measures 7 mm square. The rows represent 3 μs, 10 μs, 30 μs, and 100 μs, respectively.[3, 4] 99

List of Tables

1 The ionization molar energies of H, N, and O [MJ/mol].[5] 10

2 Equilibrium species mole fractions at various temperatures and a pressure of 101,325 Pa. The initial mixture was composed with NH_3 and O_2 mole fractions of 0.48 and 0.52, respectively. The upper values for each species are calculated by this work, while the lower values are the result of the CEA code. Mole fraction values less than 10^{-10} are reported as zero. 20

3 The generalized scalar flow variable, ϕ, effective diffusivity, Γ, and the source term ,S_ϕ, evaluations for the mass, momentum, and energy transport equations to take the form of the generalized transport equation (Equation 38). 35

4 Arrhenius coefficients used in the forward N_2-O_2 reaction rates for laser spark decay simulation in air.[6] Reverse rate coefficients are determined by the law of mass action. Values of the A-coefficient are in units of $m^3/kmol/s/K^\beta$ for bi-molecular reactions and $m^6/kmol^2/s/K^\beta$ for tri-molecular reactions. Values of E_a/R are in 1/K. β is a dimensionless constant. 42

5 Arrhenius coefficients used in the first 15 forward and reverse reaction rates of the NH_3-O_2 mechanism.[7] Values of the A-coefficient are in units of $m^3/kmol/s/K^\beta$ for bi-molecular reactions and $m^6/kmol^2/s/K^\beta$ for tri-molecular reactions. Values of E_a/R are in 1/K. β is a dimensionless constant. 43

6 Arrhenius coefficients used in the second 15 forward and reverse reaction rates of the NH_3-O_2 mechanism.[7] Values of the A-coefficient are in units of $m^3/kmol/s/K^\beta$ for bi-molecular reactions and $m^6/kmol^2/s/K^\beta$ for tri-molecular reactions. Values of E_a/R are in 1/K. β is a dimensionless constant. 44

7 The numerically evaluated relation between the dimensionless radius (l) and dimensionless time (τ)of the Sedov blast wave model including counter-pressure (P_0). 73

1 Introduction

The 1963 discovery of the electrical breakdown of gas by laser radiation opened up many possibilities in the field of ignition. The electrodeless spark generation overcomes inhibition to flow, heat removal, and contamination of the chemistry common to electrode sparks. Additionally, the variety of optical focusing elements available allow for the optimization of the spark geometry, position, and number of ignition locations for a given volume of interest. Extensive laser ignition experiments have been performed with nominal 10 ns laser pulse [2–4, 8] induced plasmas. The challenge of this dissertation is to develop a computational model that simulates the fluid dynamic and chemical kinetic effects that span the 1 ms subsequent to termination of the laser pulse, with the resolution of space spanning 10^{-11} m^3 to 10^{-1} m^3.

The ability to tailor the spark geometry allows for an optimization of the fluid dynamic spark decay phenomena to the specific application. An example application is the Lightcraft being constructed by the Air Force Research Laboratory Propulsion Directorate and NASA Marshall Space Flight Center. The Lightcraft is propelled by a ground-based laser and is proposed to provide an inexpensive ($\sim$\$200/kg) means to get small payloads into low Earth orbit. Without fuel ignition, the propulsion is solely provided by the fluid dynamic force produced during the laser spark decay. An optimally designed focusing system would produce a spark giving the best propulsion for a particular ground based laser system and Lightcraft design.

The tailoring of the spark position is an important characteristic for the re-ignition

of jet engines. If a jet engine loses its flame at high-altitude, it must drop in altitude until the proper fuel-air mixture reaches the spark plug located on the combustion chamber, wall. This potentially dangerous and untimely maneuver may be avoided by the use of a laser spark positioned at the center of the combustion chamber where the ignitable fuel-air mixture is located. Additionally, it is possible that such a spark may be used as a clean pilot source during the normal engine operation and be integrated as part of a control loop to dampen the combustion instabilities.

The possible benefits of a laser spark-plug in an internal combustion (IC) engine appear very promising. In an IC engine, the electrodes of the spark plug are typically located just below the engine head and are timed to discharge just before the piston reaches top-dead-center. A laser spark plug would not only be able to produce a spark optimum to the cylindrical geometry, but also would allow for the possibility of several sparks at various locations adjusted for the particular driving conditions. The energies and the pulse times of the laser sparks can be orders of magnitude less than those of electrode sparks. With such characteristics, it is thought that laser sparks would provide a cleaner burn with less harmful emissions. Additionally, the asymmetric laser spark (as opposed to the cylindrically symmetric electrode spark) decays in a manner in which less energy is dissipated by the blast wave formation, and the flame front of the ignition kernel has a larger area per unit volume. The larger flame-front area-to-volume ratio lowers the optimal combustion mixture to the fuel-lean side of stoichiometric.

To predict the optimal laser spark geometry and position(s) for a given application, computational models that agree with experimental measurements of the simplest of cases must first be devised. Experimentally it has been shown that a 10 ns, 1064 nm Nd:YAG laser pulse with 25 mJ of energy focused by a 10 cm focal length lens can initiate optical breakdown in air and ammonia-oxygen gases. The manner in which the laser energy is deposited onto the optically-thick plasma results in the formation of a cylindrically-asymmetric spark. The plasma produced in this process has peak values of temperature, pressure, and electron number density on the order of 35,000 K, 5×10^7 Pa, and 5×10^{19} cm^{-3}, respectively. These values, however, will vary depending on the specific breakdown gas. The specific characteristics of the laser energy deposition are required for the proper description and simulation of the induced fluid dynamics in all regions of the spark decay and laser ignition processes over time. The computational simulations to this point have assumed spherical or cylindrical symmetry and use the unrealistic self-similar Taylor-Sedov equation for determining the initial temperature, pressure, density, and bulk velocities. The main experimental and computational focus has been on the blast wave propagation.

The 1970's oil crisis and increased computational abilities have prompted several investigations to try to model the experimentally observed kernel dynamics of electrode sparks[9–13]. Despite the various successes of these electrode spark decay models, the initial conditions used often have unrealistic aspects such as fluid gradients[9, 10, 12], fluid properties[10, 11], and ignore ionization and dissociation effects[9–

11]. All of these models assume no initial bulk velocities. In the models of Bradley et al.[9], Kono et al.[10], and Sloane et al.[11], the initial time coincides with the termination of the nominal μs discharge. Due to the initial conditions of these models, the blast wave formation and propagation are not modeled properly. The models of Kravchik et al.[12] and Tanaka et al.[13] have the initial conditions coinciding with the termination of the breakdown stage, and subsequently predict the discharge and decay dynamics. Tanaka et al.[13] is the only model reported which predicts the kernel dynamics and the blast wave propagation, but agreement with experiment is marginal. In all cases the initial conditions are cylindrical, and tailored for the optimal computational prediction of high-speed photographic measurements.

Despite the geometric differences between electrode sparks and laser sparks, the respective kernel dynamics share similar flow field formations. The similarity in the flow fields arise from the axial symmetry and elongated energy deposition characteristic of both of the processes. However, due to the different spark channel geometries, drastic differences in the flow patterns exist. The understanding of these differences arising from a differing spark channel geometry is vital to the knowledge of the laser ignition kernel dynamics.

It is the purpose of this work to computationally simulate the fluid dynamics of laser spark decay subsequent to the termination of the laser pulse using real fluid values, and to accurately predict various experimentally measured fluid dynamic characteristics. Specifically, a commercial software package (CFD-ACE[14]),

designed for multi-disciplinary neutral gas dynamic simulations, is modified through user-functions to model plasma and combustion reactions simultaneously for air and ammonia-oxygen mixtures. The initial temperature profile and associated fluid properties assigned to the laser spark upon termination of the laser pulse are discussed in Section 2. In Section 3, the computational fluid dynamic (CFD) methods used by the simulation software are described. The simulation predictions of characteristic flow patterns in air such as blast wave formation, propagation, and collapse are reported and compared with prior calculations and experimental measurement in Section 4. In Section 5, the CFD model is applied to the laser-ignition of ammonia-oxygen mixtures with various equivalence ratios and results are compared with experimental measurements. In Section 6, the work presented is summarized as the specifics of the simulation model and computational results are highlighted.

2 Laser Spark Properties

In this work simulation of laser spark decay in air (as a molar 0.785:0.215 nitrogen-oxygen mixture) and various ammonia-oxygen mixtures are investigated. For accurate simulations, the proper thermodynamic properties of these gas mixture species in the 298 K to 35,000 K temperature range are required. In Subsection 2.1, the calculation and fitting of the enthalpy, entropy, and specific heat of various particles are discussed. In Subsection 2.2, the derived thermal properties are used to find the equilibrium species, pressure, and energy corresponding to the initial temperature profile for various ambient gas mixtures. The transport properties of the high-temperature mixtures are discussed in Subsection 2.3.

2.1 Temperature Profile

The amplitude and gradient of the initial temperature profile of the laser induced plasma are chosen based on theoretical [15–20], experimental[4, 8, 21–24], and computational investigations[8, 25]. Specifically, the temperature profile shown in Figure 1 describes the laser induced spark upon termination of a 10 ns, 1064 nm wavelength Nd:YAG laser pulse with 40 mJ of energy. Only a fraction of the total laser pulse energy goes into the formation of the laser spark. The temperature profile is shown with a horizontal optic axis (x-axis) from which the laser was focused from the left-hand-side. The geometrical focal point of the modeled lens-laser-pulse system is positioned to the right (up the optic axis) of the laser spark[2]. The spark is about 1

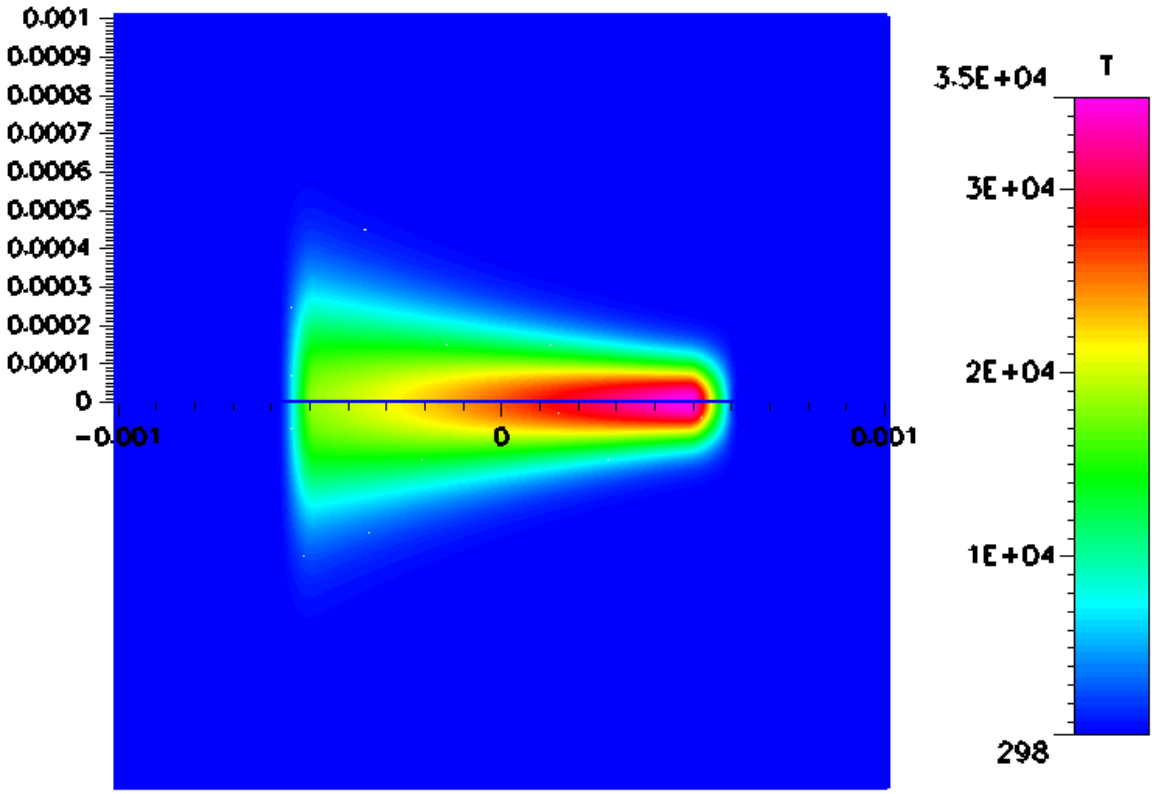

Figure 1: Initial temperature profile representing the energy deposition of the laser pulse subsequent to laser pulse termination. Spatial dimensions along the optic (horizontal) axis and the axis perpendicular are in units of meters. The temperature values are in units of Kelvin.

mm in length along the x-axis, consistent with experimental measurements[4]. The zero-point of the x-axis arbitrarily positioned at the mid-point of the spark. The temperature assigned to the gas along the optic axis between -0.5 mm and 0.5 mm is mathematically described by

$$T = 26000e^{700x}, \tag{1}$$

where x is in units of meters, based on theoretical and computational investigations. The saturation limit of ≈35,000 K measured by Stricker et al.[22] is imposed by redefining all temperatures higher than the saturation limit, equal to 35,000 K. Away from the optic axis, the temperature profile is given an axially-symmetric Gaussian profile with a varying half-width (HW), in units of meters, defined by

$$HW = 2.82 \times 10^{-4} e^{-1050x}. \tag{2}$$

The half-widths at the ends of the spark profile are taken from the diffraction-limited focal irradiance calculations of Plemmons[8], and adjusted to account for the effects of a multi-mode laser pulse. Smoothing of the profile is applied at $x = 0.5$ mm and $x = -0.5$ mm edges to reduce the unrealistically sharp and computationally unresolvable gradients. Specifically, the smoothing invokes a spatially exponential decay of the temperature in the $x > 0.5$ and $x < -0.5$ regions to allow for adequate resolution of the gradient. The particular method used to smooth the sharp gradients has been shown to be inconsequential to the simulation results in the temporal range of interest. This initial temperature profile is used throughout the rest of the investigation and

therefore is considered to be invariant with differing gas mixtures. This profile is assigned the computational time of 10 ns. This temperature profile bas been shown to be fairly insensitive for the course fluid phenomena being modeled. However, for the investigation of finer detail, additional tailoring of the profile must be performed.

2.2 Thermodynamic Properties

The molar enthalpy ($\tilde{h}$), molar specific heat ($\tilde{c_p}$), and molar entropy ($\tilde{s}$) of the plasma constituents are required for the proper modeling of dissociation, ionization, species concentrations, energy transport, pressure, and temperature decay. The high collision frequency associated with the temperatures and number densities in the laser spark allow for local thermal equilibrium (LTE) approximations. Since the most recent Journal of Army, Navy, NASA, and Air Force (JANNAF) table only covers the properties of interest for temperatures up to 20,000 K, the properties for the species of interest in the 20,000 K - 35,000 K temperature range must be evaluated. From investigations with molecular dissociation and molecular and atomic Saha equations[25], it is determined that the thermodynamic properties of the neutral and singly ionized hydrogen, nitrogen, and oxygen along with doubly ionized nitrogen and oxygen atoms are required in this temperature range.

The thermodynamics properties are evaluated by first calculating the molar energies of the species as a function of temperature. The molar energy of a pure

Table 1: The ionization molar energies of H, N, and O [MJ/mol].[5]

	H	N	O
I	1.31	1.40	1.31
II	-	2.85	3.38

monatomic/monoionic gas, $\tilde{E}_{A^i}$, is evaluated by

$$\tilde{E}_{A^i} = \tilde{E}^{trans}_{A^i} + \tilde{E}^{ele}_{A^i} + \sum_{j=2}^{i} \tilde{I}_{j-1}, \tag{3}$$

where $\tilde{E}^{trans}_{A^i}$, $\tilde{E}^{ele}_{A^i}$, and $\tilde{I}_i$ are the molar translational, electric, and ionization energies of the i^{th} ion (i=1 defines the neutral atom), respectively. The molar translational energy is evaluated by

$$\tilde{E}^{trans} = \frac{3}{2}RT, \tag{4}$$

where R is the ideal gas constant ($\approx$ 8.31451 J/K/mol). The molar electric energy is calculated by the equation

$$\tilde{E}^{ele}_{A^i} = \frac{N_A \sum_i E_i^{A^i} g_i e^{-E_i^{A^i}/RT}}{\sum_i g_i e^{-E_i^{A^i}/RT}}, \tag{5}$$

where g_i and $E_i^{A^i}$ are the degeneracy and energy of individual atomic/ionic electric energy levels taken from published tables[26], and N_A is the Avogadro constant. The ionization energies of atoms and ions investigated are listed in Table 1.

With the above treatment, the molar energies of the high-temperature atoms and ions are evaluated as a function of temperature. From the molar energy evaluation, molar specific heat ($\tilde{c_p}$), the molar enthalpy ($\tilde{h}$), and molar entropy ($\tilde{s}$) for an ideal

gas are respectively evaluated by the relations

$$\tilde{c_p} = \frac{\partial \tilde{E}}{\partial T} + R, \tag{6}$$

$$\tilde{h} = \tilde{h}^0_{298} + \int_{298}^{T} \tilde{c_p} dT, \tag{7}$$

and

$$\tilde{s} = \tilde{s}^0_{298} + \int_{298}^{T} \frac{\tilde{c_p}}{T} dT, \tag{8}$$

where $\tilde{h}^o_{298}$ and $\tilde{s}^o_{298}$ are the standard molar enthalpy and entropy, respectively

The CFD software package[27] used in this work requires the thermodynamic properties of each species to be represented by 14 coefficients (a_1-a_{14}). The fitting functions used are identical to those of Gordon and McBride (1976) and are commonly referred to as the "old" form. The fitting functions are

$$\frac{\tilde{c_p}}{R} = a_1 + a_2 T + a_3 T^2 + a_4 T^3 + a_5 T^4, \tag{9}$$

$$\frac{\tilde{h}}{RT} = a_1 + \frac{a_2}{2} T + \frac{a_3}{3} T^2 + \frac{a_4}{4} T^3 + \frac{a_5}{5} T^4 + \frac{a_6}{T}, \tag{10}$$

and

$$\frac{\tilde{s}}{R} = a_1 ln(T) + a_2 T + \frac{a_3}{2} T^2 + \frac{a_4}{3} T^3 + \frac{a_5}{4} T^4 + a_7. \tag{11}$$

With a_1 to a_5 determined by a least-square fit of $\tilde{c_p}$/R, the remaining coefficients are evaluated as the integration constants

$$a_6 = \frac{\tilde{h}^0_{298}}{R} - 298 a_1 - \frac{298^2}{2} a_2 - \frac{298^3}{3} a_3 - \frac{298^4}{4} a_4 - \frac{298^5}{5} a_5, \tag{12}$$

and

$$a_7 = \frac{\tilde{s}^0_{298}}{R} - a_1 ln(298) - 298 a_2 - \frac{298^2}{2} a_3 - \frac{298^3}{3} a_4 - \frac{298^4}{4} a_5. \tag{13}$$

Seven fit coefficients (a_8-a_{14}) of the old form describe the thermodynamic properties in the 298 - 1,000 K temperature range, and the remaining seven (a_1-a_7 are traditionally used for fitting in the 1,000 - 6,000 K range. To cover the properties of the entire laser spark, the last temperature range is extended to 35,000 K for the electrons, atoms and ions present. The specific heat of H, H^+, N, N^+, N^{++}, O, O^+, and O^{++} are plotted with the least-square fits in Figures 2-4. The N and O^+ specific heats do not fit as well to the old form functions as the other species. This error, caused by the ineffective basis functions used in the fit, can not be avoided until the CFD software is upgraded to allow for a better thermodynamic property input interface. The major computational consequence of the poor fits lies in the discontinuity that occurs at the interface between the two temperature ranges for each species. Due to this, the least square fits are modified slightly to ensure good behavior at this interface.

A "new" fitting form developed by McBride and Gordon (1994) uses a 9-coefficent fitting function per temperature range along with an additional 6,000 K - 20,000 K temperature range to accurately fit the JANNAF table of thermodynamic properties. Due to the inability of the CFD software to interface with the new form, species that have a significant population in this temperature range are fitted to 20,000 K with the old form using the new form evaluation of the thermodynamic values. Figures 5 and 6 show the results of this fitting method for H_2, N_2, O_2, OH, NO, and NH.

The old form least-square coefficients of Gordon-McBride (1976) are used for NH_3,

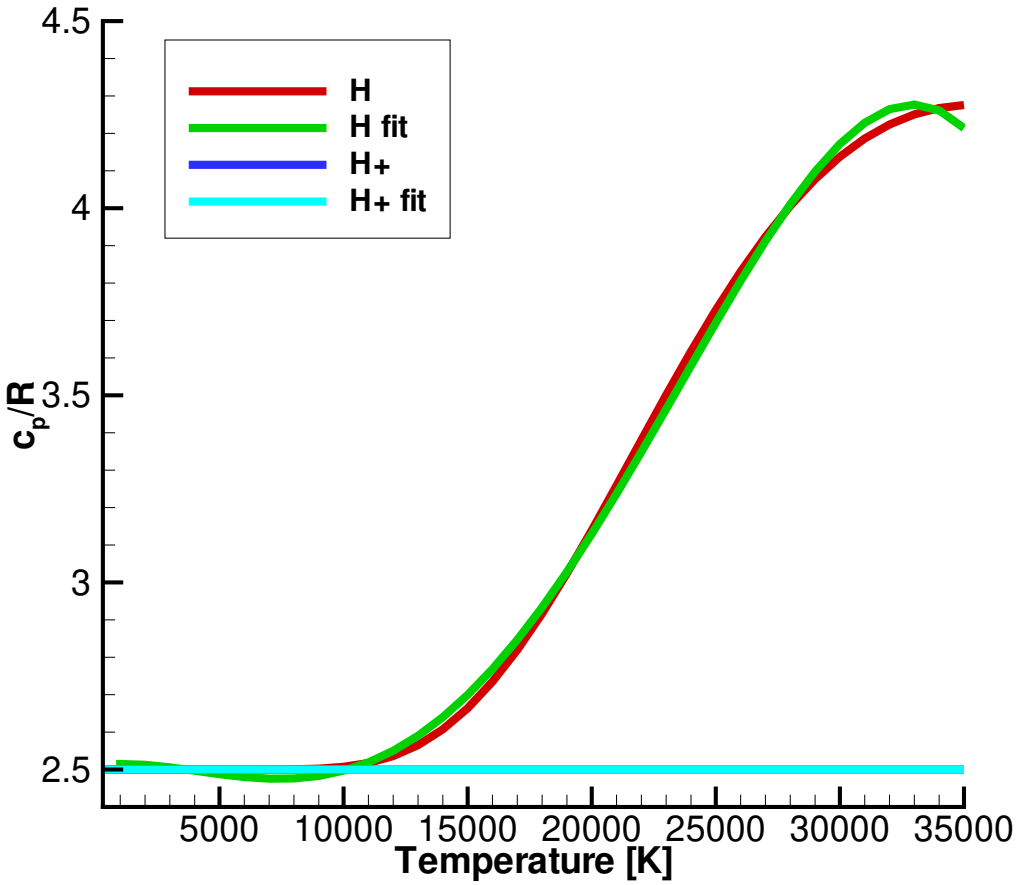

Figure 2: Calculated molar specific heat divided by the ideal gas constant for H and H^+ plotted with the least-square fit. The calculated value for H^+ is not visible due to the overlay of the H^+ fit. Temperature values are in units of Kelvin.

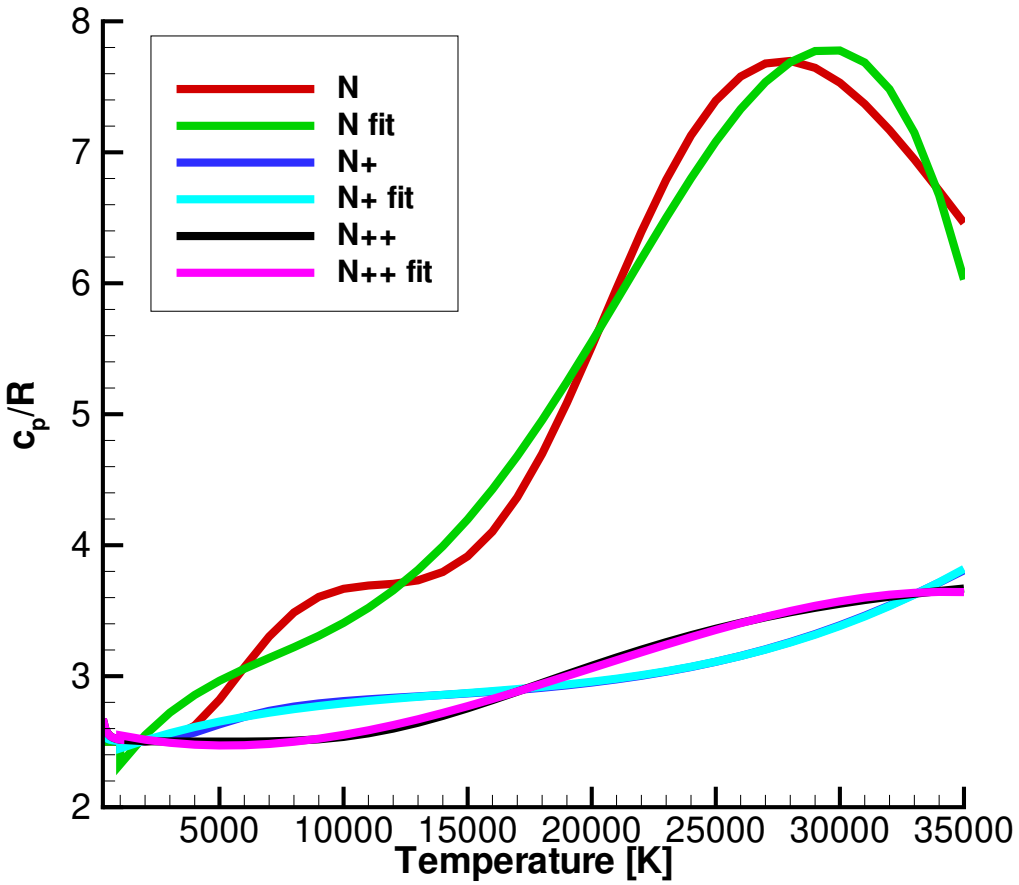

Figure 3: Calculated molar specific heat divided by the ideal gas constant for N, N^+, and N^{++} plotted with the least-square fit. Temperature values are in units of Kelvin.

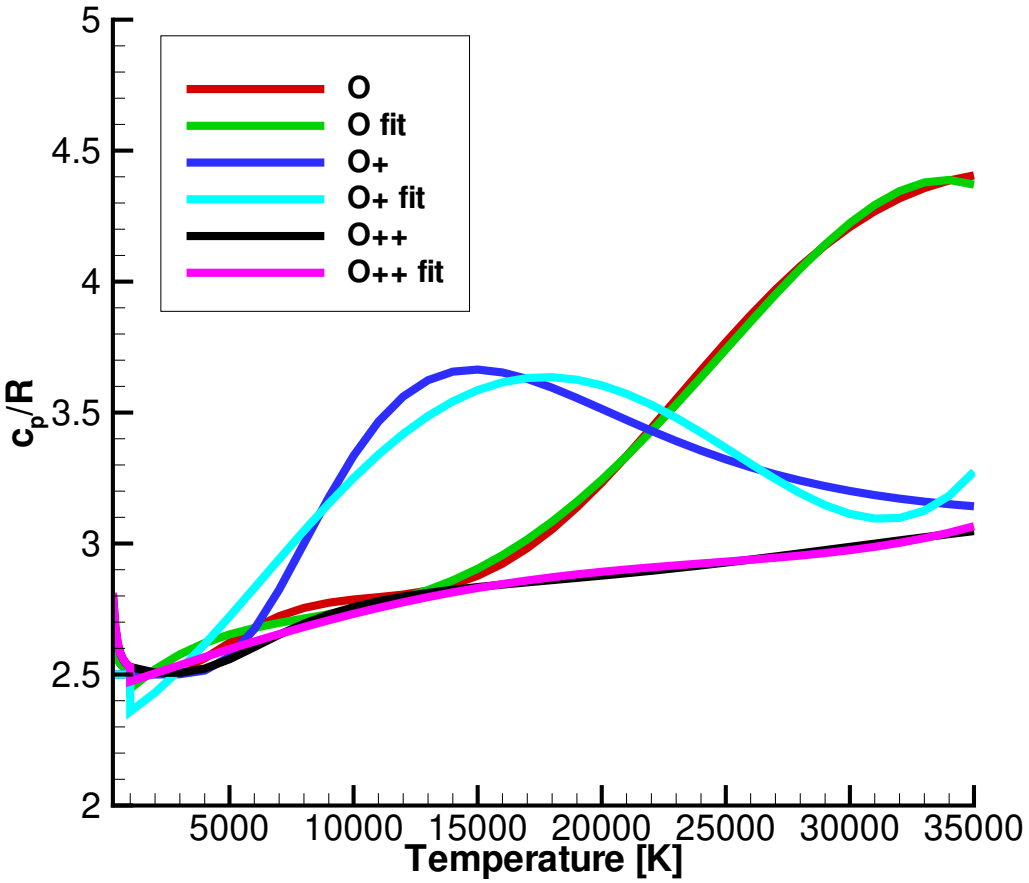

Figure 4: Calculated molar specific heat divided by the ideal gas constant for O, O^+, and O^{++} plotted with the least-square fit. Temperature values are in units of Kelvin.

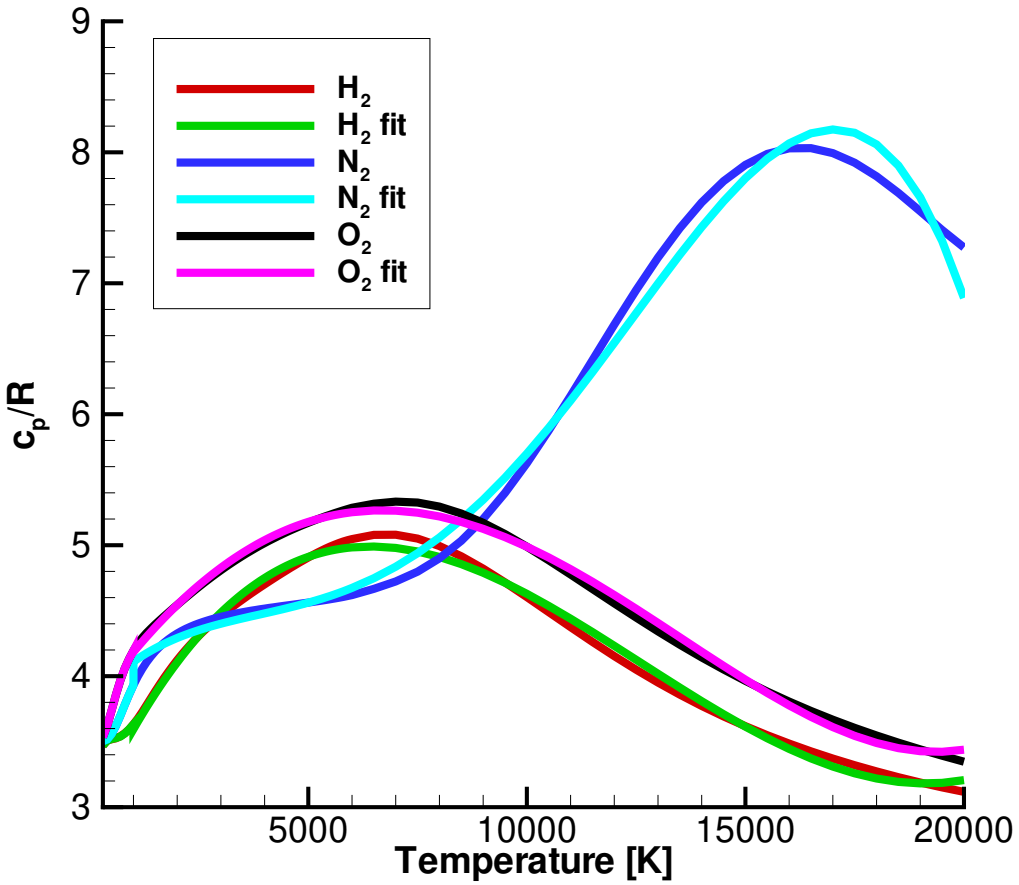

Figure 5: The molar specific heat divided by the ideal gas constant for H_2, N_2, and O_2 plotted with the least-square fit. Temperature values are in units of Kelvin.

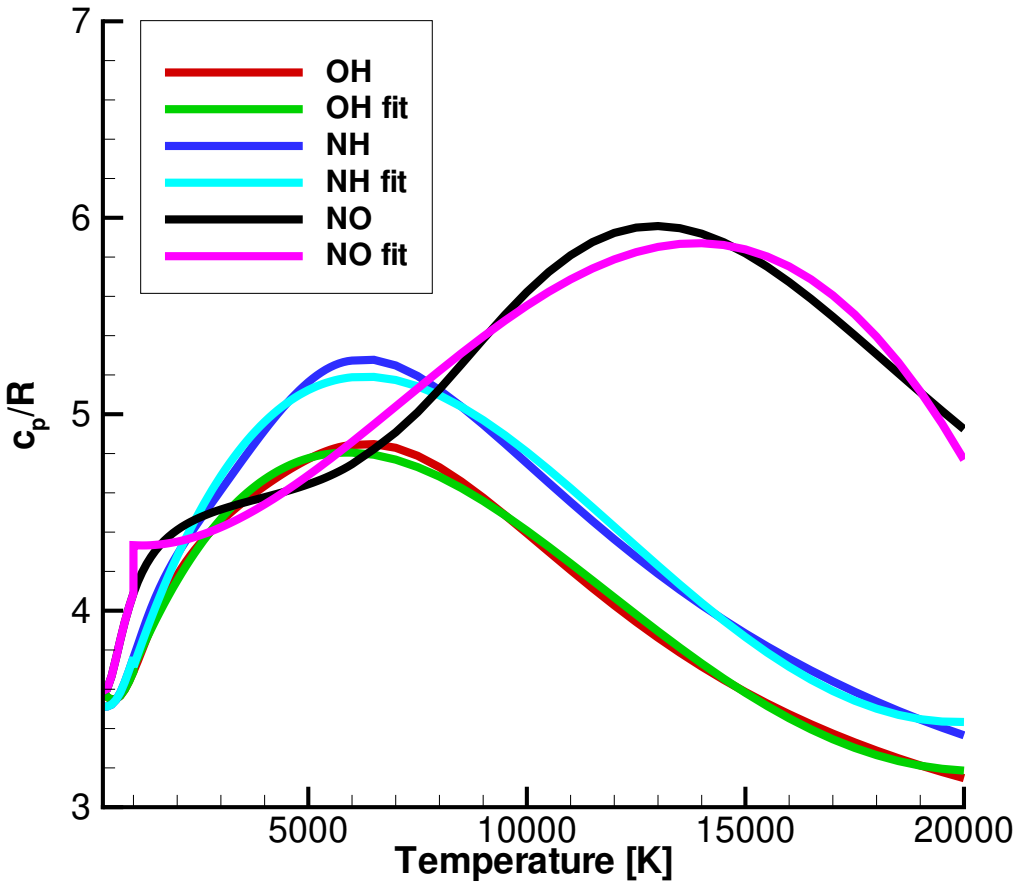

Figure 6: The molar specific heat divided by the ideal gas constant for NO, OH, and NH plotted with the least-square fit. Temperature values are in units of Kelvin.

NH_2, and H_2O since these species are inconsequential at temperatures above 6,000 K.

2.3 Species Concentrations

With the irradiance values of 10^9 W/cm^2 achieved in the laser-induced breakdown scheme investigated, the primary ionization mechanism dominating the size and shape of the plasma is laser-supported radiation (LSR) ionization[18]. A characteristic of the LSR ionization is that it propagates up the optic axis without modification of the mass density field. The equilibrium species concentrations of the initial laser spark are calculated by the minimization of the molar Gibbs free energy ($\tilde{G}$) with the constant mass density constraint.

The molar Gibbs free energy of a mixture of species as a function of gas temperature (T) and pressure (P) is

$$\tilde{G}(T,P) = \sum_{i=1}^{N_s} \tilde{n}_i \tilde{G}_i(T,P) = \sum_{i=1}^{N_s} \tilde{n}_i \Big(\tilde{G}_i(T,P_0) + RTln(\frac{P_i}{P_0}) \Big), \tag{14}$$

where N_s is the number of species considered, P_0 is the reference pressure of 101,325 Pa, and $\tilde{G}_i$ and P_i are the molar Gibbs free energy (chemical potential) and the partial pressure of species i, respectively. The molar Gibbs free energy of species i is evaluated as

$$\tilde{G}_i(T,P_0) = \tilde{h}_i(T) - T\tilde{s}_i(T). \tag{15}$$

The constant mass density constraint used to model the initial plasma is written

$$\tilde{n}_j^e = \sum_{i=1}^{N_s} a_{ji}\tilde{n}_i \quad j = 1, ..., N_e, \tag{16}$$

where $\tilde{n}_j^e$ is the molar number density of element j (regardless of bonding), a_{ji} is the number of j atoms in species i, and N_e is the total number of elements considered.

The minimization of the molar Gibbs free energy with the constant mass density constraint is achieved by the method of Lagrangian multipliers with the minimization function (Ψ)

$$\Psi = \tilde{h}_i(T) - T\tilde{s}_i(T) - \sum_{j=1}^{N_e} \Lambda_j (\sum_{i=1}^{N_s} a_{ji}\tilde{n}_i - \tilde{n}_j^e) \tag{17}$$

where Λ_j is the j^{th} undetermined multiplier. Differentiating Ψ with respect to $\tilde{n}_i$ and Λ_j separately and setting each derivative of Ψ to zero results in $N_e + N_s$ equations and $N_e + N_s$ unknowns. This system of equations is solved numerically by the use of the robust secant method. To determine the effect caused by the extension of the maximum temperature value of the old form fits, the equilibrium species are solved for a given temperature and pressure and compared with the NASA Chemical Equilibrium and Applications (CEA) code[28]. The CEA code, written by Gordon and McBride, invokes the new form of thermodynamic fits along with the Newton-Raphson method for solving the system of equations. The comparison of the two methods is shown in Table 2 for various temperatures. Since CEA contains neither O^{++} nor N^{++} in its library of thermodynamic properties, those values are not applicable in its calculation. The results of the two methods compare extremely well, and with a few exceptions agree to two significant figures. Thus, despite the inaccuracy in the use of the old form in fitting the thermodynamic properties, the results are tolerable.

The initial laser spark species concentrations are calculated by the above method

Table 2: Equilibrium species mole fractions at various temperatures and a pressure of 101,325 Pa. The initial mixture was composed with NH_3 and O_2 mole fractions of 0.48 and 0.52, respectively. The upper values for each species are calculated by this work, while the lower values are the result of the CEA code. Mole fraction values less than 10^{-10} are reported as zero.

	298 K	1,000 K	5,000 K	10,000 K	15,000 K	20,000 K
NH3	$4.47\text{x}10^{-1}$	$7.73\text{x}10^{-5}$	$3.93\text{x}10^{-10}$	0.0	0.0	0.0
NH3	$4.48\text{x}10^{-1}$	$7.80\text{x}10^{-5}$	$4.86\text{x}10^{-10}$	0.0	0.0	0.0
NH2	$4.86\text{x}10^{-8}$	$2.90\text{x}10^{-4}$	$8.32\text{x}10^{-6}$	$2.10\text{x}10^{-9}$	0.0	0.0
NH2	0.0	0.0	$1.87\text{x}10^{-7}$	$2.54\text{x}10^{-10}$	0.0	0.0
NH	0.0	0.0	$3.87\text{x}10^{-5}$	$1.02\text{x}10^{-5}$	$2.10\text{x}10^{-7}$	$4.02\text{x}10^{-10}$
NH	0.0	0.0	$4.99\text{x}10^{-5}$	$9.12\text{x}10^{-6}$	$2.15\text{x}10^{-7}$	$4.51\text{x}10^{-10}$
OH	$1.46\text{x}10^{-7}$	$2.46\text{x}10^{-2}$	$8.73\text{x}10^{-3}$	$2.72\text{x}10^{-5}$	$6.13\text{x}10^{-7}$	$1.40\text{x}10^{-9}$
OH	$1.10\text{x}10^{-7}$	$2.31\text{x}10^{-2}$	$8.65\text{x}10^{-3}$	$2.69\text{x}10^{-5}$	$5.95\text{x}10^{-7}$	$1.32\text{x}10^{-9}$
NO	0.0	$2.07\text{x}10^{-5}$	$1.37\text{x}10^{-2}$	$1.03\text{x}10^{-4}$	$7.00\text{x}10^{-5}$	$8.05\text{x}10^{-10}$
NO	0.0	$1.81\text{x}10^{-5}$	$7.46\text{x}10^{-3}$	$3.36\text{x}10^{-5}$	$2.50\text{x}10^{-7}$	$3.03\text{x}10^{-10}$
H2	$3.31\text{x}10^{-2}$	$4.74\text{x}10^{-1}$	$4.97\text{x}10^{-3}$	$1.47\text{x}10^{-5}$	$3.47\text{x}10^{-7}$	$9.07\text{x}10^{-10}$
H2	$3.20\text{x}10^{-2}$	$4.75\text{x}10^{-1}$	$6.52\text{x}10^{-3}$	$1.99\text{x}10^{-5}$	$4.69\text{x}10^{-7}$	$1.21\text{x}10^{-9}$
N2	$1.10\text{x}10^{-2}$	$1.62\text{x}10^{-1}$	$8.04\text{x}10^{-2}$	$3.19\text{x}10^{-4}$	$3.50\text{x}10^{-7}$	$1.60\text{x}10^{-10}$
N2	$1.07\text{x}10^{-2}$	$1.62\text{x}10^{-1}$	$8.13\text{x}10^{-2}$	$1.25\text{x}10^{-4}$	$1.72\text{x}10^{-7}$	0.0
O2	$5.09\text{x}10^{-1}$	$3.39\text{x}10^{-1}$	$4.38\text{x}10^{-3}$	$7.71\text{x}10^{-6}$	$1.54\text{x}10^{-7}$	$3.08\text{x}10^{-10}$
O2	$5.09\text{x}10^{-1}$	$3.40\text{x}10^{-1}$	$2.79\text{x}10^{-3}$	$4.68\text{x}10^{-6}$	$8.94\text{x}10^{-8}$	$1.70\text{x}10^{-10}$
H	0.0	$1.57\text{x}10^{-9}$	$5.22\text{x}10^{-1}$	$4.66\text{x}10^{-1}$	$1.89\text{x}10^{-1}$	$1.68\text{x}10^{-2}$
H	0.0	$1.56\text{x}10^{-9}$	$5.17\text{x}10^{-1}$	$4.66\text{x}10^{-1}$	$1.88\text{x}10^{-1}$	$1.66\text{x}10^{-2}$
N	0.0	0.0	$5.76\text{x}10^{-3}$	$1.52\text{x}10^{-1}$	$4.16\text{x}10^{-2}$	$2.66\text{x}10^{-3}$
N	0.0	0.0	$9.38\text{x}10^{-3}$	$1.54\text{x}10^{-1}$	$4.86\text{x}10^{-2}$	$3.28\text{x}10^{-3}$
O	0.0	0.0	$3.60\text{x}10^{-1}$	$3.38\text{x}10^{-1}$	$1.40\text{x}10^{-1}$	$1.16\text{x}10^{-2}$
O	0.0	0.0	$3.67\text{x}10^{-1}$	$3.38\text{x}10^{-1}$	$1.38\text{x}10^{-1}$	$1.11\text{x}10^{-2}$
H+	0.0	0.0	$1.94\text{x}10^{-6}$	$9.82\text{x}10^{-3}$	$1.45\text{x}10^{-1}$	$2.34\text{x}10^{-1}$
H+	0.0	0.0	$1.91\text{x}10^{-6}$	$1.02\text{x}10^{-2}$	$1.47\text{x}10^{-1}$	$2.34\text{x}10^{-1}$
N+	0.0	0.0	$1.62\text{x}10^{-8}$	$5.80\text{x}10^{-3}$	$6.95\text{x}10^{-2}$	$8.04\text{x}10^{-2}$
N+	0.0	0.0	$1.73\text{x}10^{-8}$	$4.54\text{x}10^{-3}$	$6.28\text{x}10^{-2}$	$8.03\text{x}10^{-2}$
O+	0.0	0.0	$1.10\text{x}10^{-6}$	$6.00\text{x}10^{-3}$	$1.00\text{x}10^{-1}$	$1.69\text{x}10^{-1}$
O+	0.0	0.0	$1.17\text{x}10^{-6}$	$6.46\text{x}10^{-3}$	$1.03\text{x}10^{-1}$	$1.70\text{x}10^{-1}$
N++	0.0	0.0	0.0	0.0	$1.11\text{x}10^{-6}$	$4.98\text{x}10^{-4}$
N++	N/A	N/A	N/A	N/A	N/A	N/A
O++	0.0	0.0	0.0	0.0	$4.70\text{x}10^{-9}$	$8.46\text{x}10^{-6}$
O++	N/A	N/A	N/A	N/A	N/A	N/A
e-	0.0	0.0	$3.05\text{x}10^{-6}$	$2.17\text{x}10^{-2}$	$3.15\text{x}10^{-1}$	$4.85\text{x}10^{-1}$
e-	0.0	0.0	$3.10\text{x}10^{-6}$	$2.12\text{x}10^{-2}$	$3.13\text{x}10^{-1}$	$4.85\text{x}10^{-1}$

using the old form thermodynamic property fit coefficients over the 298 K - 35,000 K temperature range. The computed number densities of species existing in the laser spark for air and a 0.93:1.0 molar mixture of NH_3-O_2 are shown in Figures 7 and 8. In both cases H2O is excluded from the equilibrium calculation. If included, the stability of H2O causes an unrealistic instantaneous combustion. It is this very combustion process that we wish to simulate through time. The treatment of H2O and combustion reactions in this work are described in Subsection 2.3.

Figures 7 and 8 show that the majority of diatomic-molecular dissociation occurs at temperatures less than 20,000 K. This validates the upper temperature limit used in the fits of the molecular thermodynamic properties, and also the use of the thermodynamic values from the new JANNAF table. The significance of the double ionized atoms is shown by the number densities of N^{++} in Figure 7 and O^{++} in Figure 8. Additionally, with the continued increase in number density of these ions at 35,000 K, and knowledge of their ionization potentials, it is easily inferred that triply ionized atoms are insignificant inside the temperature range of interest.

The initial pressure profile is calculated from the initial temperature profile and a given gas mixture with the initial number densities by

$$P = \sum_{i=1}^{N_s} \tilde{n}_i RT. \tag{18}$$

The initial pressure profiles corresponding to the cases of air and the 0.93:1.0 molar mixture of NH_3-O_2 are shown in Figures 9 and 10. Both pressure profiles have maximum values in the hundreds of atmospheres. Due to these high pressures and

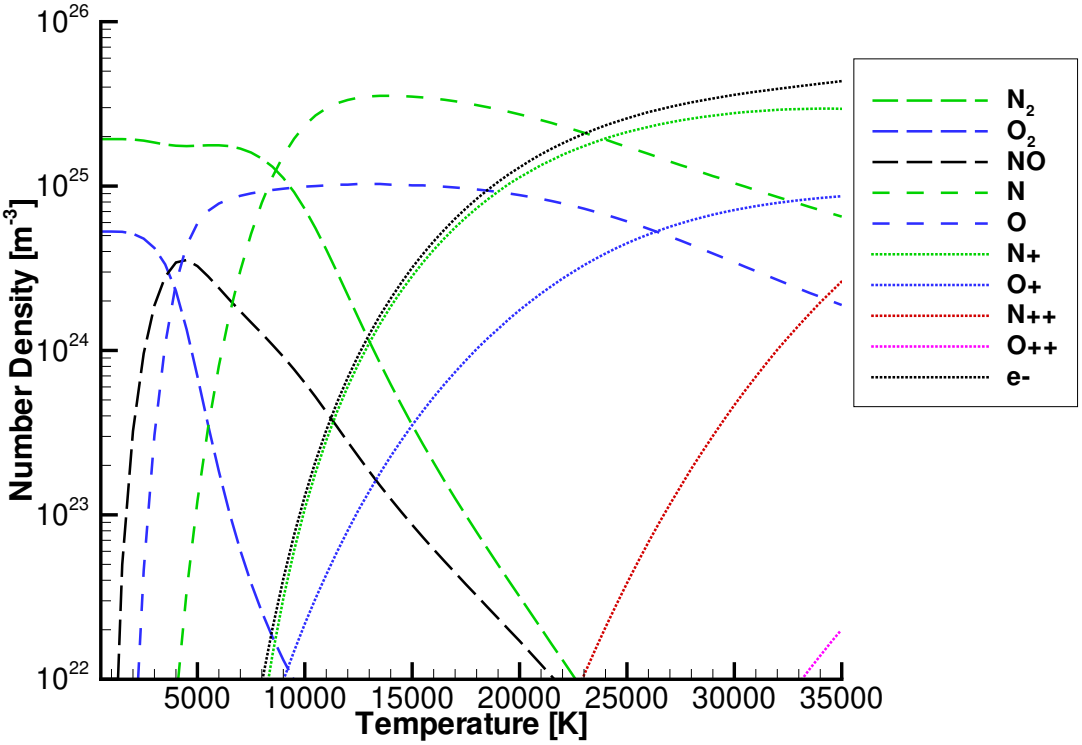

Figure 7: Initial species number densities contained in a laser spark in air subsequent to laser pulse termination. The number density values are plotting in units of particles per cubic meter. The temperature values are in units of Kelvin.

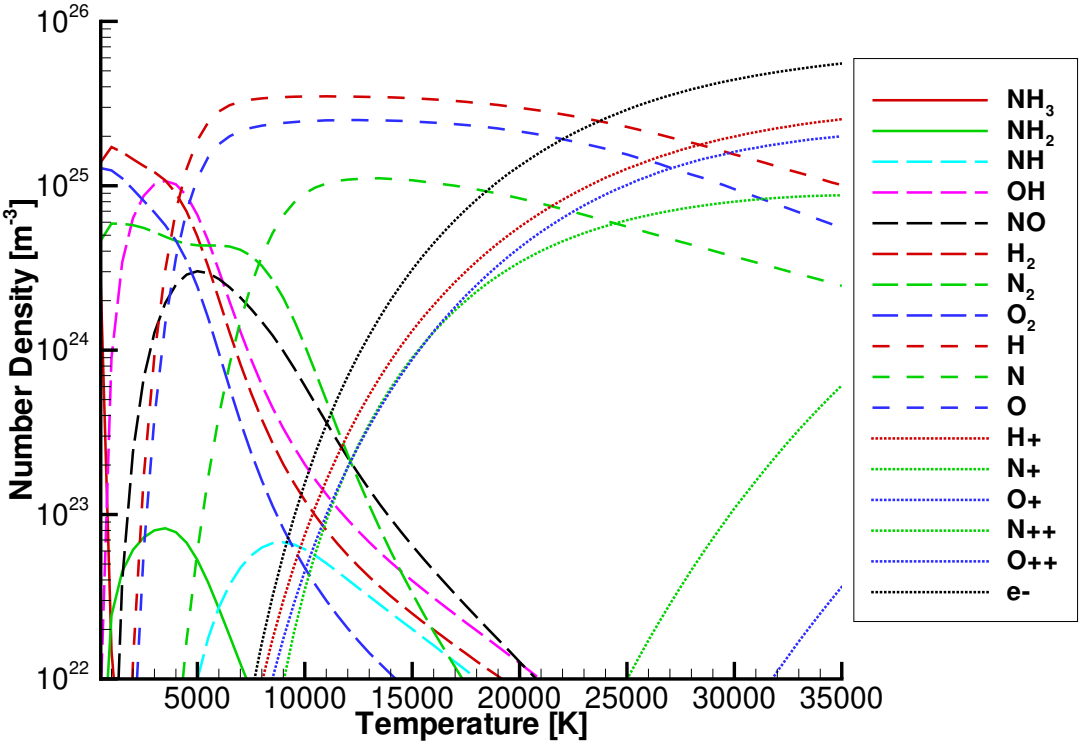

Figure 8: Initial species number densities contained in a laser spark in a 0.93:1.0 molar mixture of ammonia and oxygen subsequent to laser pulse termination. The number density values are plotting in units of particles per cubic meter. The temperature values are in units of Kelvin.

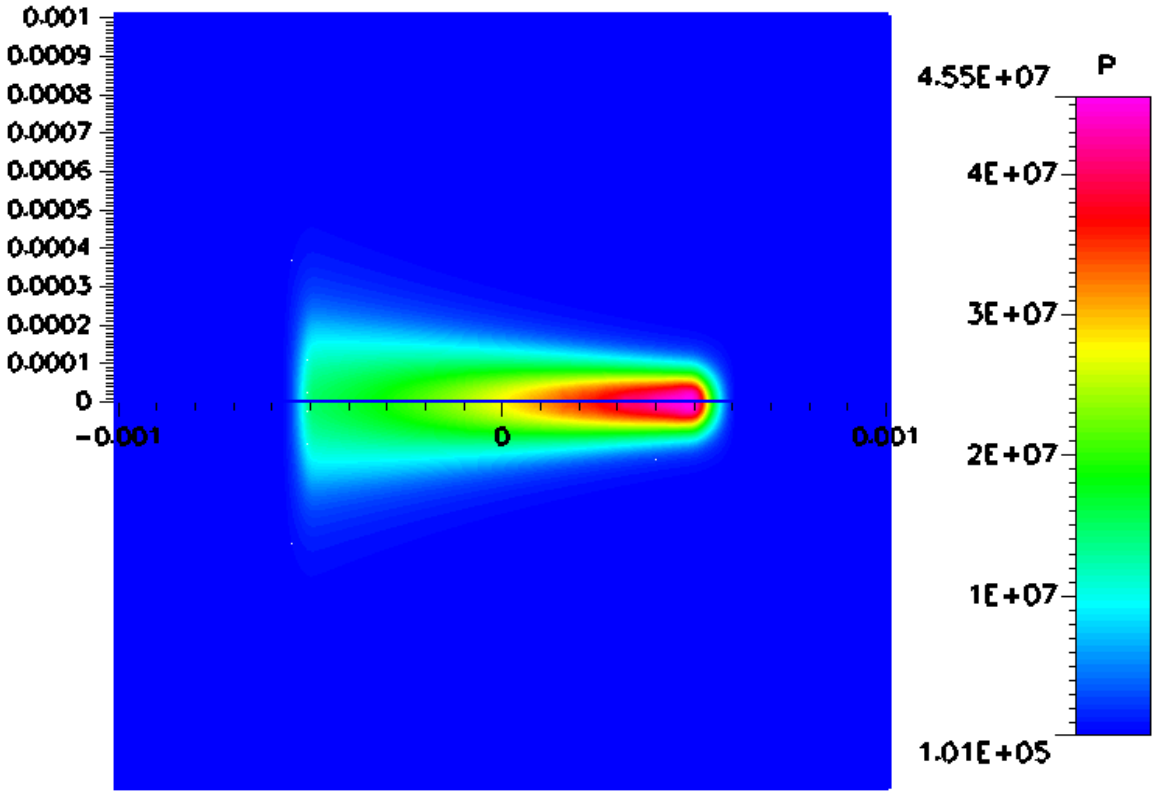

Figure 9: Initial pressure profile including ionization and dissociation effects of air subsequent to laser pulse termination. Spatial dimensions along the x-axis (horizontal) and the axis perpendicular are in units of meters. The pressure values are in units of pascals.

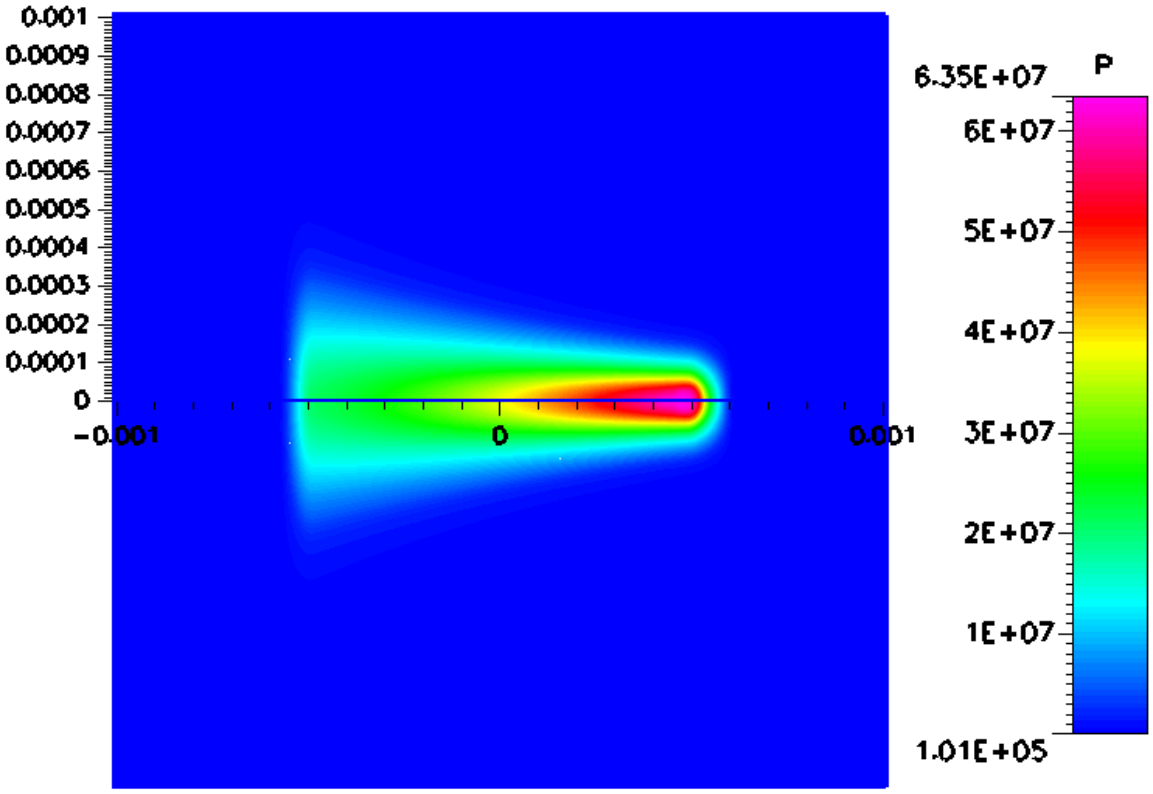

Figure 10: Initial pressure profile including ionization and dissociation effects of a 0.93:1.0 molar mixture of ammonia and oxygen subsequent to laser pulse termination. Spatial dimensions along the x-axis (horizontal) and the axis perpendicular are in units of meters. The pressure values are in units of pascals.

steep gradients, the initial relaxation of the profile (decay of the spark) is expected to result in a violent expansion and blast wave formation.

With the temperature, species concentrations, and thermodynamic properties of the initial laser spark, the energy (E) of the initial profiles are calculated by

$$E = 2\pi \int_{x=-0.6mm}^{0.6mm} \int_{r=0.0mm}^{0.6mm} \left(\sum_{i=1}^{N_s} (\tilde{h}_i \tilde{n}_i - p_i)_{T=T'(x,r)} - \sum_{i=1}^{N_s} (\tilde{h}_i^0 \tilde{n}_i^0 - p_i^0)_{T=298} \right) r dr dx \quad (19)$$

where x is along the optic axis, r is an axis perpendicular, T' is the gas temperature at a given (x,r) location, and the superscript "^{0}" represents the values of the ambient species. The result of this evaluation is the thermodynamic energy relative to the ambient gas mixture. Applying the composite Simpson's rule [29] to the numerical integration of Equation 19 for the air and NH_3-O_2 cases, results in energy values of 9.2 mJ and 12.3 mJ, respectively. These values may be interpreted as the magnitude of the modeled laser energy deposition.

2.4 Transport Properties

For the proper modeling of the fluid dynamics resulting from the laser spark decay, the transport properties should take into account as many ionization effects as possible. Specifically, ionization potentials, coulomb interactions, and the minute mass of the electron affect the viscosity, thermal conductivity, and diffusion, thus making the nominal low-temperature models partially ineffective.

The viscosity (η) of a gas is defined by the equation

$$J_{p_x} = -\eta \frac{\partial v_x}{\partial z}, \quad (20)$$

where J_{p_x} is the flux density of x-momentum and v_x is the x-velocity. The viscosity of ionized hydrogen, nitrogen, and oxygen gases is taken from tabulated values of Boulos et al.[1]. These tabulated values include effects of dissociation, ionization, and free electrons on an initially homogeneous gas at 101,325 Pa. Figure 11 shows that the viscosity of hydrogen, nitrogen, and oxygen gas decreases as the temperature increases over 11,000 K. Comparison of Figure 11 with Table 2 and Figures 7 and 8 shows the decrease to occur at the onset of ionization. This sharp decrease is due to the increased collision integral values caused by long-range Coulomb interactions between charged particles.

The viscosity of gas mixtures (η_{mix}) is evaluated through with the use of Wilke's semi-empirical approximation[27, 30],

$$\eta_{mix} = \sum_{\alpha} \frac{\chi_\alpha \eta_\alpha}{\sum_\beta \chi_\beta Z_{\alpha\beta}}, \tag{21}$$

where

$$Z_{\alpha\beta} = \frac{\left[1 + \sqrt{\frac{\eta_\alpha}{\eta_\beta}}\left(\frac{m_\beta}{m_\alpha}\right)^{\frac{1}{4}}\right]^2}{\sqrt{8(1 + \frac{m_\alpha}{m_\beta})}}, \tag{22}$$

χ_α is the mole fraction of species α, and η_α and m_α are respectively the viscosity and molecular weight of the ionized gas of species α. The approximation of Wilke has been shown to produce good results while sidestepping the difficult evaluation of the collision integrals for each species collision combination. Figure 12 shows the results of the viscosity calculations for ammonia-oxygen mixtures with various fuel equivalence ratios (ϕ). For regions with gaseous temperatures below 6,000 K, the viscosity is

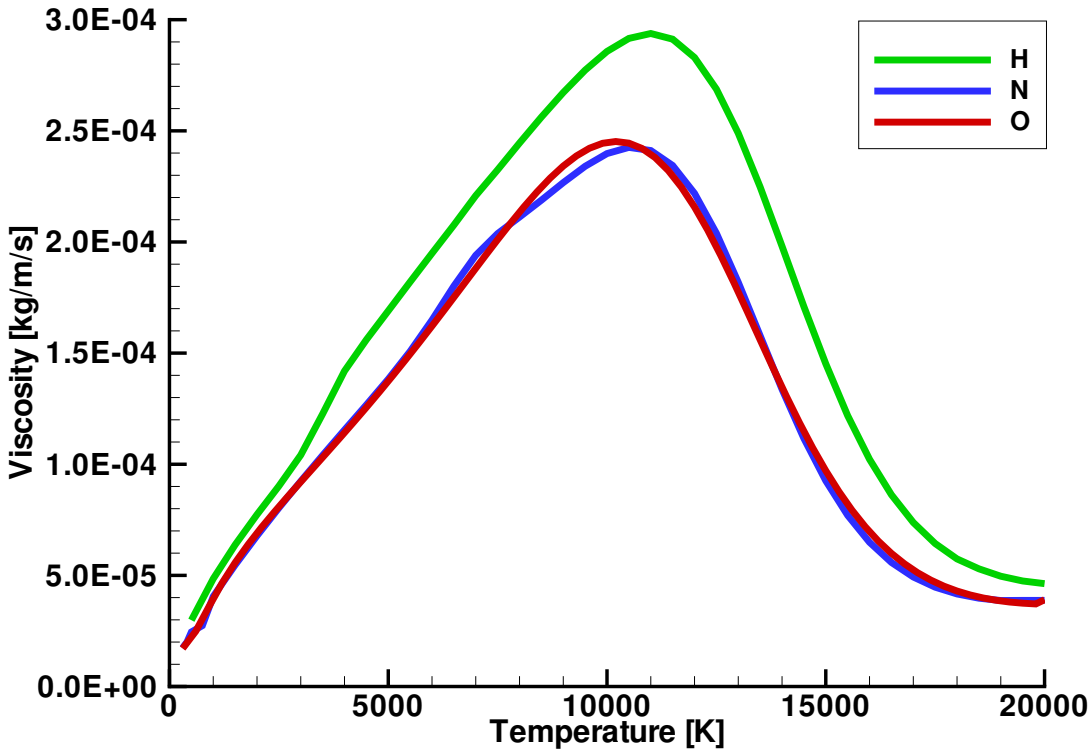

Figure 11: Viscosity of high-temperature hydrogen, nitrogen, and oxygen gas at 101,325 Pa including dissociation and ionization effects[1]. Viscosity values are in units of kg/m/s. Temperatures values are in units of Kelvin.

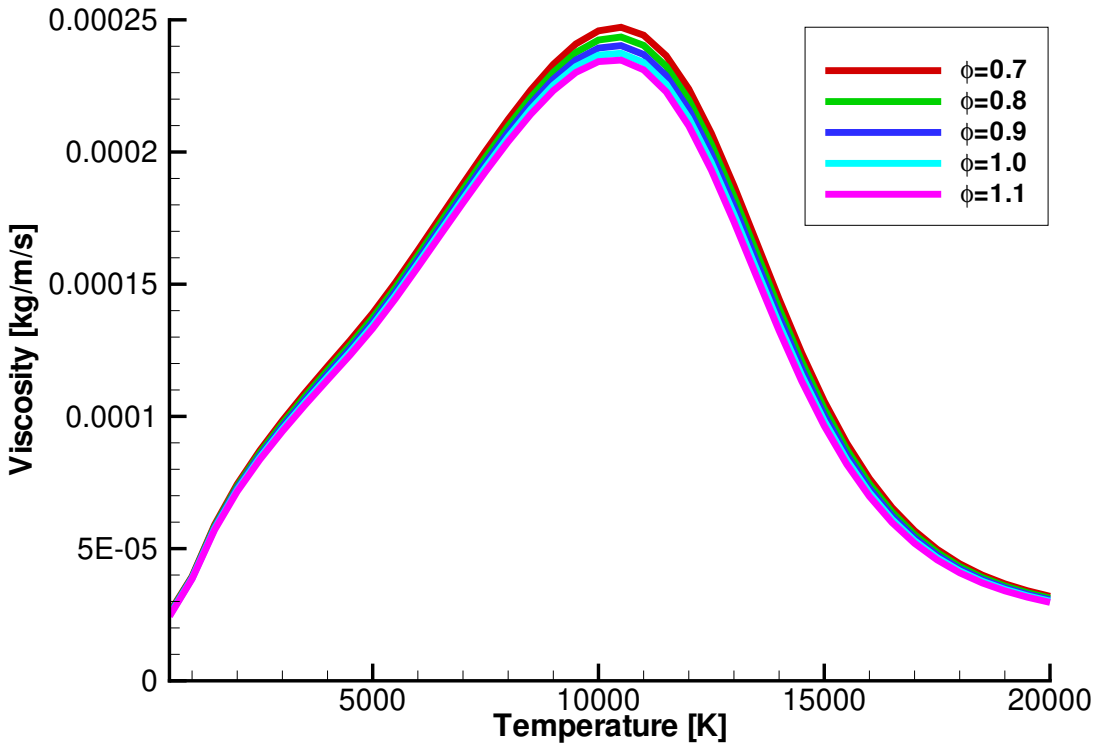

Figure 12: Viscosity of various high-temperature ammonia-oxygen mixtures at 101,325 Pa including dissociation and ionization effects. The homogeneous hydrogen, nitrogen, and oxygen viscosity values are taken from Boulos et al.[1]. Viscosity values are in units of kg/m/s. Temperature values are in units of Kelvin.

evaluated using Sutherland's law for individual species, and weighted accordingly to local species concentrations.

The thermal conductivity, κ, of a gas is defined by Fourier's law,

$$q_x = -\kappa \frac{\partial T}{\partial x}, \tag{23}$$

where q_x is the heat flux in the x-direction. The thermal conductivity may be split up into its three major constituents,

$$\kappa = \kappa_{trans} + \kappa_{rxn} + \kappa_{int} \tag{24}$$

where κ_{int}, κ_{trans}, and κ_{rxn} represent the contributions from internal degrees of freedom, translational movement, and reactions effects, respectively. The strong relation between κ, the specific heat, and viscosity allows for the approximate evaluation of thermal conductivity by a Prantdl number, Pr,

$$Pr = \frac{\eta c_p}{\rho \kappa}, \tag{25}$$

where Pr is set to 0.7 in this investigation. This theory is most applicable at low temperatures, but with the input limitations of the CFD software this evaluation produces the most physical thermal conductivity model.

The mass diffusion (D) of a gas satisfies Fick's law,

$$J_{n_x} = -D \frac{\partial n}{\partial x}, \tag{26}$$

where J_n is the flux density of number density. The diffusion of electrons caused by their increased mobility must be ignored since the bulk movement of charged particles

caused by electromagnetic fields (inhibiting the electron diffusion) is not simulated. For this reason and also for computational efficiency, the diffusion model implemented invokes a constant Schmidt number, Sc,

$$Sc = \frac{\eta}{\rho D} \tag{27}$$

where D is the diffusion coefficient depending on the diffusing species and the gas mixture. The Schmidt number is set to the nominal 0.7 for all species to ensure equal diffusion, and thereby keeping the gas quasi-neutral at all locations.

3 Computational Modeling

The transport of mass, momentum, and energy are numerically modeled to time-accurately simulate the fluid phenomena induced during laser spark decay. Subsection 3.1 introduces the partial differential equations (PDEs) that are used in the mathematical modeling of fluid transport. In Subsection 3.2 the method of discretization of the PDEs over a generic control volume is discussed and shown to result in numerically solvable finite difference equations (FDEs). The fluid variables desired are found by the solution of the FDEs. The finite-element method of iteratively solving the FDEs is shown in Subsection 3.3. Subsections 3.4 introduces the kinetics mechanisms used to handle equilibrium plasmas and finite-rate combustion reactions simultaneously. Subsection 3.5 presents the spatial and temporal computational grids utilized in the simulations. The initial conditions used throughout the simulations are discussed in Subsection 3.6.

3.1 Transport Equations

In the flow of fluid that acts as a continuum, the mass fraction transport equation is written

$$\frac{\partial(\rho Y_\alpha)}{\partial t} + \frac{\partial(\rho u_j Y_\alpha)}{\partial x_j} = \frac{\partial J_{\alpha j}}{\partial x_j} + M_\alpha \omega_\alpha, \tag{28}$$

where ρ is mass density, t is time, $J_{\alpha j}$ is the diffusive mass flux of species α in the j-direction, x_i and u_i are respectively i^{th} Cartesian component of position and velocity, M_α, Y_α, and ω_α are the mass, mass fraction, and molar production rate of species α,

respectively. Summing over all species gives the nominal continuity equation,

$$\frac{\partial \rho}{\partial t} + \frac{\partial (\rho u_i)}{\partial x_i} = \frac{\partial m}{\partial t}. \tag{29}$$

The molar production rate in the mass fraction transport equation is evaluated as

$$\omega_\alpha = \sum_{n=1}^{N} \nu_{\alpha n} q_n, \tag{30}$$

where $\nu_{\alpha n}$ is the stoichiometric coefficient of the α^{th} species in the n^{th} reversible reaction step, and q_n is the rate-of-progress variable for the n^{th} reaction step. The rate-of-progress is expressed as

$$q_n = k_n^f \prod_{\alpha=1}^{N_s} \chi_\alpha^{\nu'_{\alpha n}} - k_n^r \prod_{\alpha=1}^{N_s} \chi_\alpha^{\nu''_{\alpha n}}, \tag{31}$$

where k_n^f and k_n^r are the forward and reverse rate coefficients of the n^{th} reaction step, and χ_α is the molar fraction of the α^{th} species. The forward rate coefficients are approximated to be in the Arrhenius form

$$k^f = AT^\beta e^{-E_a/RT}, \tag{32}$$

where A and β are empirical constants, R is ideal the gas constant, and E_a represents activation energy. The pre-exponential factor AT^β is the product of the collision frequency and the orientation factor. The equilibrium reverse reaction rates may be approximated by the Arrhenius form or calculated from the law of mass action

$$k^r = \frac{k^f}{K_c}, \tag{33}$$

where K_c is the equilibrium constant.

The momentum transport equation may be written

$$\frac{\partial(\rho u_i)}{\partial t} + \frac{\partial(\rho u_i u_j)}{\partial x_i} = -\frac{\partial p}{\partial x_i} + \frac{\partial \tau_{ij}}{\partial x_i}, \tag{34}$$

where τ_{ij} is the viscous stress tensor. For Newtonian fluids, the viscous stress tensor is related to the spatial velocity gradients by

$$\tau_{ij} = \eta\Big(\frac{\partial u_i}{\partial x_j} + \frac{\partial u_j}{\partial x_i}\Big) - \frac{2}{3}\eta\Big(\frac{\partial u_k}{\partial x_k}\Big)\delta_{ij}, \tag{35}$$

where η is the dynamic viscosity. Using this evaluation of the viscous stress tensor in the momentum equation gives

$$\frac{\partial(\rho u_i)}{\partial t} + \frac{\partial(\rho u_i u_j)}{\partial x_i} = -\frac{\partial p}{\partial x_i} + \frac{\partial}{\partial x_i}\Big[\eta\Big(\frac{\partial u_i}{\partial x_j} + \frac{\partial u_j}{\partial x_i}\Big) - \frac{2}{3}\eta\Big(\frac{\partial u_k}{\partial x_k}\Big)\delta_{ij}\Big], \tag{36}$$

which is commonly referred to as the Navier-Stokes equation.

The energy transport equation for a compressible fluid continuum can be written

$$\frac{\partial(\rho H)}{\partial t} + \frac{\partial(\rho u_j H)}{\partial x_j} = \frac{\partial}{\partial x_j}(\kappa\frac{\partial T}{\partial x_j}) + \frac{\partial P}{\partial t} + \frac{\partial(\tau_{ij} u_j)}{\partial x_i} - \frac{\partial(J_{\alpha j} h_\alpha)}{\partial x_j}, \tag{37}$$

where P is the pressure, H is the total enthalpy (per mass), h_α is the static enthalpy for species α, κ is the thermal conductivity from Fourier's Law, and T is the fluid temperature.

The previous transport equations can take on the general Cartesian form

$$\frac{\partial}{\partial t}(\rho\phi) + \frac{\partial}{\partial x_j}(\rho u_j \phi) = \frac{\partial}{\partial x_j}\Gamma\frac{\partial \phi}{\partial x_j} + S_\phi, \tag{38}$$

where ϕ is a generalized scalar flow variable, Γ is the effective diffusivity, and S_ϕ is the source term. Table 3 displays how each of the transport equations submits to this general form.

Table 3: The generalized scalar flow variable, ϕ, effective diffusivity, Γ, and the source term ,S_ϕ, evaluations for the mass, momentum, and energy transport equations to take the form of the generalized transport equation (Equation 38).

Transport Equation	ϕ	Γ	S_ϕ
Mass Fraction	Y_α	0	$\frac{\partial J_{\alpha j}}{\partial x_j} + M_\alpha \omega_\alpha$
Momentum	u_i	0	$-\frac{\partial p}{\partial x_i} + \frac{\partial \tau_{ij}}{\partial x_j}$
Energy	H	$\frac{\kappa}{c_p}$	$\frac{\partial p}{\partial T} + \frac{\partial \tau_{ij} u_j}{\partial x_i} + \frac{\partial J_{\alpha j} h_\alpha}{\partial x_j} + S_a$

3.2 Discretization Methods

The axial-symmetry of the laser pulse, focal irradiance pattern, and subsequent plasma formation allows the use of an axial-symmetric computational grid along the optic axis. To avoid confusion, the radial, azimuthal, and axial cylindrical coordinates will be respectively labeled as r, θ, and z and also as ζ_i with i=1,2,3. Rewriting the general transport equation in cylindrical coordinates gives

$$\frac{1}{r}\frac{\partial}{\partial t}(r\rho\phi) + \frac{1}{r}\frac{\partial}{\partial \zeta_k}\left[r\rho(\vec{V}\hat{\zeta^k})\phi\right] = \frac{1}{r}\frac{\partial}{\partial \zeta_k}\left[r\Gamma\frac{\partial \phi}{\partial \zeta_k}\right] + S_\phi \tag{39}$$

where $\vec{V}$ is velocity. The numerical integration of each term in the general transport equation over a generic control volume gives the relation between the flow value at a cell center with that of the neighboring cells. The generic control volume used in this axially-symmetric case has six cell faces represented by n, s, w, e, h, and l, and six

neighboring cell centers represented by N, S, W, E, H, and L, respectively.

Approximating the integral of the transient term in the general transport equation over an axial-symmetric control volume gives

$$\iiint_V \frac{1}{r}\frac{\partial \rho\phi}{\partial t} r dr d\theta dz = \frac{(\rho\phi V)_{t_1} - (\rho\phi V)_{t_0}}{t_1 - t_0}, \tag{40}$$

where V is the volume of the control cell and the expression in the parenthesis are evaluated at times t_1 and t_0, respectively. The times t_1 and t_0 are dictated by the temporal grid.

Integrating the convection term in the general transport equation over an axial-symmetric control volume gives

$$\sum_{j=1}^{3} \iiint_V \frac{1}{r}\frac{\partial}{\partial \zeta_j}(\rho u_j \phi) r dr d\theta dz \tag{41}$$

$$= C_e - C_w + C_n - C_s + C_h - C_l \tag{42}$$

$$= G_e\phi_e - G_w\phi_w + G_n\phi_n \tag{43}$$

$$-G_s\phi_s + G_h\phi_h - G_l\phi_l \tag{44}$$

where C_q, G_q, and ϕ_q are the convection, mass flux, and flow value at the q cell face. Since the cell value of ϕ is only known at the cell center, the face values of ϕ are interpolated. Various numerical interpolation schemes are available, each with increasing accuracy relating to decreasing stability. In compressible flow problems, the central difference scheme (second order accuracy) and the Osher-Chakravarthy scheme (third order accuracy) are typically used. The inherent computational symmetry in these methods inhibits the pseudo-numerical transport of flow variables.

These higher-order schemes may be blended with the first-order upwind scheme to obtain greater numerical stability.

Integrating the main diffusion term over an axial-symmetric control volume gives

$$\sum_j \iiint_V \frac{1}{r}\frac{\partial}{\partial \zeta_j}\left[r\Gamma\frac{\partial \phi}{\partial \zeta_j}\right] r dr d\theta dz \tag{45}$$

$$= r\Gamma_n(\phi_N - \phi_P) - r\Gamma_s(\phi_P - \phi_S) \tag{46}$$

$$+ r\Gamma_w(\phi_W - \phi_P) - r\Gamma_e(\phi_P - \phi_E) \tag{47}$$

$$+ r\Gamma_h(\phi_H - \phi_P) - r\Gamma_l(\phi_P - \phi_L) \tag{48}$$

$$= -(D_n + D_s + D_w + D_e + D_h + D_l)\phi_P \tag{49}$$

$$+ D_n\phi_N + D_s\phi_S + D_w\phi_W \tag{50}$$

$$+ D_e\phi_E + D_h\phi_H + D_l\phi_L, \tag{51}$$

where D_q is the diffusion coefficient and is defined as $r\Gamma_q$.

The source term in the general transport equation may be a function of the corresponding flow variable. It is evaluated as

$$S_\phi = m_P\phi_P + b_P, \tag{52}$$

where m_P and b_P are the slope and y-intercept of the linearized source. The evaluation of the source term uses the latest flow value.

Due to the strong connection between the pressure and velocity fields, the pressure gradient source term in the momentum transport equation is treated separately from the other source terms. Integrating the pressure gradient over a control volume gives

$$\iiint_V \left[\frac{\partial P}{\partial r} + \frac{1}{r}\frac{\partial P}{\partial \phi} + \frac{\partial P}{\partial z}\right] r dr d\phi dz = \sum_i A_i^{\perp}\Delta_i P \tag{53}$$

where $A_i^{\perp}$ is the cell face area perpendicular to the i^{th} direction and $\Delta_i P$ is the change in pressure across the control volume in the i^{th} direction.

The numerical integration of each transport equation term over the computational grid of control volumes results in a finite difference equation (FDE). Each FDE interrelates a flow variable of a cell with that at the neighboring cells, which is written

$$a_P \phi_P = \sum_Q a_Q \phi_Q + b_P, \tag{54}$$

where the sum over Q represents the sum over the neighboring cell centers, and a_Q are the link coefficients. Combining the FDE of each flow variable, a system of FDEs is formed. These FDEs give a non-linear system since the link coefficients are in general functions of the flow variables.

The mass transport equation is treated differently than the general transport equation previously described. Integrating the continuity equation over a control volume,

$$\iiint_V \left(\frac{\partial \phi}{\partial t} + \left[\frac{\partial}{\partial r} + \frac{1}{r}\frac{\partial}{\partial \phi} + \frac{\partial}{\partial z} \right] (\rho u_j) \right) r dr d\phi dz = \iiint_V \dot{m} r dr d\phi dz, \tag{55}$$

results in

$$\frac{(\rho V)_{t_1} - (\rho V)_{t_0}}{t_1 - t_0} + G_e - G_w + G_n - G_s + G_h - G_l = \dot{m} V_1. \tag{56}$$

Interpolation is required to approximate the cell face mass flux with the mass density and velocities only available at the cell center. In order to avoid the well known checkerboard instability associated with pure linear interpolation, the velocity-

pressure relation includes a third-order correction term[27]. This relation is written

$$u_q = \frac{1}{2}(u_P + u_Q) - \frac{1}{2}\Big[(\phi_P + \phi_Q)(\frac{\delta P}{\partial x_i})_q - d_P(\frac{\delta P}{\partial x_i})_P - d_Q(\frac{\partial P}{\partial x})_Q\Big], \qquad (57)$$

where d_Q=$V_1 P/a_Q$. The mass density in the mass flux term is evaluated by the second-order central difference scheme. This dicretization of the continuity equation serves as the FDE describing pressure transport in the pressure-based finite-element method.

3.3 Solution Methods

The CFD-ACE software package was selected to solve of the fluid transport equations. Specifically, the CFD-ACE solves the FDEs with a implicit whole-field solver[27]. Globally, the non-linear system of FDEs is solved by a variation of the Semi-Implicit Method for Pressure-Linked Equations Consistent (SIMPLEC)[31]. SIMPLEC iteratively solves the momentum equation and the pressure-velocity relation to find the velocity and pressure fields that approach the ideal continuity relation. The link coefficients and flow variables are iteratively solved until an acceptable error is obtained for each variable over the entire computational domain. The convergence of each flow variable is monitored by the decrease in the absolute iteration-to-iteration residual of the variable over the computational domain. The coupled and non-linear nature of the FDE system requires the use of linear under-relaxation factors and inertial under-relaxation factors to slow the iteration-to-iteration change in the flow variable. These under-relaxation schemes ensure numerical convergence to the proper set of

flow values.

Linear under-relaxation factors are used to ensure the proper convergence of the independent flow variables. The linear under-relaxation factor adjusts the same cell iteration-to-iteration change of an in dependent variable by

$$\phi = \phi^* + f\Delta\phi, \tag{58}$$

where f is the linear under-relation factor and $\Delta\phi$ is the initially desired numerical correction of the independent flow variable ϕ. Note that a factor of zero will lead to no iteration-to-iteration change in the flow value, while a factor of 1.0 will lead to no resistance in the value change.

Inertial under-relaxation is applied to the scalar flow variables, which are not defined by FDEs, but rather are related to the independent variables through algebraic relations. The inertial under-relaxation factor is applied by adding two near equal terms on each side of Equation 54,

$$(a_P + I)\phi_P = \sum_Q a_Q\phi_Q + b_Q + I\phi^*, \tag{59}$$

where I is the inertial factor. When I is set to zero, there is no resistance opposing the convergence. However, if I has a very large value, then no iteration-to-iteration change in the flow variable will take place. Typically, values of I between 0.3 and 1.0 are effective.

3.4 Kinetic Mechanisms

Due to the nature of spark decay and spark ignition, both plasma kinetics and combustion kinetics mechanisms must be modeled simultaneously for a given time step. This dual reaction mechanism is achieved through the use of a user defined subroutine.

With the mass fractions (F_i) of each species in a particular cell, the corresponding mole fractions (X_i) are calculated by Newton's method and the system of equations

$$F_i = \frac{m_i X_i}{\sum_i^{N_s} m_i X_i} \tag{60}$$

where m_i is the mass of species i, and N_s is the total number of species. If the mole fraction of electrons is greater than 0.01 in a given cell and time step, the plasma equilibrium code of subsection 2.3 is applied at the temperature and pressure values of that cell. The cell's mass fractions and mass density,

$$\rho = \frac{P}{RT} \sum_i^{N_s} X_i m_i, \tag{61}$$

are then updated with the values corresponding to the equilibrium species concentrations.

If the electron mole fraction is zero for a particular cell, then a finite-rate reaction mechanism is applied. Since the finite-rate reactions only take place in regions containing neutral species, ion-molecule reactions are not modeled. The reaction mechanism used in the simulation of laser spark decay in air is taken from Gutheil et al.[6], and involves 5 reaction steps, with the reverse reaction rates determined by the law of mass action. The reaction steps and the corresponding Arrhenius rate coefficients

Table 4: Arrhenius coefficients used in the forward N_2-O_2 reaction rates for laser spark decay simulation in air.[6] Reverse rate coefficients are determined by the law of mass action. Values of the A-coefficient are in units of m^3/kmol/s/K^β for bi-molecular reactions and m^6/$kmol^2$/s/K^β for tri-molecular reactions. Values of E_a/R are in 1/K. β is a dimensionless constant.

No.	Reaction	A[m^3,kmol,sec]	β	E_a/R[1/K]
1	$O+N_2 \longrightarrow N+NO$	$1.82 \times 10^{+11}$	0.0	38369.0
2	$O+NO \longrightarrow N+O_2$	$3.80 \times 10^{+6}$	1.0	20820.0
3	$NO+M \longrightarrow N+O+M$	$3.98 \times 10^{+17}$	-1.5	75498.0
4	$N_2+M \longrightarrow N+N+M$	$3.72 \times 10^{+18}$	-1.6	113199.0
5	$O+O+M \longrightarrow O_2+M$	$6.17 \times 10^{+9}$	-0.5	0.0

are shown in Table 4. The reaction mechanism selected to model ammonia-oxygen ignition is a reduced kinetic mechanism of the 63 step mechanism reported by Basevich and Vedeneev[7]. The CFD-ACE software restricts the number of species to 18, of which 6 are used by the charged particles in the plasma model. The remaining 12 species are determined by their significance in the 63 step mechanism as quantified from the results of the Sandia National Laboratories' CHEMKIN code[32]. The reduced kinetic mechanism involves 30 steps, with forward and reverse rate coefficients specified in the Arrhenius form. The error induced by the reduction in steps has been shown to cause negligible error in the species concentrations and flame front propagation[3]. Tables 5 and 6 show the individual steps in the ammonia-oxygen kinetic mechanism along with the Arrhenius rate coefficients used.

For cells with electron mole fractions between 0 and 0.01, the ionic concentrations are transferred to their respective atoms. The total concentration is renormalized to unity while setting the electron concentration to zero. In this manner the kinetic

Table 5: Arrhenius coefficients used in the first 15 forward and reverse reaction rates of the NH_3-O_2 mechanism.[7] Values of the A-coefficient are in units of $m^3/kmol/s/K^\beta$ for bi-molecular reactions and $m^6/kmol^2/s/K^\beta$ for tri-molecular reactions. Values of E_a/R are in 1/K. β is a dimensionless constant.

No.	Reaction	A[m^3,kmol,sec]	β	E_a/R [K]
1f	$OH+H_2 \rightarrow H_2O+H$	2.16×10^5	1.51	1726.0
1r	$OH+H_2 \leftarrow H_2O+H$	1.01×10^6	1.51	9310.0
2f	$OH+O \rightarrow H+O_2$	2.75×10^{12}	-0.816	-45.29
2r	$OH+O \leftarrow H+O_2$	5.13×10^{12}	-0.816	8303.1
3f	$OH+H \rightarrow O+H_2$	6.9×10^9	0.0	3543.0
3r	$OH+H \leftarrow O+H_2$	1.5×10^{10}	0.0	4479.0
4f	$OH+OH \rightarrow O+H_2O$	6.0×10^5	1.27	0.0
4r	$OH+OH \leftarrow O+H_2O$	6.3×10^6	1.27	8504.0
5f	$H+H+M \rightarrow H_2+M$	2.04×10^{10}	-0.31	0.0
5r	$H+H+M \leftarrow H_2+M$	1.05×10^{17}	-1.31	52838.0
6f	$O+O+M \rightarrow O_2+M$	3.60×10^9	-1.64	0.0
6r	$O+O+M \leftarrow O_2+M$	1.55×10^{17}	-1.64	60386.0
7f	$H+OH+M \rightarrow H_2O+M$	3.6×10^{10}	0.0	0.0
7r	$H+OH+M \leftarrow H_2O+M$	8.3×10^{14}	0.0	50327.0
8f	$O+H+M \rightarrow OH+M$	4.7×10^9	0.0	0.0
8r	$O+H+M \leftarrow OH+M$	1.0×10^{13}	0.0	52335.0
9f	$NH_2+H+M \rightarrow NH_3+M$	3.2×10^5	1.0	-7548.0
9r	$NH_2+H+M \leftarrow NH_3+M$	1.2×10^{13}	0.0	45793.0
10f	$NH_2+OH \rightarrow NH_3+O$	1.26×10^8	0.0	1459.0
10r	$NH_2+OH \leftarrow NH_3+O$	3.1×10^9	0.0	3070.0
11f	$NH_2+NO \rightarrow N_2+H_2O$	1.25×10^{18}	-3.2	0.0
11r	$NH_2+NO \leftarrow N_2+H_2O$	1.6×10^{19}	-3.2	61392.0
12f	$NH_2+NH_2 \rightarrow NH_3+NH$	6.0×10^{10}	0.0	5032.2
12r	$NH_2+NH_2 \leftarrow NH_3+NH$	4.3×10^{11}	0.0	12580.0
13f	$NH_2+NH \rightarrow NH_3+N$	6.0×10^{10}	0.0	2012.9
13r	$NH_2+NH \leftarrow NH_3+N$	2.8×10^{12}	0.0	13084.0
14f	$NH_3+OH \rightarrow NH_2+H_2O$	3.2×10^9	0.0	925.9
14r	$NH_3+OH \leftarrow NH_2+H_2O$	2.0×10^9	0.0	7850.0
15f	$NH_3+H \rightarrow NH_2+H_2$	3.6×10^9	0.0	4529.0
15r	$NH_3+H \leftarrow NH_2+H_2$	8.1×10^{10}	0.0	7297.0

Table 6: Arrhenius coefficients used in the second 15 forward and reverse reaction rates of the NH_3-O_2 mechanism.[7] Values of the A-coefficient are in units of $m^3/kmol/s/K^\beta$ for bi-molecular reactions and $m^6/kmol^2/s/K^\beta$ for tri-molecular reactions. Values of E_a/R are in 1/K. β is a dimensionless constant.

No.	Reaction	A[m^3,kmol,sec]	β	E_a/R [K]
16f	NH+NO $\rightarrow$ N_2+OH	1.0×10^{9}	0.0	0.0
16r	NH+NO $\leftarrow$ N_2+OH	6.6×10^{9}	0.0	47302.0
17f	NH+O_2 $\rightarrow$ NO+OH	5.1×10^{6}	0.0	0.0
17r	NH+O_2 $\leftarrow$ NO+OH	3.1×10^{6}	0.0	25161.0
18f	NH+OH $\rightarrow$ NO+H_2	1.6×10^{8}	0.56	754.8
18r	NH+OH $\leftarrow$ NO+H_2	2.5×10^{9}	0.56	35225.0
19f	NH+H $\rightarrow$ N+H_2	1.2×10^{10}	0.0	2114.0
19r	NH+H $\leftarrow$ N+H_2	5.3×10^{10}	0.0	12580.0
20f	NH+O $\rightarrow$ N+OH	6.0×10^{10}	0.0	2516.0
20r	NH+O $\leftarrow$ N+OH	1.1×10^{11}	0.0	12077.0
21f	NH+NH $\rightarrow$ NH_2+N	6.0×10^{10}	0.0	4026.0
21r	NH+NH $\leftarrow$ NH_2+N	3.9×10^{11}	0.0	7548.0
22f	N+NO $\rightarrow$ N_2+O	2.75×10^{9}	0.0	251.6
22r	N+NO $\leftarrow$ N_2+O	1.26×10^{10}	0.0	37993.0
23f	N+O_2 $\rightarrow$ NO+O	1.0×10^{10}	0.0	3774.0
23r	N+O_2 $\leftarrow$ NO+O	2.0×10^{9}	0.0	19827.0
24f	NO+NO $\rightarrow$ N_2+O_2	1.35×10^{11}	0.0	38043.0
24r	NO+NO $\leftarrow$ N_2+O_2	2.63×10^{12}	0.0	59883.0
25f	N+OH $\rightarrow$ NO+H	1.33×10^{11}	-0.25	0.0
25r	N+OH $\leftarrow$ NO+H	5.0×10^{11}	-0.25	24406.0
26f	O+NH $\rightarrow$ H+NO	6.0×10^{9}	0.0	0.0
26r	O+NH $\leftarrow$ H+NO	4.4×10^{10}	0.0	33646.0
27f	NH_2+NO $\rightarrow$ N_2+OH+H	6.2×10^{15}	-2.2	503.2
27r	NH_2+NO $\leftarrow$ N_2+OH+H	3.3×10^{8}	-1.2	2013.0
28f	H+NH_2 $\rightarrow$ NH+H_2	6.0×10^{9}	0.0	4076.1
28r	H+NH_2 $\leftarrow$ NH+H_2	3.8×10^{9}	0.0	10568.0
29f	NH_2+N $\rightarrow$ N_2+H_2	6.0×10^{9}	0.0	0.0
29r	NH_2+N $\leftarrow$ N_2+H_2	1.1×10^{11}	0.0	77495.0
30f	N+H_2 $\rightarrow$ NH_2	1.33×10^{10}	0.0	5586.0
30r	N+H_2 $\leftarrow$ NH_2	2.5×10^{16}	-1.0	41515.0

mechanism is switched from the plasma equilibrium to the multi-step, finite-rate mechanisms described above. However the calculation of cell mass density from the temperature, pressure, and mass fractions continues throughout the simulation.

3.5 Computational Domain

CFD-ACE uses the previously described finite-element approach to solve the governing transport equations on a structured grid. In this method, the flow variables are computationally approximated at the geometrical center of each control volume by numerically evaluating the transport equations. These cell-center fluid values represent the average values in the cell, and are considered valid throughout the cell. This consideration dictates the optimum cell size and thereby the geometry and density of a suitable computational grid. If the cells are too large, then the poorly defined gradients will lead to poorly resolved results. Conversely, extremely small cells will lead to superior resolution with increased computational resources and time requirements. An optimum computational grid must reasonably resolve the phenomena of interest while keeping the computational requirements to a minimum. The same ideology applies to the temporal grid in unsteady fluid problems. The requirement to sufficiently resolve the sub-millimeter structures at early times, and the super-centimeter structures of later times is accomplished with the implementation of outwardly expanding boundaries.

Utilizing the axial symmetry of the laser-induced breakdown, reduces the spatial computational domain to two dimensions. Figure 13 shows the two-dimensional axial

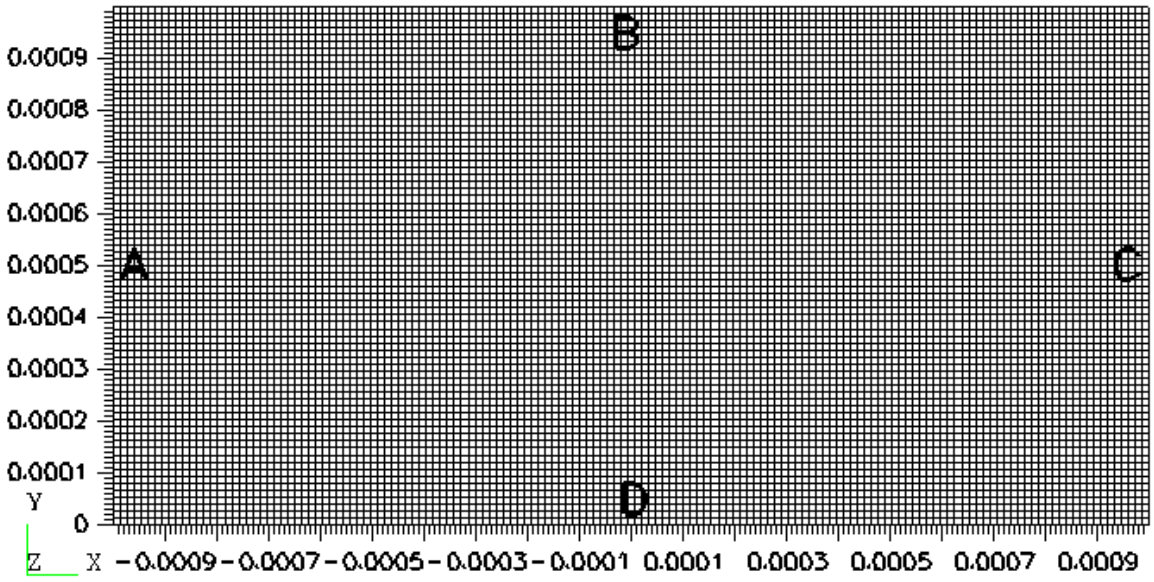

Figure 13: The computational domain at initial size. Boundaries A-C are kept with a constant temperature of 298 K, a constant pressure of 101,325 Pa, and a constant gas concentration depending on the particular simulation. Boundary D coincides with the optic axis (x-axis) and is the line of axial symmetry. The 150 by 75 grid used in the simulations are shown. The distances on the x-axis and the y axis are in units of meters.

symmetric grid used in the simulations. The x-axis (horizontal) is set to represent the optic axis of the laser pulse, and the y-axis (vertical) represents an axis that is perpendicular. Along the x-axis (D), a symmetry boundary condition is applied allowing for zero flux across the boundary. Only the positive y-axis is contained in the computational domain, splitting the two-dimensional laser spark profile in half. The remaining three boundaries (A-C) are held at a constant pressure of 101,325 Pa and temperature of 298 K. The three constant-pressure boundaries move (extending the symmetry line) in time to keep the blast wave contained within the computational domain, as needed. The motion of the boundaries is predetermined, since adaptive grid motion is not performed with the CFD-ACE software. A typical position function for modeling the constant-pressure boundary movement is

$$y(t) = x(t) = 5.3 \times 10^{-4} + 0.65 \times t^{-0.4}, \tag{62}$$

where t is the time in units of seconds, and y and x are positions in the units of meters. This function can vary depending on the particular gas species and spatial region of interest in the simulation. If the resolution of the high-temperature region is desired, the movement of the boundaries will be reduced allowing for the blast wave to leave the computational domain after sufficient pressure decay.

Each cell in the structured grid maintains an aspect ratio of one to best reduce the possibility of pseudo-numerical gas flow influencing the calculations and to aid the numerical convergence. With vortices and multi-directional flows present in laser spark decay, this better ensures the simulation of real flow effects. A typical com-

putational grid contains 150 by 75 grid points, which initially span a 2 mm by 1 mm region (see Figure 13). These initial grid specifications produce an initial grid density of about 13 μm per cell. Such an initial grid density allows for the efficient and sufficient resolution of the laser spark. The grid is rescaled at each time step as the boundaries expand the computational domain in a manner that satisfies the space conservation law [27].

To temporally resolve the laser spark decay in an efficient manner, a non-linear temporal grid is used. Starting with the initial condition set at 10 ns, each subsequent time step is calculated as fraction (f) of the total time. The temporal grid is defined by the equation

$$t_{n+1} = f \times t_n, \tag{63}$$

where t_{n+1} and t_n are two consecutive time steps, and f is the fractional value. In this work, f is set to 1.059 giving a simulation from 10 ns to 1.0 ms 200 intermediate time steps. This value was found to give reasonable convergence, however, some interesting fluid dynamic effects occurring at approximately 100 ns in time are only seen with f-values less than 1.001.

3.6 Initial Conditions

To begin solving the time-dependent system of FDEs, the initial temperature, pressure, species concentration, and velocity profiles must be specified in the computational domain. The temperature profile described in subsection 2.1 (Figure 1) is used along with the species concentrations (Figures 7 and 8) and pressure profiles (Figures

9 and 10 of subsection 2.3 corresponding to a constant mass density profile for the given initial gas mixture. For all gas mixtures considered in this investigation, the ambient temperatures and pressures at the computational boundaries are 298 K and 101,325 Pa, respectively. The initial bulk velocities are assumed to be negligible and are set to zero.

4 Laser Spark Decay in Air

In ignition, the high-temperature kernel plays a dominate role in the spatio-temporal flame front formation and propagation. For a rigorous laser spark ignition model, the time-accurate simulation of the high-temperature kernel dynamic must first be achieved without combustion reactions. The challenge of this work is to show that the propagation of the initial laser energy deposition profile induces the subsequent development of various flow phenomena characteristic to laser spark decay.

In this section, the fluid properties of Section 2 and the computational methods of Section 3 are applied to the time-accurate simulation of laser spark decay in air. The transient pressure relaxation and redistribution forming the blast wave are described along with the accompanying flow field in Subsection 4.1. In Subsection 4.2, the kernel dynamics characteristic of laser spark decay are shown to result from the initial energy deposition profile. In Subsection 4.3, attention is brought to the blast wave propagation. Comparisons are made with other blast wave models and with experimental measurements. This section concludes with the verification of the dynamic model by comparison of the predicted kernel dynamics with ultra-high speed photographs in Subsection 4.4.

4.1 Pressure Decay

The axially symmetric pressure gradient calculated in Subsection 2.3 dominates the induced fluid flow during the initial laser spark decay. The bulk velocities grow

significantly in the regions of large pressure gradients, with magnitudes as high as 3,000 m/s, causing a shift in the pressure profile. In the first tens of nanoseconds, this shift causes the peak pressure location to move down the optic axis toward the focusing lens. As the pressure decay continues, the peak pressure moves radially away from the x-axis causing the formation of a blast wave. The blast front begins with a shape closely mimicking the outline of the initial pressure profile and becomes increasingly spherical as it propagates outward.

Upon the formation of a well defined blast front ($\approx$ 100 ns) the expansion of the inner gas is uniformly outward as it reduces the pressure gradient, and subsequently relaxes the pressure profile (Figure 14). As the expansion proceeds, the motion of the inner gas over-compensates for the pressure gradients present. This over-compensation is due to the lagging relationship between the pressure gradient and the gas flux caused by the momentum field. With this effect being a function of the initial pressure gradient, the gas on the positive x-axis will over-expand itself more than that on the negative x-axis. The over-expansion will proceed until the outward momentum of the gas expansion is overcome by the induced, radially-positive, pressure gradient.

Figure 15 displays the pressure profile along with the flow field at 1.8 μs in time. At this time, the inner pressure is reduced by the expansion to ambient values and over-expands due to the momentum field. The pressure profile appears spherical and is centered near the origin. As the inner pressure continues to decrease, the induced

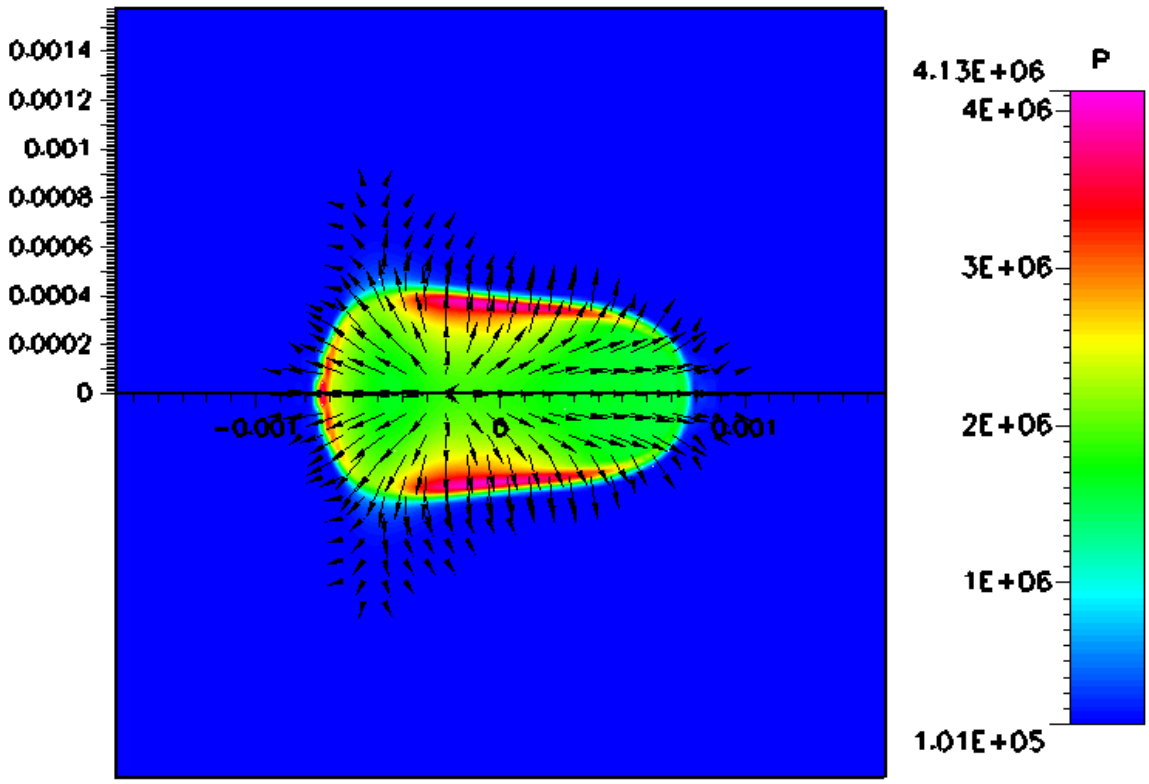

Figure 14: Computationally predicted pressure profile of laser spark decay in air at 100 ns in time. The velocity direction field is represented by arrows. Spatial dimensions along the x-axis are in the units of meters; the vertical dimension shares the same scale. The pressure values displayed are in units of pascals.

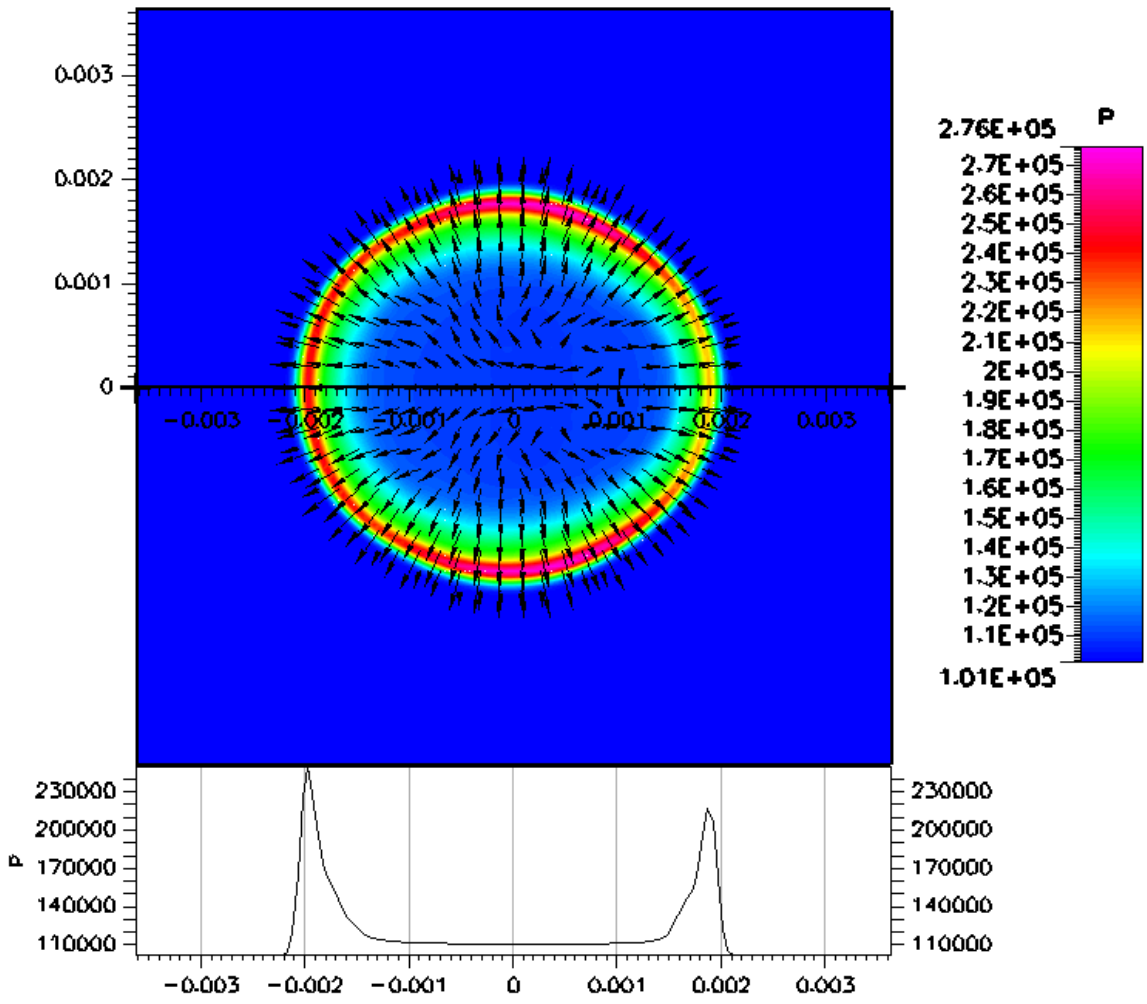

Figure 15: Computationally predicted pressure profile of laser spark decay in air at 1.8 μs in time. The velocity direction field is represented by arrows. The lower graph is the gas pressure [Pa] along the x-axis. Spatial dimensions along the x-axis are in the units of meters; the vertical dimension shares the same scale. The pressure values displayed are in units of pascals.

pressure gradient begins to revert the momentum of the gas, initiating a collapse. At 4.5 μs, the momentum field is reverted and the flow of the gas is toward the origin. Consequently, the pressure of the inner region begins to increase from its low value of $\approx$ 84,000 Pa. Due to the greater over-expansion of the right side, the induced collapse from this side dominates the flow field through the remainder of the decay. In the case of spherically- and cylindrically-symmetric sparks, the outward expansion remains symmetric, and therefore the collapsing fronts are of equal strength.

During the collapse, the two axial fronts increase and then decrease in strength, but the flow down the x-axis remains dominant throughout. This dominance is seen at 5.6 μs (Figure 16) by a leftward velocity 2-3 times greater than the opposing flow. Also at this time back-to-back vortex rings begin to strengthen, feeding off the interaction of the two opposing fronts. Eventually, the rightward front pushes completely through, and continues to flow down the x-axis. Figure 17 shows that at 32 μs, the weaker front moving up the x-axis is diverted radially as the stronger front pushes through. Due to the momentum field, the inner region at this time is slightly over-filled, giving rise to a second blast wave. With the damping of the oscillation in the inner gas pressure, further over-expansions and collapses are not computationally resolved. Figure 18 shows that after 1.0 ms the down-axis flow continues with diminishing velocity as its momentum is taken away by the stagnant air it travels through.

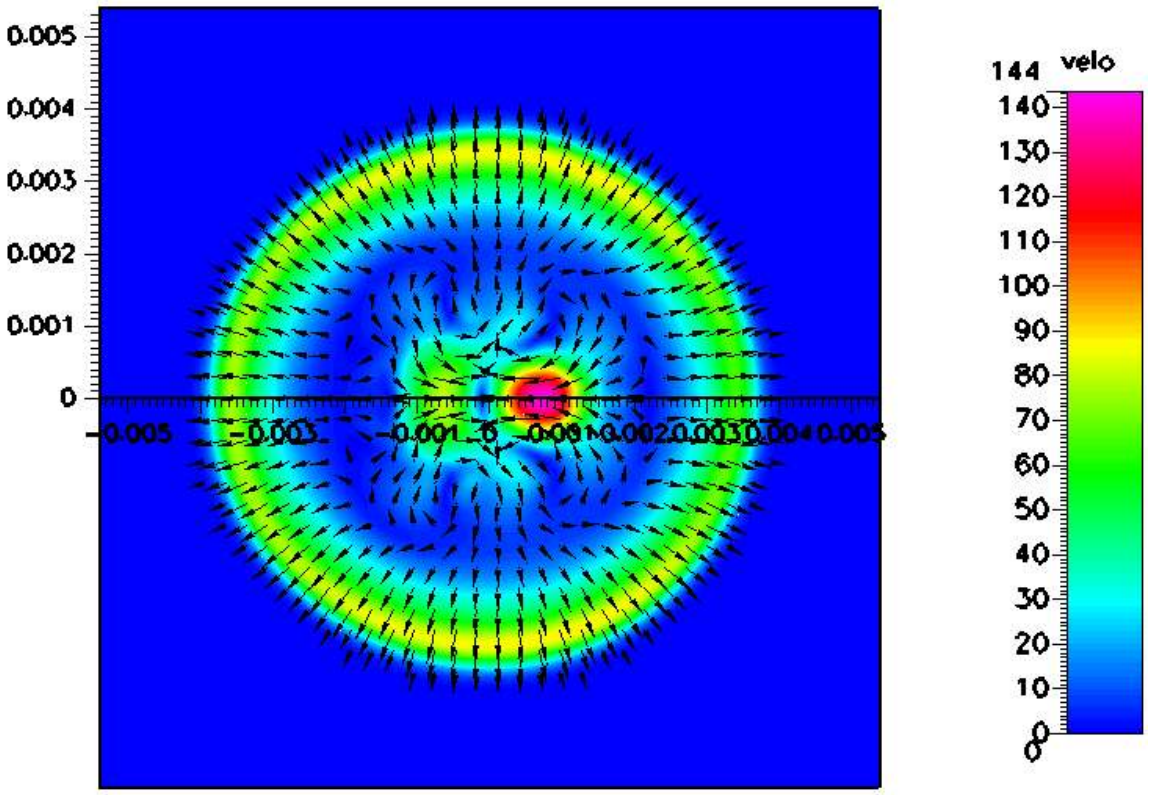

Figure 16: Computationally predicted velocity field of laser spark decay in air at 5.6 μs in time. The velocity direction field is represented by arrows. Spatial dimensions along the x-axis are in the units of meters; the vertical dimension shares the same scale. The velocity values displayed are in units of meters/second.

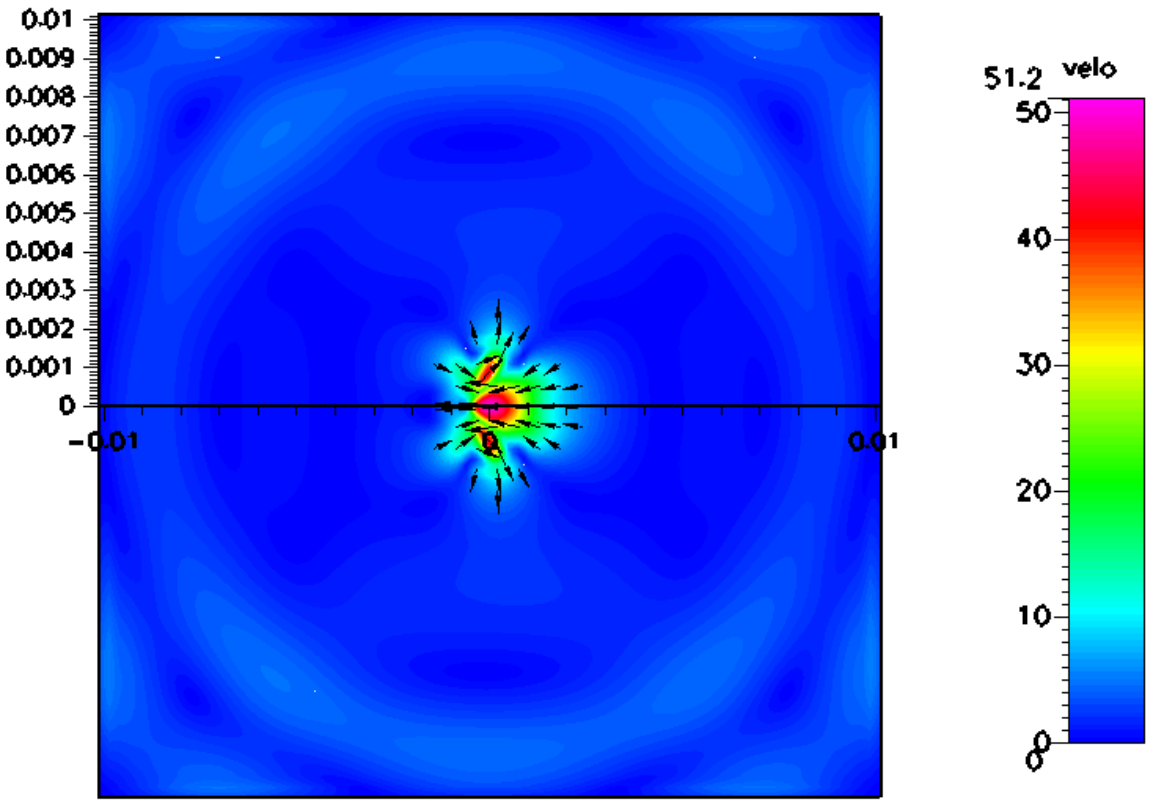

Figure 17: Computationally predicted velocity field of laser spark decay in air at 32 μs in time. The velocity direction field is represented by arrows. Spatial dimensions along the x-axis are in the units of meters; the vertical dimension shares the same scale. The velocity values displayed are in units of meters/second.

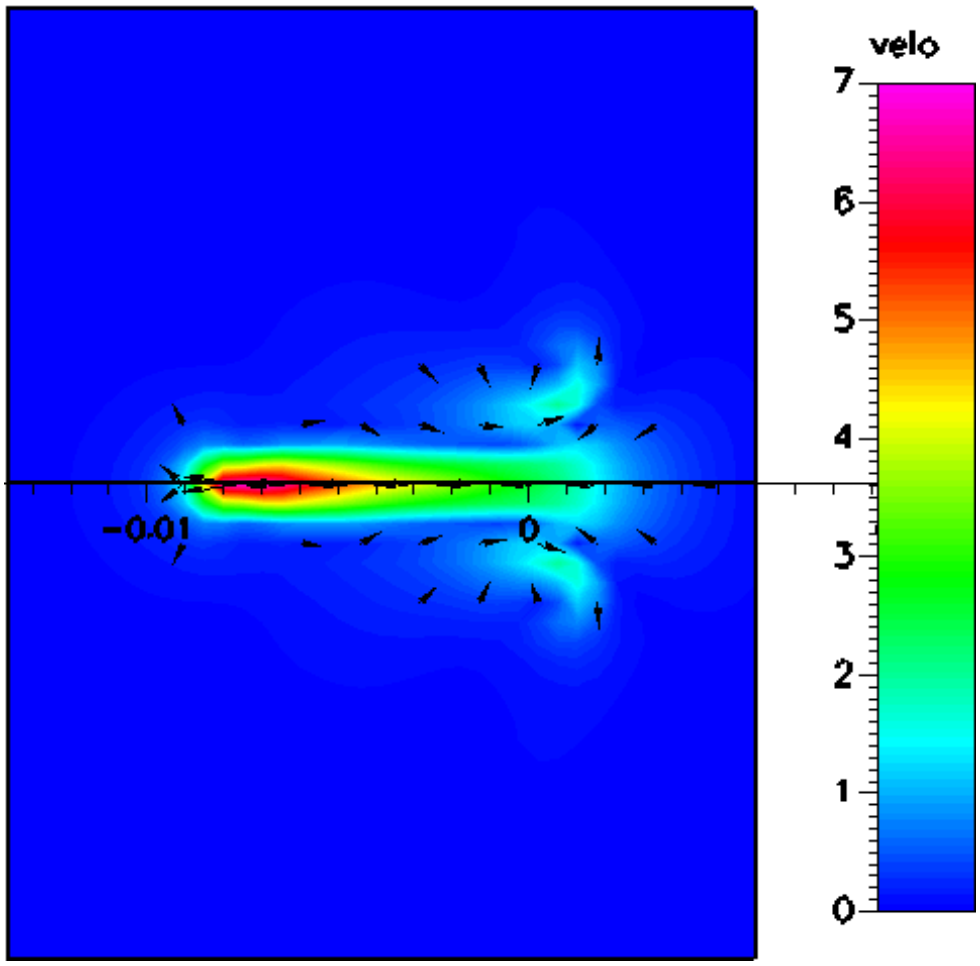

Figure 18: Computationally predicted velocity field of laser spark decay in air at 1.0 ms in time. The velocity direction field is represented by arrows. Spatial dimensions along the x-axis are in the units of meters; the vertical dimension shares the same scale. The velocity values displayed are in units of meters/second.

4.2 Kernel Dynamics

The evolution of the high-temperature kernel after the laser-induced breakdown is dominated by the expansion induced during relaxation of pressure gradients. This fast initial expansion of the high-pressure gas acts to spread the temperature profile outward and causes a sharp decrease in the peak temperature value. The effect of the initial expansion on the temperature profile over-shadows other thermal dissipation processes. Figure 19 shows the temperature profile of the kernel at 100 ns. The effects of the expansion are clearly seen by the 50% increase in the length compared with the initial profile (Figure 1). As expected, the radial kernel expansion is not uniform, with the front being expanded about twice as much as the back. At 100 ns, the well-defined blast front resides just below the surface of the kernel (compare Figure 19 with Figure 14). The kernel and blast front will separate at about 300 ns in time, but the kernel expansion continues until the gaseous collapse described in Subsection 4.1 initiates.

As collapse of the low pressure region induces gas flux down the x-axis toward the origin, the high-temperature region of the kernel is flushed to the left. This effect is seen at 1.8 μs in Figure 20 by the elongation of the peak temperature region, and the reduction of the temperature gradient on the right side. A similar effect begins on the left side as the collapse reverts that region's velocity inward. The kernel contracts along the x-axis and continues to expand radially as the left and right sides of the kernel are flushed toward the origin. Figure 21 shows that at 5.6 μs, the kernel is

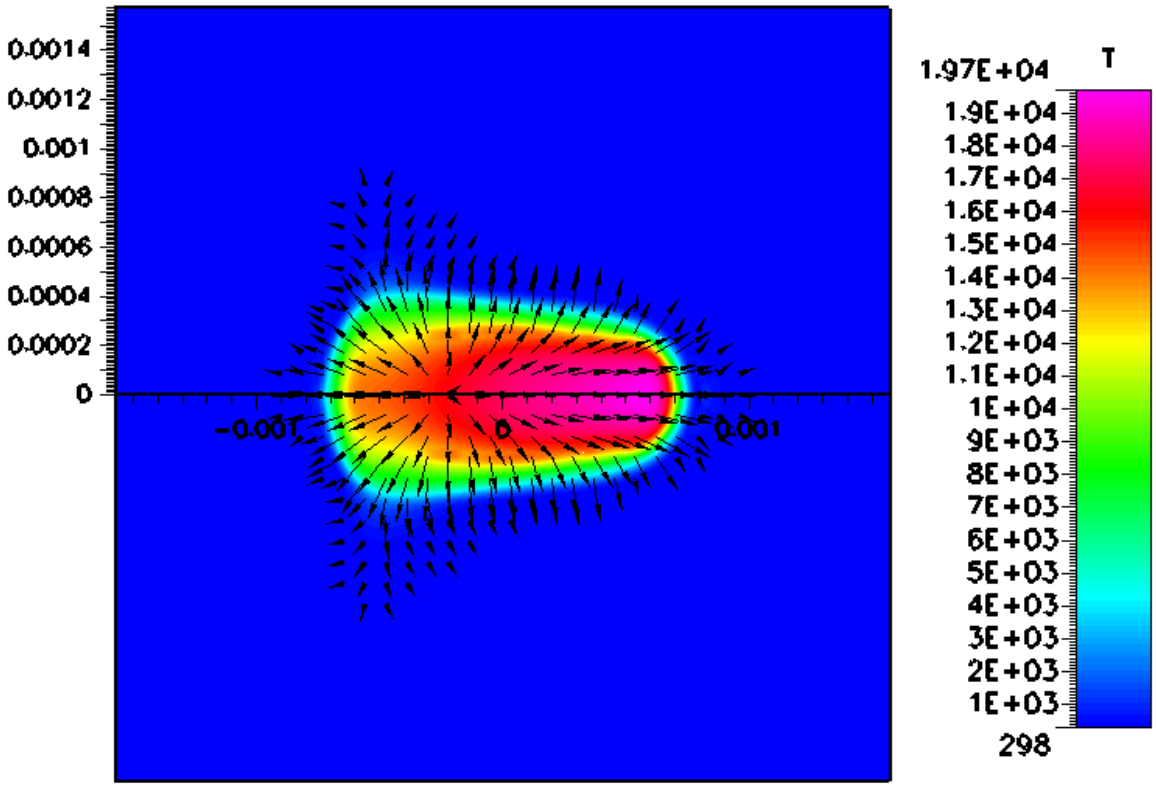

Figure 19: Computationally predicted temperature profile of laser spark decay in air at 100 ns in time. The velocity direction field is represented by arrows. Spatial dimensions along the x-axis are in the units of meters; the vertical dimension shares the same scale. The temperature values displayed are in units of Kelvin.

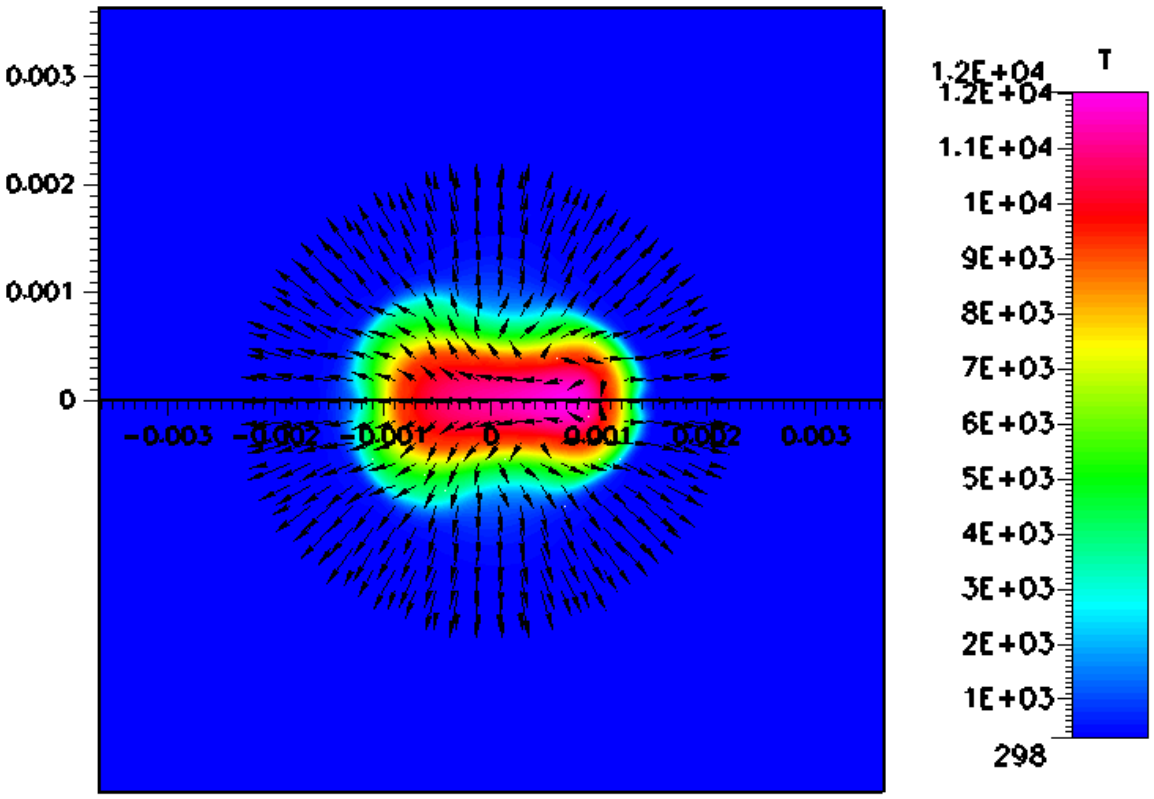

Figure 20: Computationally predicted temperature profile of laser spark decay in air at 1.8 μs in time. The velocity direction field is represented by arrows. Spatial dimensions along the x-axis are in the units of meters; the vertical dimension shares the same scale. The temperature values displayed are in units of Kelvin.

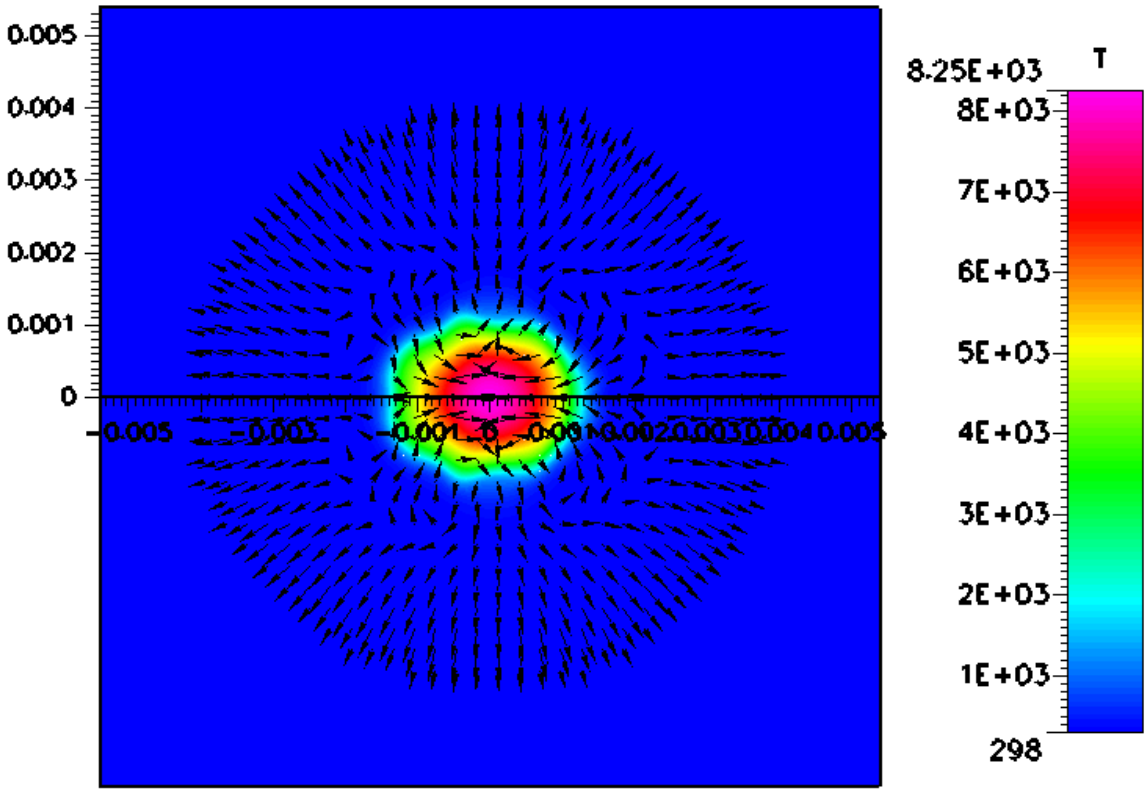

Figure 21: Computationally predicted temperature profile of laser spark decay in air at 5.6 μs in time. The velocity direction field is represented by arrows. Spatial dimensions along the x-axis are in the units of meters; the vertical dimension shares the same scale. The temperature values displayed are in units of Kelvin.

contracted to a near-spherical shape. The radial expansion seen in the region between the vortex rings is caused by the outflow of gas at the interface of the opposing fronts.

As the flow field continues to interact with the kernel, the kernel becomes increasingly compressed in the interaction region of the two colliding fronts. At 32 μs (Figure 22) the kernel is in the shape of a "C" and continues to be bent as the stronger axial front pushes through the opposing flow. Figure 22 shows the flow field acting to separate the high-temperature region of the kernel into two distinct pieces. One piece of the kernel forms a ring around the x-axis and is located at the entrance of the back-to-back vortices. The other kernel piece remains close to the x-axis and is located at the head of the dominating axial front. The two kernel regions continue to separate along the x-direction as the decay continues, but remain connected past 1.0 ms (Figure 23). The ring also expands radially during the decay as it interacts with the weakening vortices.

The re-distribution of the kernel into two pieces is strongly correlated with the width of the initial spark profile. As the initial profile is widened radially, the majority of the kernel remains on the x-axis. Conversely, the ring portion of the kernel is enhanced with a thinner initial profile. Decay with a stronger ring portion is a characteristic of most laser sparks investigated, but as in this simulation, both regions are present.

The peak-temperature temporal-decay during the simulation is shown in Figure 24 to decrease in a near-exponential manner. The decrease in temperature is slower

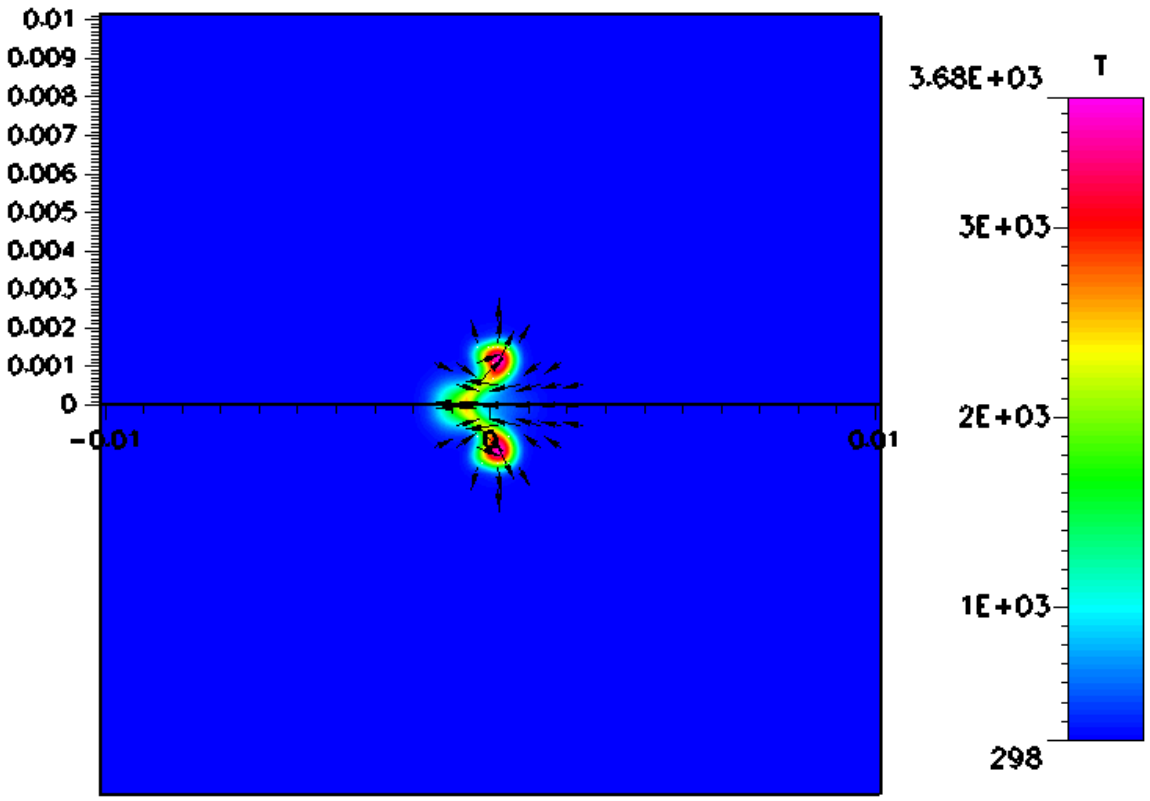

Figure 22: Computationally predicted temperature profile of laser spark decay in air at 32 μs in time. The velocity direction field is represented by arrows. Spatial dimensions along the x-axis are in the units of meters; the vertical dimension shares the same scale. The temperature values displayed are in units of Kelvin.

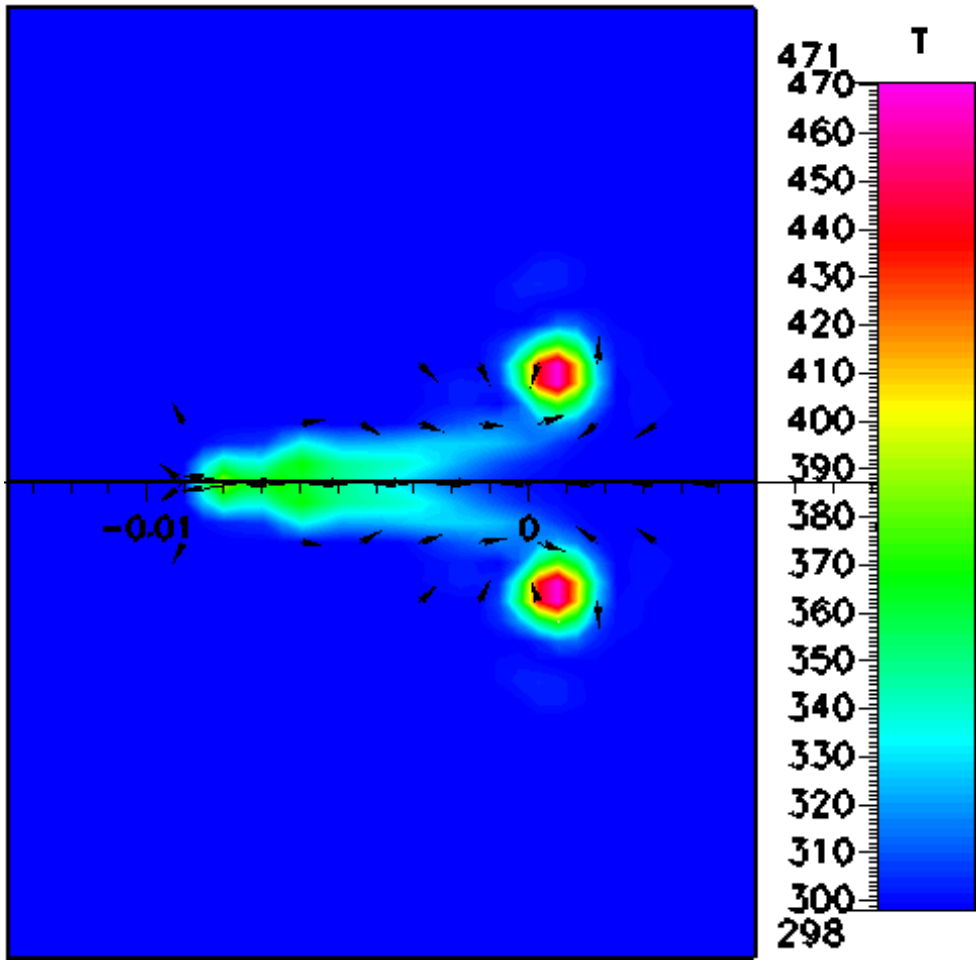

Figure 23: Computationally predicted temperature profile of laser spark decay in air at 1.0 ms in time. The velocity direction field is represented by arrows. Spatial dimensions along the x-axis are in the units of meters; the vertical dimension shares the same scale. The temperature values displayed are in units of Kelvin.

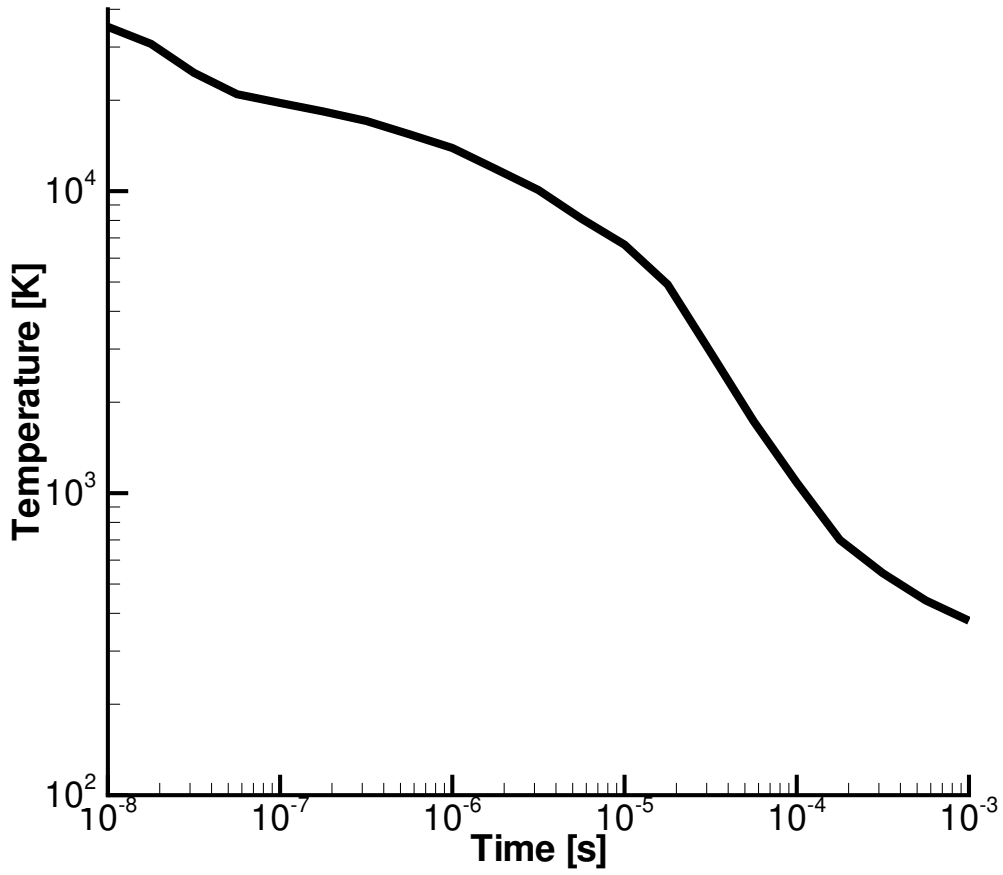

Figure 24: Temporal plot of the maximum kernel temperature predicted during laser spark decay in air. Temperature values are in units of Kelvin. Temporal values are in units of seconds.

in the 100 ns - 300 ns range. Figure 25 shows the electron number densities starting at 4×10^{25} m^{-3} to decay with similar behavior to that of the temperature decay. A possible cause for the slope increase is the slow-down in the kernel expansion as it separates from the blast front. The decay of the temperature and electron number density show similarities in magnitude and behavior with laser spark decay measurements in hydrogen gas[8].

4.3 Blast Wave Propagation

In the past, the models of blast waves have been limited to either spherical or cylindrical symmetries. It is well known that with such symmetries the fluid equations describing the propagation of a blast wave in the strong blast approximation can be analytically solved. Such a solution allows the blast wave propagation to be described by only two variables: the blast energy and the ambient mass density. This solution is referred to as self-similar, and was pioneered by Taylor[33], Sedov[34], and Brode[35]. Self-similar solutions have been used in the past as the initial condition for laser spark induced blast wave models[36–41]. Although such initial conditions have been shown to predict well the propagation of the blast wave at later times and distances far from the origin, there exist physical inconsistencies.

The first inconsistency with self-similar initial conditions is the implementation of the incorrect initial geometry of the laser spark. As shown in Subsection 4.1, the initial asymmetry caused by the breakdown processes leads to many interesting fluid phenomena, none of which can be described completely by spherical or cylindrical

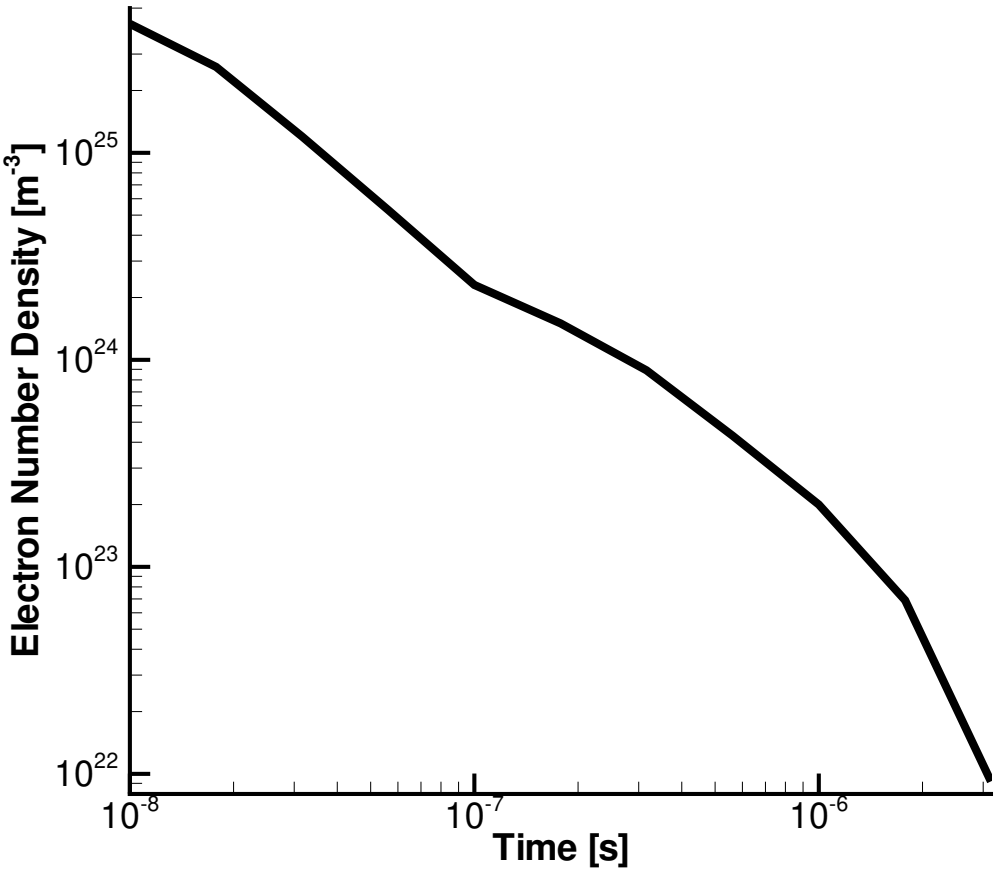

Figure 25: Temporal plot of the maximum kernel electron number density predicted during laser spark decay in air. Number density values are in units of inverse cubic meters. Temporal values are in units of seconds.

sources. Also the blast wave pre-exists in the initial condition and therefore the blast wave formation is not modeled but assumed.

The second inconsistency is the unrealistic values assigned by the self-similar solution to the gas at the geometrical center of the blast. The assigned temperatures are unrealistically high due to the near-zero mass density. This unrealistic assignment of fluid quantities leads to the inability to properly predict the kernel development and the secondary blast wave. Additionally, the effects of dissociation and ionization are typically ignored by the acceptance of a fixed adiabatic constant. Steiner et al.[39, 40] and Loeb et al.[41] both show results of models which include dissociation and ionization energy storage effects, however both models are limited to the radial-dimension in spherically or cylindrically symmetric cases.

The model presented in this work improves on the past models by the use of realistic geometry and fluid values based on the breakdown processes. The realistic initial conditions specific for the particular laser spark of interest contains no bulk velocities, thus allowing for the computation of the blast wave formation as well as the subsequent propagation. Most importantly, this model permits calculation of the fraction of spark energy that is dissipated by the formation of the blast wave.

As described in Subsection 4.1, a blast wave is formed during the initial stages of the laser spark decay, and propagates outward through time. The computational and experimental blast wave radii are compared in Figure 26. The computational radii are approximated by the peak pressure location of the blast wave along the y-axis (center

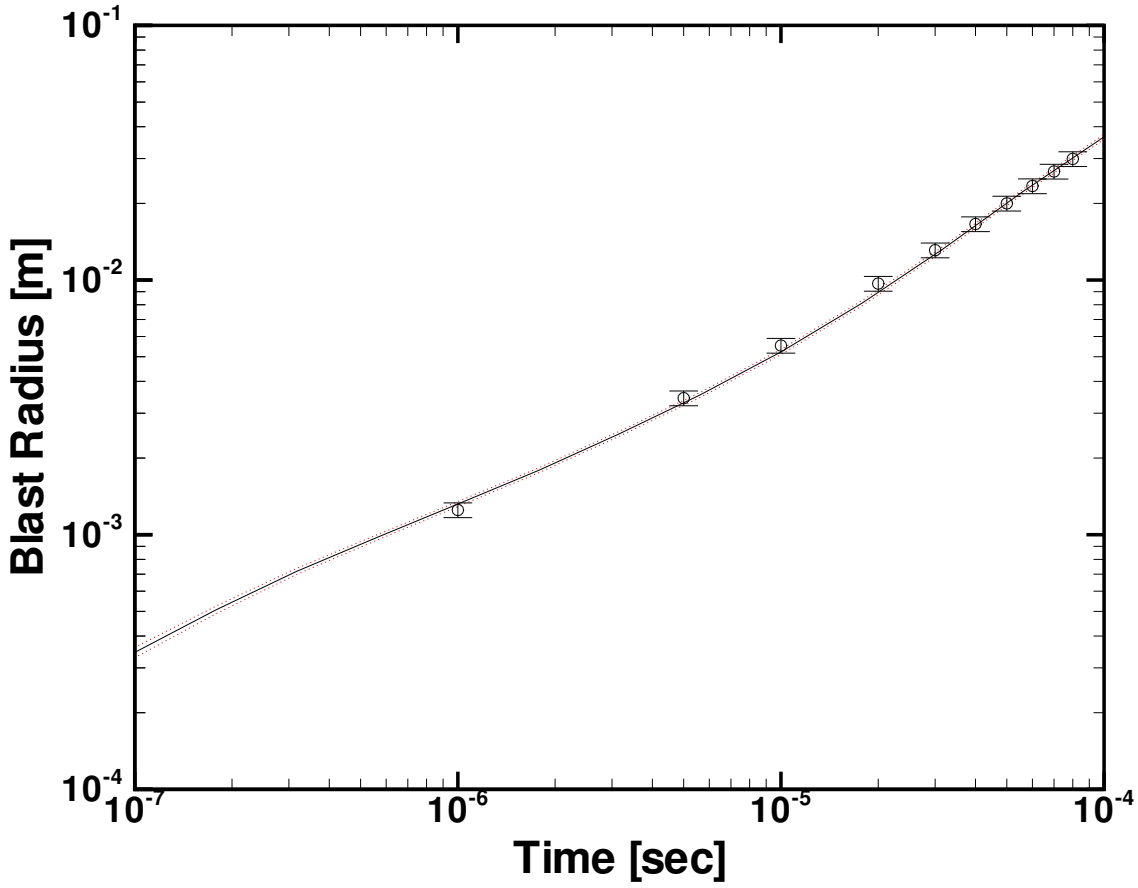

Figure 26: Comparison of the predicted blast wave radius (black line) with experimental measurements (circles with error bars)[2]. The red lines represent a one-cell-width deviation from the predicted blast wave radius. Blast wave radii are in units of meters. Temporal values are in units of seconds.

line). The two outer lines are separated one cell width apart from the calculated blast radius. The experimental data points and error bars are extracted from ultra-high speed photography of laser spark decay in air[2]. A factor of 2.5 difference in the computational and experimental spark energies arises from the length, width, and saturation temperature imposed on the initial laser-spark temperature-profile. Despite the difference in the computational and experimental laser spark energy, the agreement between the results is superb over several orders of magnitude in time. Due to the eventual decay of the blast wave into a sound wave, the agreement is expected to continue for greater times. It is noteworthy that neither the experimental nor computational blast wave propagation is modeled accurately by the Taylor equation. Deviation from the Taylor model is due to the initial lack of spherical symmetry and the unsatisfied strong blast wave-pressure condition for times greater than 700 ns.

The blast wave front becomes increasingly spherical as it propagates outward in time. The asymmetry in the blast front is quantified by

$$A = \frac{r_x - r_y}{r_y}, \tag{64}$$

where A is the parameter quantifying the spherical asymmetry, and r_x and r_y are the blast radii along the optic axis and a radial axis, respectively. Perfect spherical symmetry is represented by $A = 0$, and any non-zero value signifies an asymmetric deformation of the blast front. The position of the blast front in the x and y directions is approximated by the peak pressure location. Due to the effects of numerical diffusion and the various energy dissipation mechanisms, this blast front marker is

merely a systematic method of approximation. Figure 27 shows the temporal asymmetrical behavior of the blast wave decreasing with time until 2 μs when the blast wave is nearly spherical. The oscillations in the asymmetry at late times shows that the precision of the blast front marker is approximately 3%.

With the pressure not satisfying the strong blast wave condition at times when the wave is nearly spherical, the self-similar model does not apply. However, the non self-similar numerical approximation of Sedov [34] takes into account the counter-pressure of the ambient environment. The Sedov model defines the dimensionless length (l) and dimensionless time (τ) for a spherically-symmetric blast as

$$l = r_s \left(\frac{P_1}{E_0} \right)^3, \tag{65}$$

and

$$\tau = t E_0^{-\frac{1}{3}} \rho^{-\frac{1}{2}} P_1^{\frac{5}{6}}, \tag{66}$$

respectively. With a relation between $l(r_s,E_0,P_1)$ and $\tau(t,E_0,\rho,P_1)$ given by numerical solution [34], the energy (E_0) required to drive a blast wave to a radius (r_s) at a time (t) in a gas with an ambient pressure (P) and ambient mass density (ρ) may be calculated. Table 7 displays the relation between the dimensionless variables as calculated by N. S. Mel'nikova, V. P. Korobeinikov, and E. V. Riazanov and reported by Sedov[34]. Numerically solving these equations along with linear-interpolation of Table 7 results in the evaluation of the blast energy as a function of the time and blast wave radius. This model gives a blast source energy calculation that is very sensitive to the blast radius at a given time. Using the predicted near-spherical blast wave

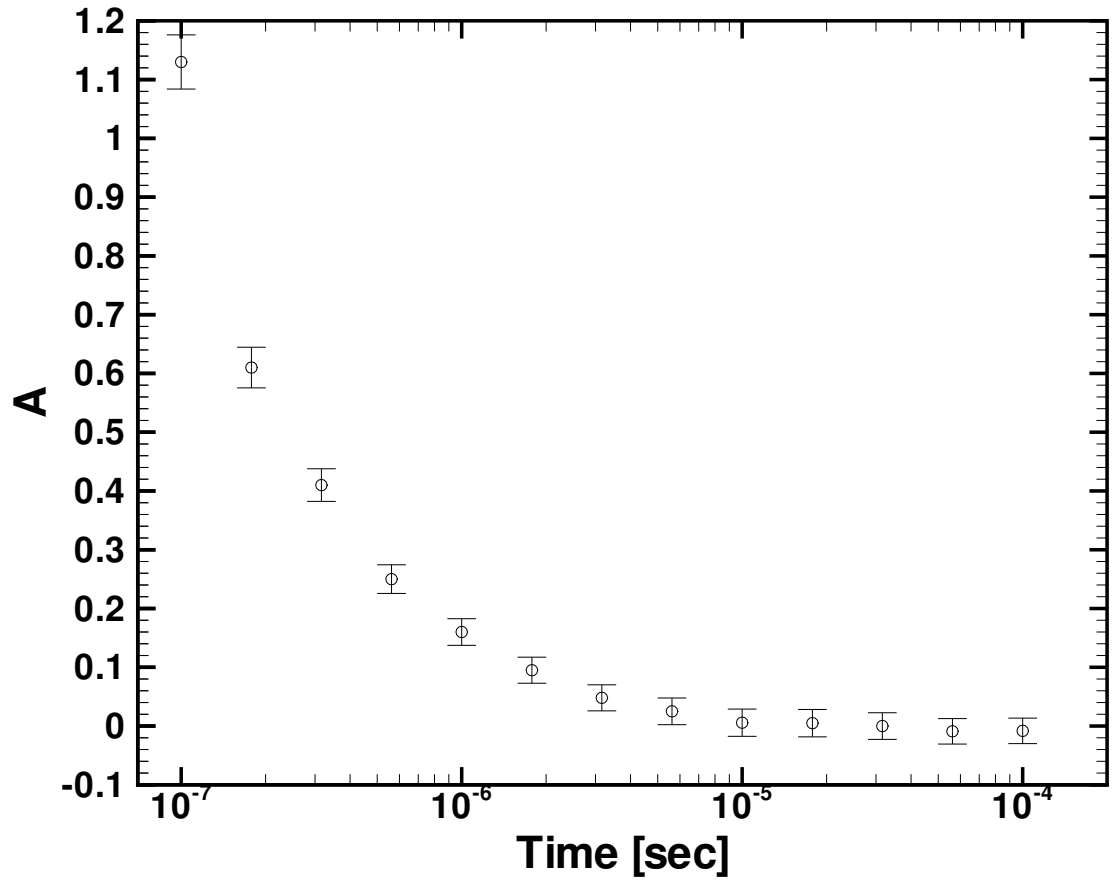

Figure 27: Temporal evolution of the blast front asymmetry quantified by the dimensionaless parameter A (see Equation 64). Temporal values are in units of seconds.

Table 7: The numerically evaluated relation between the dimensionless radius (l) and dimensionless time (τ)of the Sedov blast wave model including counter-pressure (P_0).

l	τ	P_1/P_0
0.1867	0.01403	21.1
0.2669	0.03230	10.31
0.3342	0.05431	4.967
0.4890	0.1231	3.056
0.6003	0.1842	2.321
0.6812	0.2333	2.010
0.7566	0.2807	1.835
0.9566	0.3667	1.615
0.9801	0.4323	1.521
1.2524	0.6296	1.338
1.3210	0.6811	1.315
1.5171	0.8299	1.255
1.8751	1.1080	1.185
2.3222	1.4636	1.136
2.8641	1.8973	1.102
3.6983	2.7763	1.066
7.0791	5.3764	1.032
9.6424	7.5180	1.022

radii in the 10.0 - 20.0 μs time range gives a blast energy value of $3.5^{+0.6}_{-0.5}$ mJ. With 9.2 mJ of absorbed laser energy, the source energy-blast energy coupling parameter is $3.5^{+0.6}_{-0.5}$/9.2 or $0.38^{+0.7}_{-0.5}$. Due to the sensitivity of the radii values on the blast energy calculation, the experimentally measured radii predict invalid and unrealistic energies over the domain of radii represented by the experimental error bars.

The outward flux of the gas in the region of the initial laser spark causes a decrease in pressure of the region. In the spherically symmetric case, the collapse produces a negative radial velocity, which is predicted by the Sedov model to begin around $\tau \approx 0.432$, which corresponds to $4.8^{+0.3}_{-0.2}$ μs in the case of a $3.5^{+0.6}_{-0.5}$ mJ blast source. In the case of the laser spark, this collapse is not spherically symmetric. The high-temperature region in which the laser pulse energy was deposited maintains an asymmetric profile, resulting in an asymmetric collapse. Figure 28 shows the temporal change of the pressure at a specific point in the inner gas over time. The initial decrease in pressure of the inner gas is predicted to drop below the counter pressure of one atmosphere. Eventually the pressure difference between the inner gas and the counter pressure overcomes the outward momentum of the inner gas, resulting in a collapse. The collapsing flow field is predicted to initiate around 4.5 μs by the accompanying increase in the inner gas pressure. This time of the gas collapse is in very good agreement with the Sedov model prediction of the spherically symmetric case. It is interesting to note that the secondary blast wave caused by the collapse will not be properly predicted if the initial conditions and subsequent inner gas flow

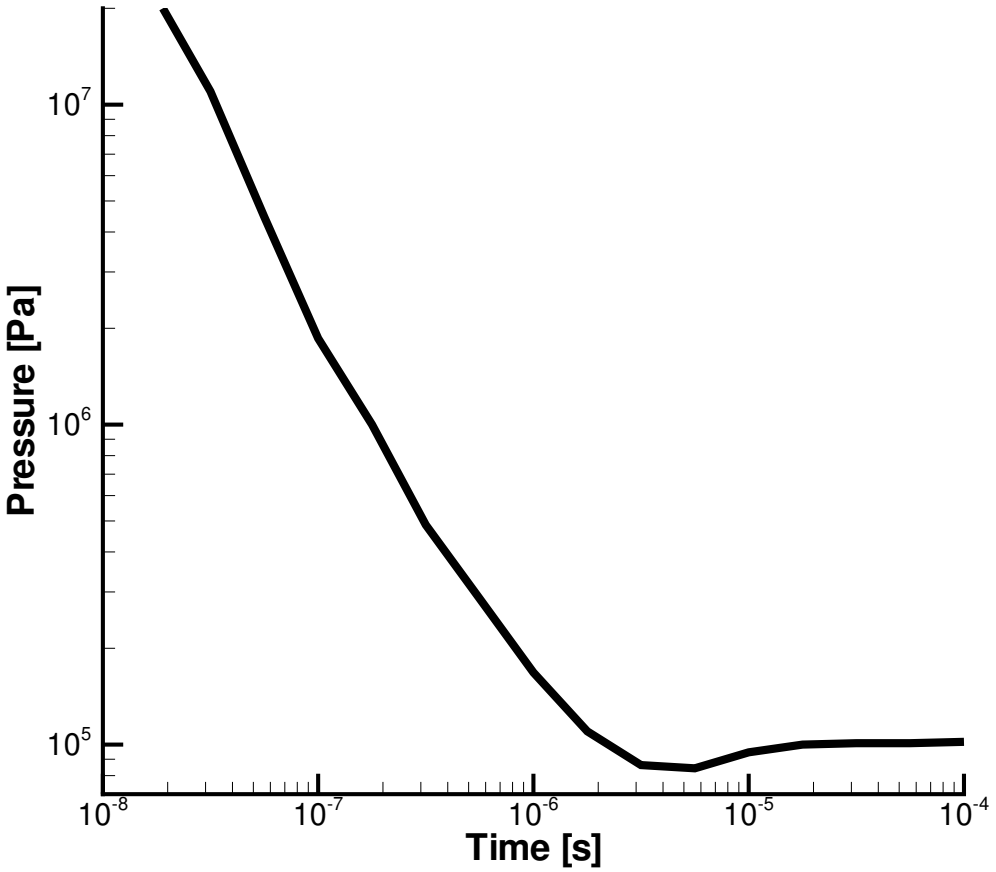

Figure 28: Pressure history of the point located at the origin of the x-axis and y-axis. Pressure values are in units of pascals. Temporal values are in units of seconds.

values were unrealistic, as in the self-similar Taylor model.

4.4 Shadowgraph Comparison

The time-accurate predictions of the kernel dynamics and temperature decay compare very well with previous planar laser-induced fluorescence measurements made by Chen[4] and Raman scattering measurements made by Nassif and Huwel[42]. However, to best determine the ability of the computational model to predict the experimentally measured dynamics, ultra-high speed shadowgraphs are experimentally recorded and compared with synthetic shadowgraphs. In particular, the ability of the model to time-accurately predict the axial collapse and the subsequent flow toward the lens would qualify the asymmetry of the laser-induced breakdown model and give insight into laser spark ignition phenomena. The use of synthetic and experimental shadowgraphs allows for the time-resolved comparison of the temperature, pressure, and mass density profiles simultaneously. The laser-spark energy used in the experimental shadowgraph investigation is ≈40 mJ, which is about 4 times larger than that simulated.

A shadowgraph is a measure of the linear displacement of a light ray as it passed through a medium. With the first-gradient of the refractive index determining the deflection of a light ray, the second-gradient describes the deviation of initially parallel light rays propagating through a non-uniform medium. The relative luminosity (I) of a shadowgraph (assuming small deflection angles) is modeled by[43]

$$I(x,y) = S\int_{z_0}^{z_1}\left(\frac{\partial^2 n}{\partial x^2}+\frac{\partial^2 n}{\partial y^2}\right)dz, \tag{67}$$

where z is the direction of the light source, n is the index of refraction and S is a scaling factor. The axially symmetric computationally predicted refractive index profile is determined by applying axial symmetry to the pressure and temperature profiles and the relation[5]

$$n = \frac{P[1 + P(334.5 - T) \times 10^{-10}]}{351.8T}(n_0 - 1) + 1, \tag{68}$$

where n_0 is the index of refraction of air at 288.2 K and 101325 Pa, and temperature and pressure are in MKS units. For a light source with a wavelength of 510 nm in vacuum, n_0 for air is taken to be $1+2.6928\times10^{-4}$[5]. The pressure and temperature dependence of the refractive index is related to the number density of the gas as expected.

The synthetic shadowgraphs are calculated by Equation 67 with the predicted three-dimensional refractive index profiles. The second derivatives in the integrand of Equation 67 are numerically evaluated to 4^{th} order. The integral is converted into a Riemann sum of the integrand, evaluated on parallel planes, each perpendicular to the z-axis (out-of-the-page). The parameter S in Equation 67 is set to allow the shadowgraph intensity to optimally span the gray scale output.

Figure 29 displays the experimental and computational shadowgraphs at 5 μs. Both the synthetic and experimental shadowgraph show the deformations of the refractive index caused by the blast wave and the high-temperature, low-pressure inner gas region. The horizontal structure is caused by the limited resolution of the computational grid as the deformation caused by the blast wave is rotated three-

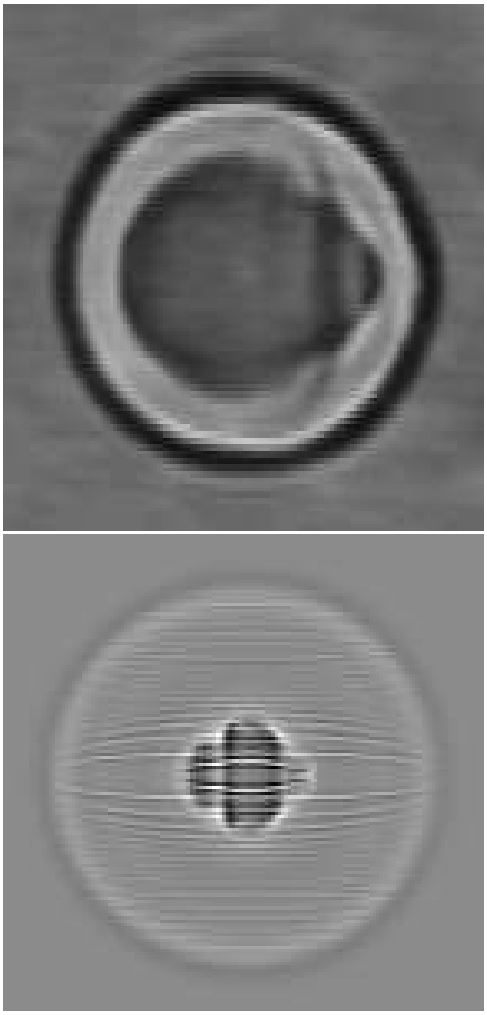

Figure 29: Experimental (top) and computationally predicted synthetic (bottom) shadowgraph of laser spark decay in air at 5 μs in time.

dimensionally. Additionally, noise is induced during the evaluation of the second derivatives. The affect of this noise is reduced by the Riemann sum.

Figure 30 displays the experimental and computational shadowgraphs at 100 μs. Both shadowgraphs show the effects of the dominating axial collapse. The axial collapse toward the lens is shown to have pushed through the weaker opposing flow. Additionally, the weaker axially collapsing front moving away from the lens has been pushed aside and now gives momentum to the back-to-back vortex structure. This vortex structure is seen in both shadowgraphs as the vertically positioned axially symmetric toroidal structure. The flow field induced by a decay of a 25 mJ laser spark has been experimentally shown to have a structure similar to that of the 40 mJ case. However, the toroidal structure developed with the lesser spark energy has a toroidal structure that is more narrow[2]. This trend is in agreement with the computational shadowgraphs.

Figure 31 displays the experimental and computational shadowgraphs at 500 μs. In both shadowgraphs, the gas flow toward the lens is seen to have continued. At this point in time, the lens-ward propagation has slowed down to approximately 9 m/s. In experiments, the flow pattern is soon overcome by chaotic motion in its last stage of decay. The comparison between the two shadowgraphs remains superb at this time despite the now large time delay from the initial laser spark profile description. The agreement at late times shows the importance of the initial modeling of the laser energy deposition and the propagation of the asymmetry through out the time-

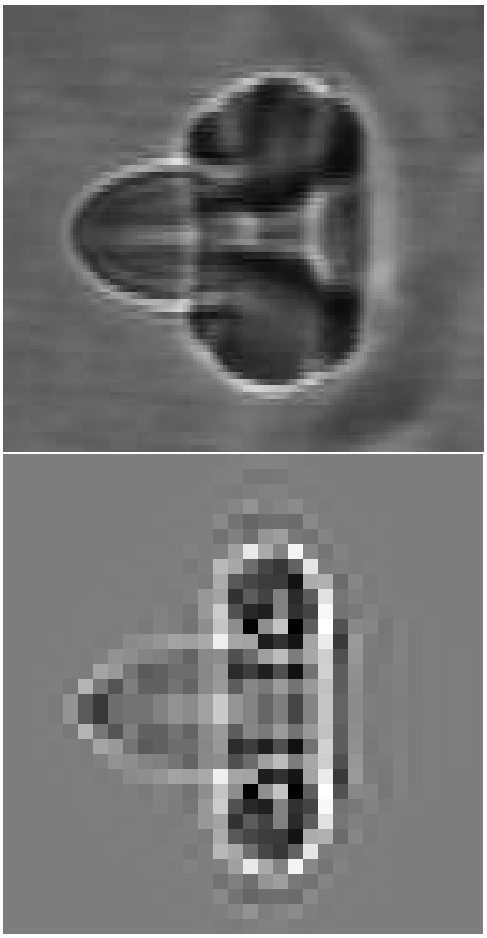

Figure 30: Experimental (top) and computationally predicted synthetic (bottom) shadowgraph of laser spark decay in air at 100 μs in time.

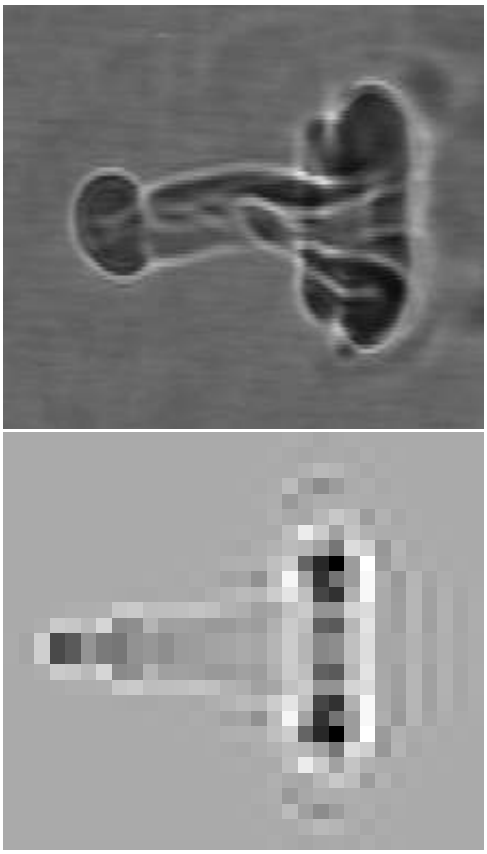

Figure 31: Experimental (top) and computationally predicted synthetic (bottom) shadowgraph of laser spark decay in air at 500 μs.

accurate model.

Due to the relaxation of the pressure profile at later times, the temperature and density are strongly related by the ideal gas law. Thus, it is not surprising that the temperature profiles and the characteristic pattern visualized by the shadowgraphs are similar.

5 Laser Spark Decay in Ammonia-Oxygen Mixtures

In Section 4, the computational ability to simulate laser spark decay in non-combustible gases was verified. In this section, an additional level of complexity is added to the model as laser spark ignition of combustible mixtures is investigated. Specifically, the temperature-triggered finite-rate energy release into the flow field is simulated for ammonia-oxygen mixtures at various fuel equivalence ratios (ϕ). Ammonia-oxygen mixtures are chosen due to their reduced number of reactions steps required for proper modeling ($\approx$30) compared with that of the hydrocarbon combustion (100+). Additionally, the abundance of experimental data for laser ignition of ammonia-oxygen mixtures allows for the verification of the computational model, as well as to give insight to experimental measurements. The global ammonia-oxygen stoichiometric reaction is

$$4NH_3 + 3O_2 \rightarrow 2N_2 + 6H_2O \tag{69}$$

and has an enthalpy of reaction of -5.5$\times 10^7$J/kg. This value of the enthalpy of reaction is primarily due to the extreme stability of H_2O (ΔH_f^0 = -1.34$\times 10^7$ J/kg). As H_2O is formed during combustion, the enthalpy of reaction is added to the static enthalpy of that region, causing an increase in temperature. Due to the spatial and temporal dependence on the production of H_2O, the enthalpy added to the flow field is non-uniform and dynamic. The chemical kinetics model is identical to that used in the simulation of the laser decay in air, with the exception that the multi-step finite-rate

coefficients are those of Tables 5 and 6. The major advantage of the kinetics model developed in this work is the simultaneous modeling of the equilibrium plasma in the ionized regions of the kernel and the combustion reactions in the neutral regions. Such a model is necessary for the proper calculation of flame-front-blast-front interactions.

The simulation of laser spark decay with the dynamic enthalpy source is investigated in Subsection 5.1 for a stoichiometric ammonia-oxygen mixture (ϕ=1.0). In Subsection 5.2, simulation results of laser spark decay in ammonia-oxygen mixtures with various fuel equivalence ratios are reported. The temperature, species concentrations, and pressure profiles used in modeling the initial laser spark in ammonia-oxygen mixtures are those which were developed in Section2. Additionally, the transport models described in Subsection 2.4 are used for each mixture. The simulation results are compared with experimental measurements in Subsection 5.3.

5.1 Stoichiometric Laser Spark Ignition

At early times, the relaxation of the initial high-pressure profile is nearly identical with that of the laser spark decay in air. As the temperature profile expands, H_2O begins to form in the regions with temperature $\approx$ 3,000 K. However, due to the enthalpies on the order of 10^8 J/kg in the high-temperature plasma, the enthalpy of reaction of the ammonia combustion is inconsequential. At 100 ns, Figure 32 shows that the H_2O forms between the low-temperature NH_3-O_2 mixture and high-temperature neutral species. At this time, the high-concentration region of H_2O is located at the blast front.

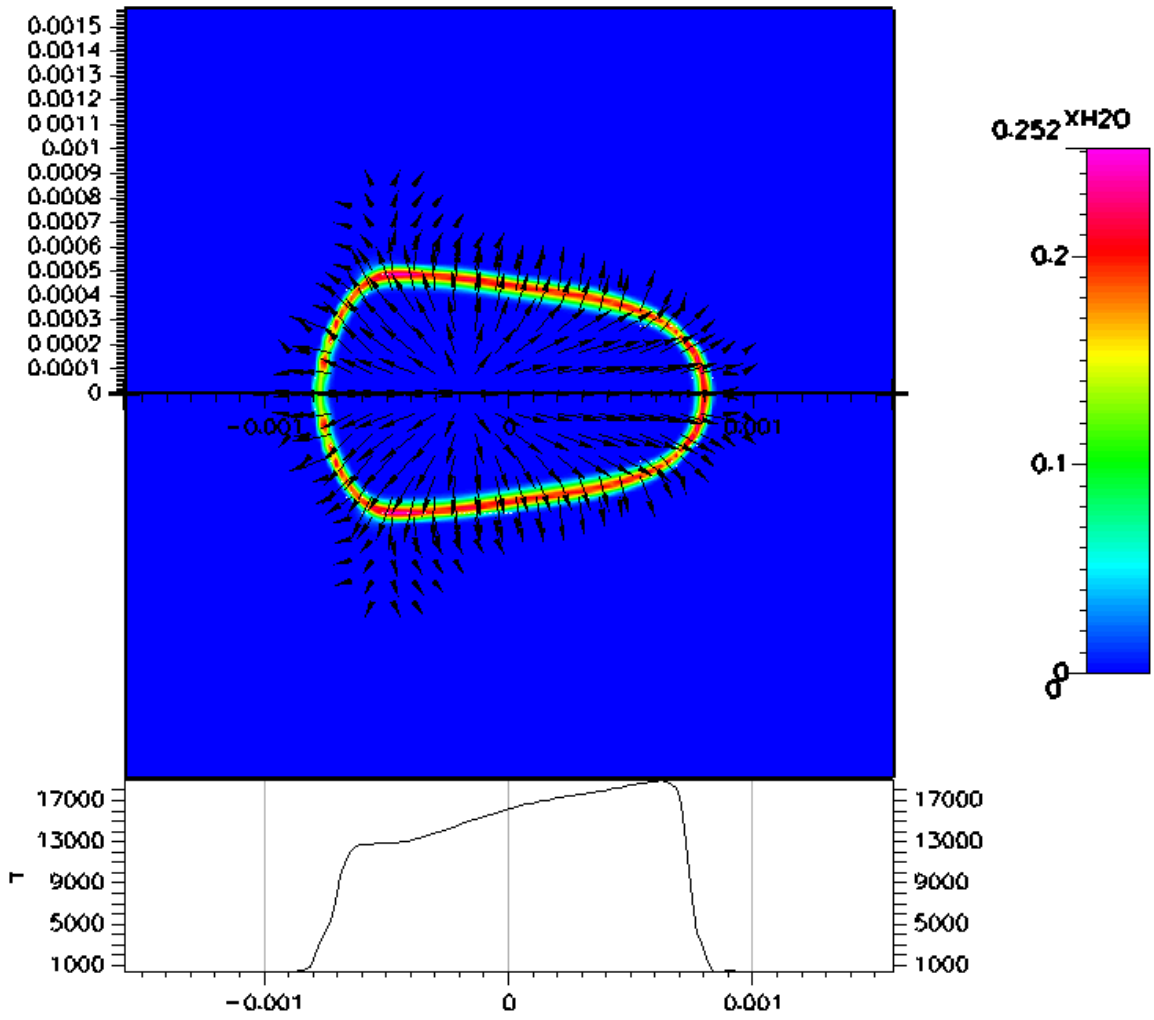

Figure 32: The molar concentration profile of H_2O at 100 ns. The bottom graph depicts the temperature along the x-axis in units of Kelvin. The distances on the x-axis and the y axis are in units of meters.

As the blast wave continues its expansion, it separates from the shell of H_2O at around 300 ns. Both become increasingly spherical as they expand. However, due to the non-spherical temperature profile, the H_2O concentration becomes weaker in high temperature gradient regions. This effect is shown in Figure 32 by the weaker H_2O concentration on the positive x-axis where the temperature gradient is highest. In the radial regions, the H_2O is enhanced due to the larger spatial region with combustion-favorable temperatures.

The static enthalpy of the kernel decays accordingly, as the kernel temperature decreases due to expansion and thermal conductivity effects. The decay of the temperature profile allows for increased formation of H_2O, and the subsequent enthalpy of reaction is added to the flow field. Figure 33 shows that at 2.4 μs the peak static enthalpy of the decaying kernel is about equal to that of the reaction. With the addition of the enthalpy of reaction in the periphery of the kernel, the reactants begin to be preheated and the H_2O concentration strengthens and expands. The strengthening is shown at 5.6 μs in Figure 34 by the relative increase of H_2O concentration on the positive x-axis. The temperature profile also becomes increasingly spherical at this time as the axial-collapsing fronts compress the elongated kernel. This effect is indicated in Figure 34.

As the compression of the kernel continues, the temperature profile begins to take on the shape of the interaction region. However, unlike the case of the non-ignition simulation, the temperature drop that occurs during the interaction of the two fronts

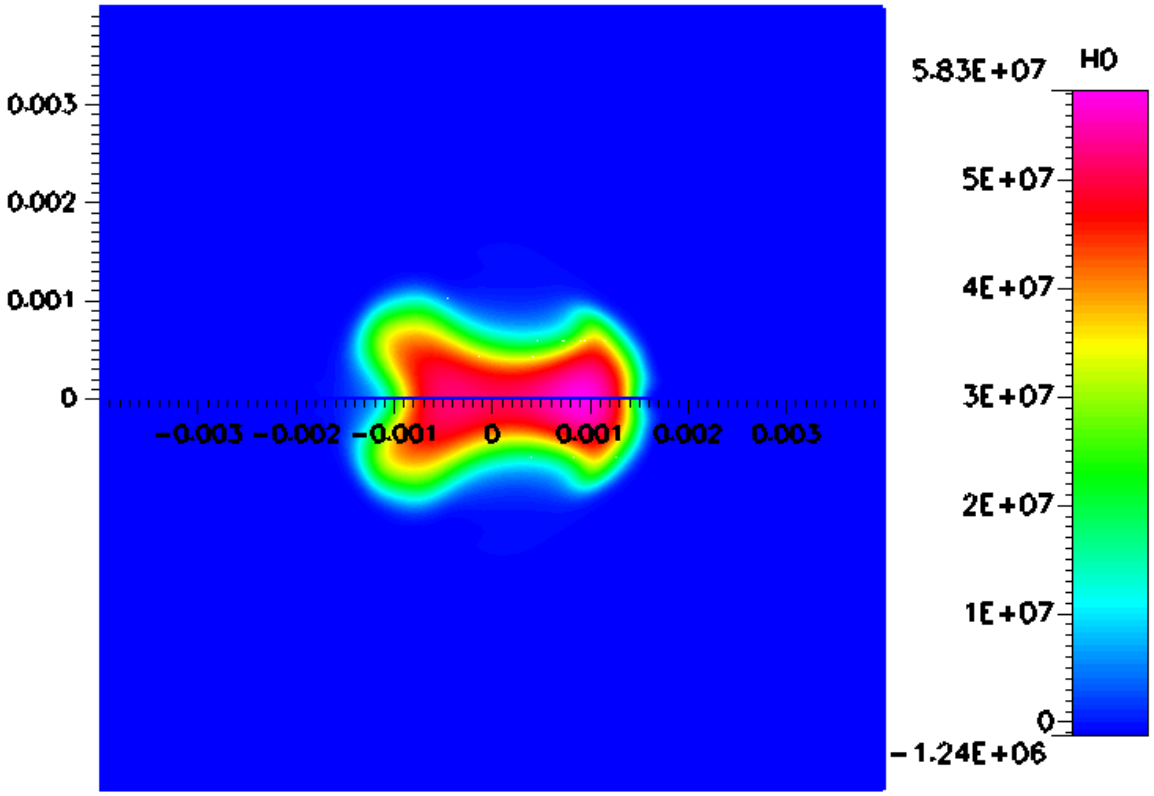

Figure 33: The static enthalpy profile at 2.4 μs. Enthalpy values are in units of J/kg. The distances on the x-axis are in units of meters; the vertical dimension shares the same scale.

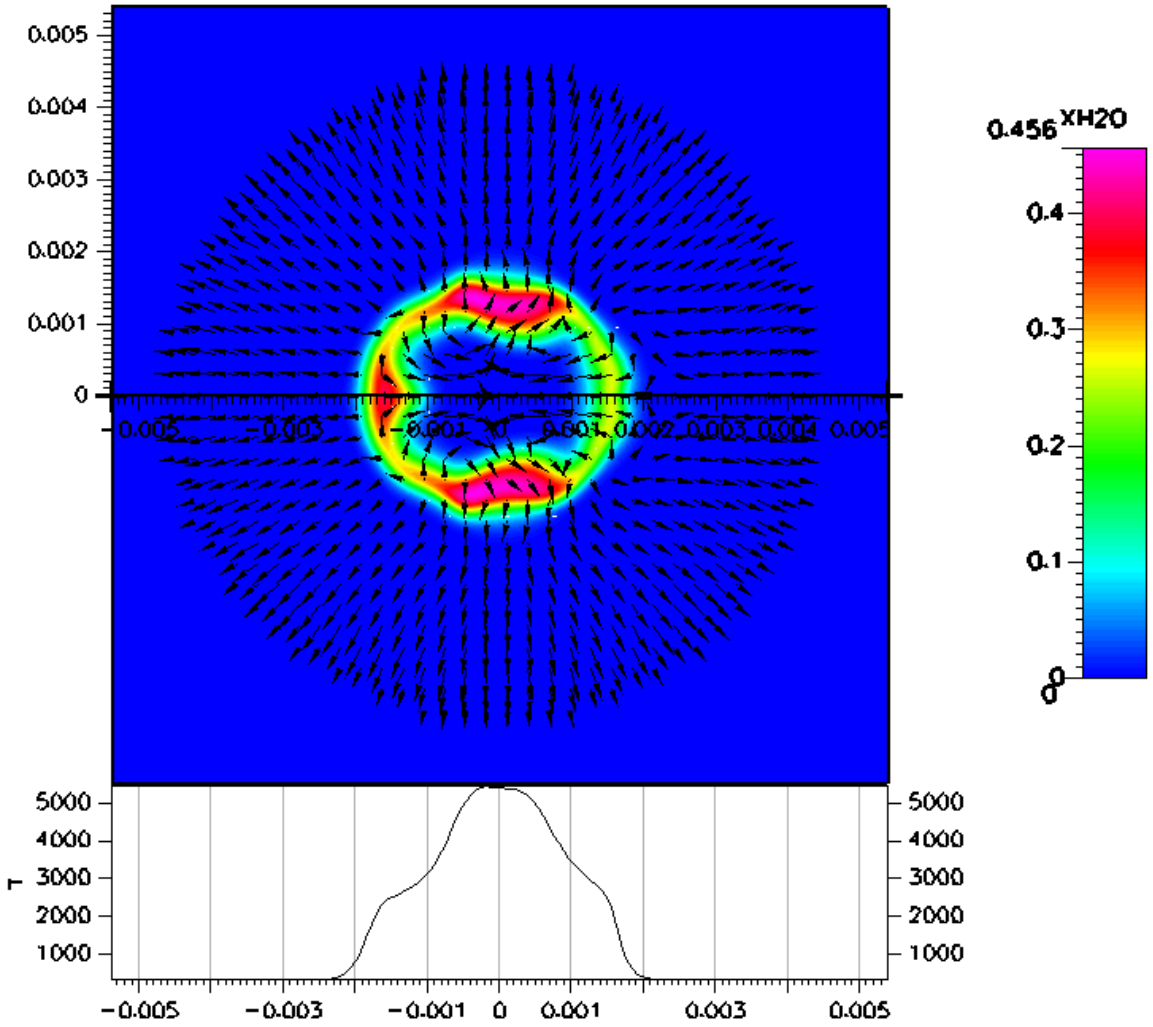

Figure 34: The molar concentration profile of H_2O at 5.6 μs. The bottom graph depicts the temperature along the x-axis in units of Kelvin. The distances on the x-axis and the y axis are in units of meters.

now allows for the formation of H_2O, and the subsequent dominating enthalpy of reaction is added to the flow field. In this manner, the reactions inhibit the total collapse of the kernel. At 32 μs (Figure 35), the kernel has withstood the majority of the collapse. The flame front begins to propagate in all directions except for the right side where the axial collapse still has a velocity of 32 m/s, which is 6 times greater than the flame front velocity. Eventually, as the axial flow weakens, the flame front begins to propagate outward. The deformation of the flame front caused by the unbalanced axial collapse propagates throughout the remainder of the simulation. Figure 36 shows a slight indentation of the flame front on the positive x-axis at 1.0 ms, along with the increased length in the y-direction. The ignition temperature is around 2,500 K.

5.2 Equivalence Ratio Dependence

The variance in the fuel equivalence ratio (ϕ) allows control over the reaction enthalpy source that is dynamically introduced into the flow. For $\phi = 1.0$ shown in the Subsection 5.1, the energy from the reaction is maximized. For a case where $\phi = 0.1$, the energy introduced through reactions is small, and ignition does not occur. For the intermediate $\phi = 0.7$ case, the energy introduced into the flow field from the reaction is not maximized, but ignition still occurs. With the reduced reaction energy source compared with the stoichiometric case, the strength of the collapse becomes a factor for whether ignition is achieved. A strong collapse can flood the flame front with more gas flux than it can process thereby causing blow-out of the flame kernel.

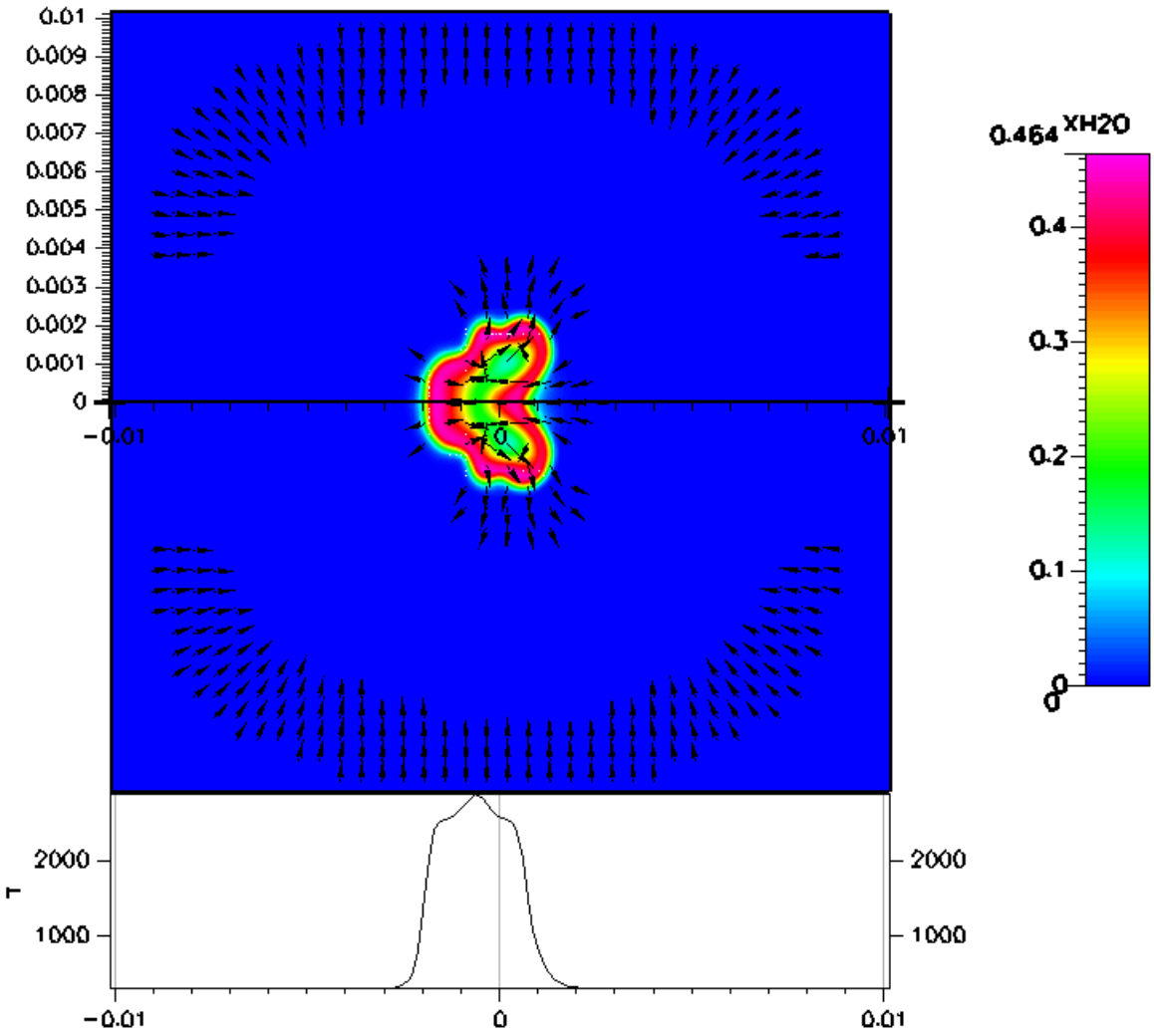

Figure 35: The molar concentration profile of H_2O at 32 μs. The velocity direction field is represented by arrows. The bottom graph depicts the temperature along the x-axis in units of Kelvin. The distances on the x-axis and the y axis are in units of meters.

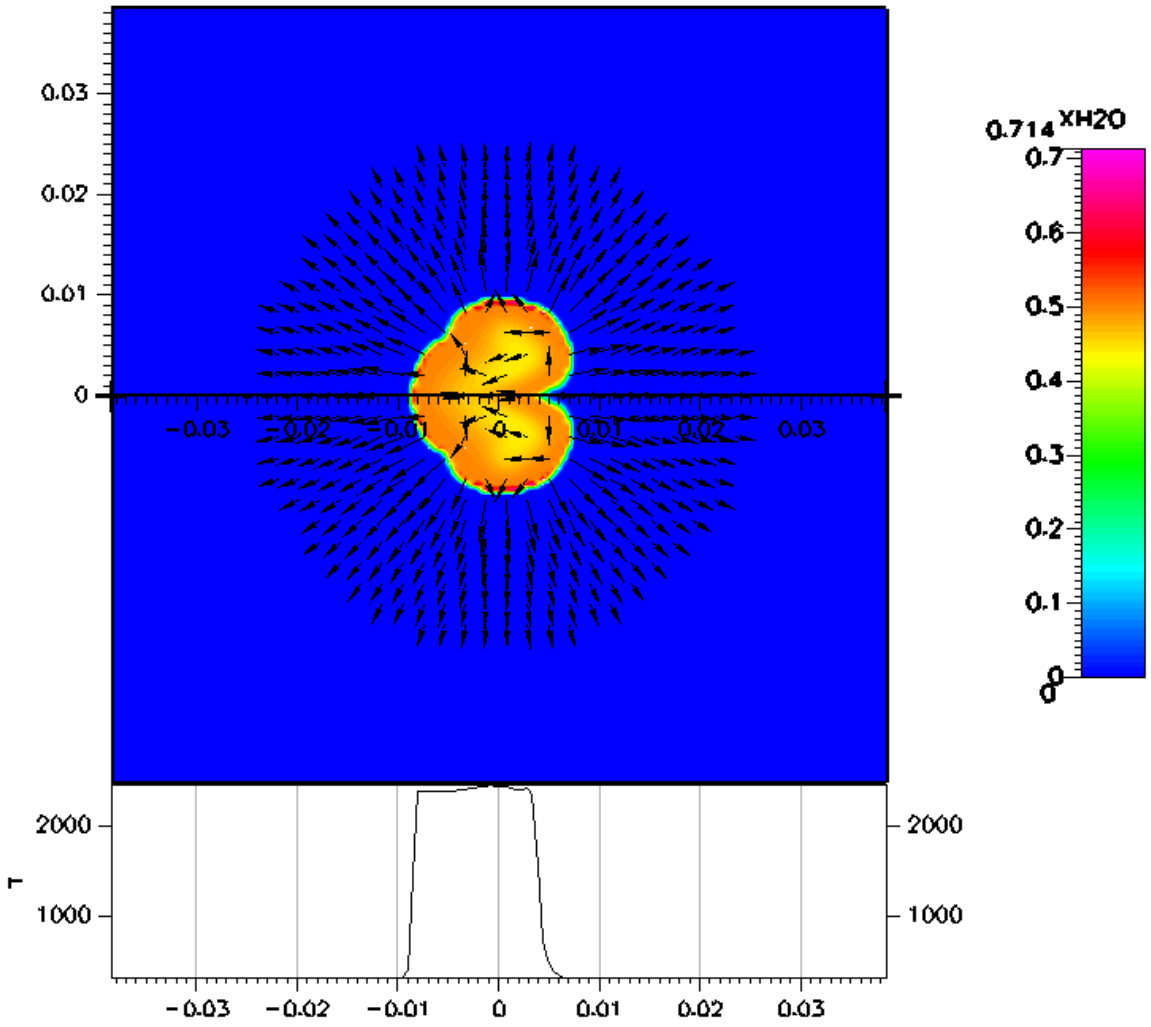

Figure 36: The molar concentration profile of H_2O at 1.0 ms. The velocity direction field is represented by arrows. The bottom graph depicts the temperature along the x-axis in units of Kelvin. The distances on the x-axis and the y axis are in units of meters.

Figures 37, 38, and 39 show the simulated NH concentration, OH concentration, and temperature profiles at 3.2 μs, 10 μs, 32 μs, and 100 μs for $\phi = 0.1$, 0.7, and 1.0, respectively. In all cases, the NH, OH, and temperature profiles are similar at 3.2 μs, with the exception of their size. The mixtures with lower equivalence ratios have smaller profiles due to the differences in the initial pressure profiles (see Subsection 2.2) and their smaller energy of the initial condition. These smaller initial pressures give rise to weaker blast fronts and less expansion of the kernel before separation. Such a reduced initial pressure profile between mixtures of differing ratios will happen in the event of temperature saturation during the laser-induced breakdown. As a result of the assumed temperature profile, differences in the energy of the initial laser sparks are caused by the number of bonds in the NH_3 compared with O_2. The energies of the $\phi = 0.1$, 0.7, and 1.0 initial conditions are 9.3 mJ, 12.3 mJ, and 12.9 mJ, respectively.

At 3.2 μs and 10 μs, the peak in the temperature profiles are shown to be too high for OH formation by the hole in the OH profiles. OH only begins to dominate the center region of the kernel after the peak temperature drop below 3,500 K.

The deformation of the profiles is shown to increase with decreasing ϕ as expected. In the ϕ=0.1 case, the axial flow is seen to compress the temperature and concentration profiles due to the lack of energy of the reaction entering the system. At 100 μs, the blow-out of the flame is evident by the reduced size and temperature of the kernel. Additionally, the temperature profile and kernel dynamic are very similar to that of the laser spark decay in air. For ϕ=0.7, the axial flow to the left has caused a

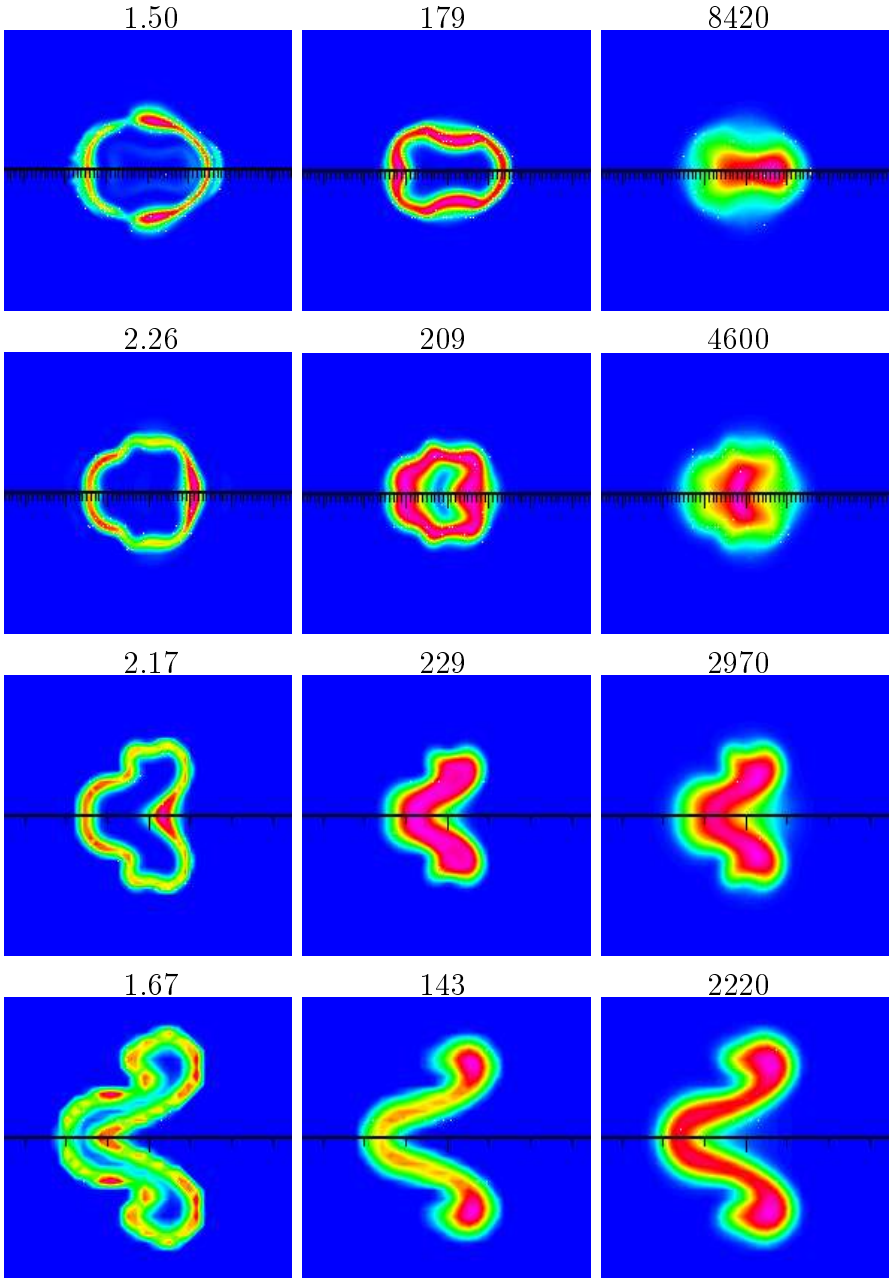

Figure 37: Simulated NH concentration (left), OH concentration (middle), and temperature profiles(right) for laser spark decay in an ammonia-oxygen mixture with an equivalence ratio of 0.1. The boundaries of each picture measures 7 mm square. The rows represent 3.2 μs, 10 μs, 32 μs, and 100 μs, respectively. All values are scaled for each profile to span the entire pseudo-color scale. Peak values are displayed on top of each profile with concentration in units of 10^{21} m^{-3} and temperature in units of Kelvin.

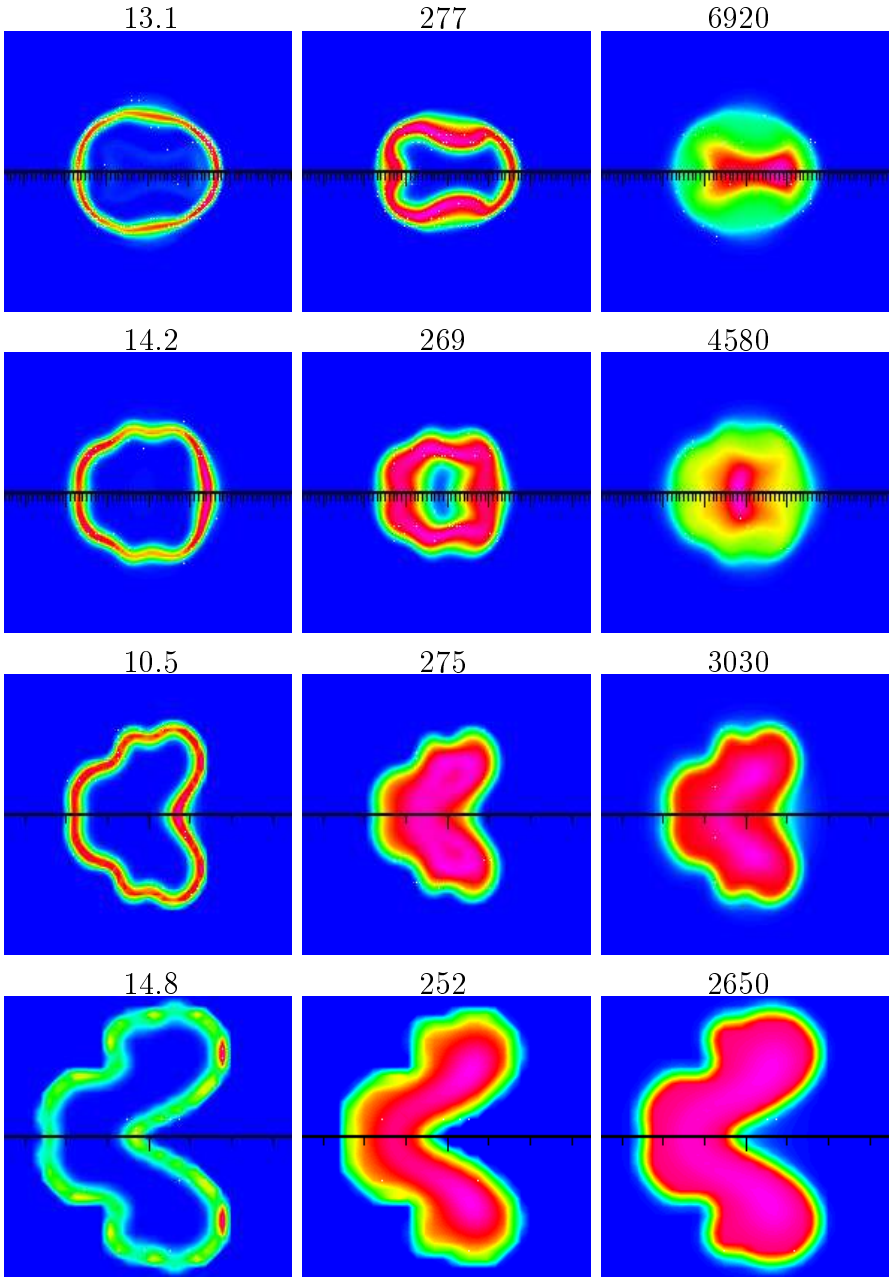

Figure 38: Simulated NH concentration (left), OH concentration (middle), and temperature profiles(right) for laser spark decay in an ammonia-oxygen mixture with an equivalence ratio of 0.7. The boundaries of each picture measures 7 mm square. The rows represent 3.2 μs, 10 μs, 32 μs, and 100 μs, respectively. All values are scaled for each profile to span the entire pseudo-color scale. Peak values are displayed on top of each profile with concentration in units of 10^{21} m^{-3} and temperature in units of Kelvin.

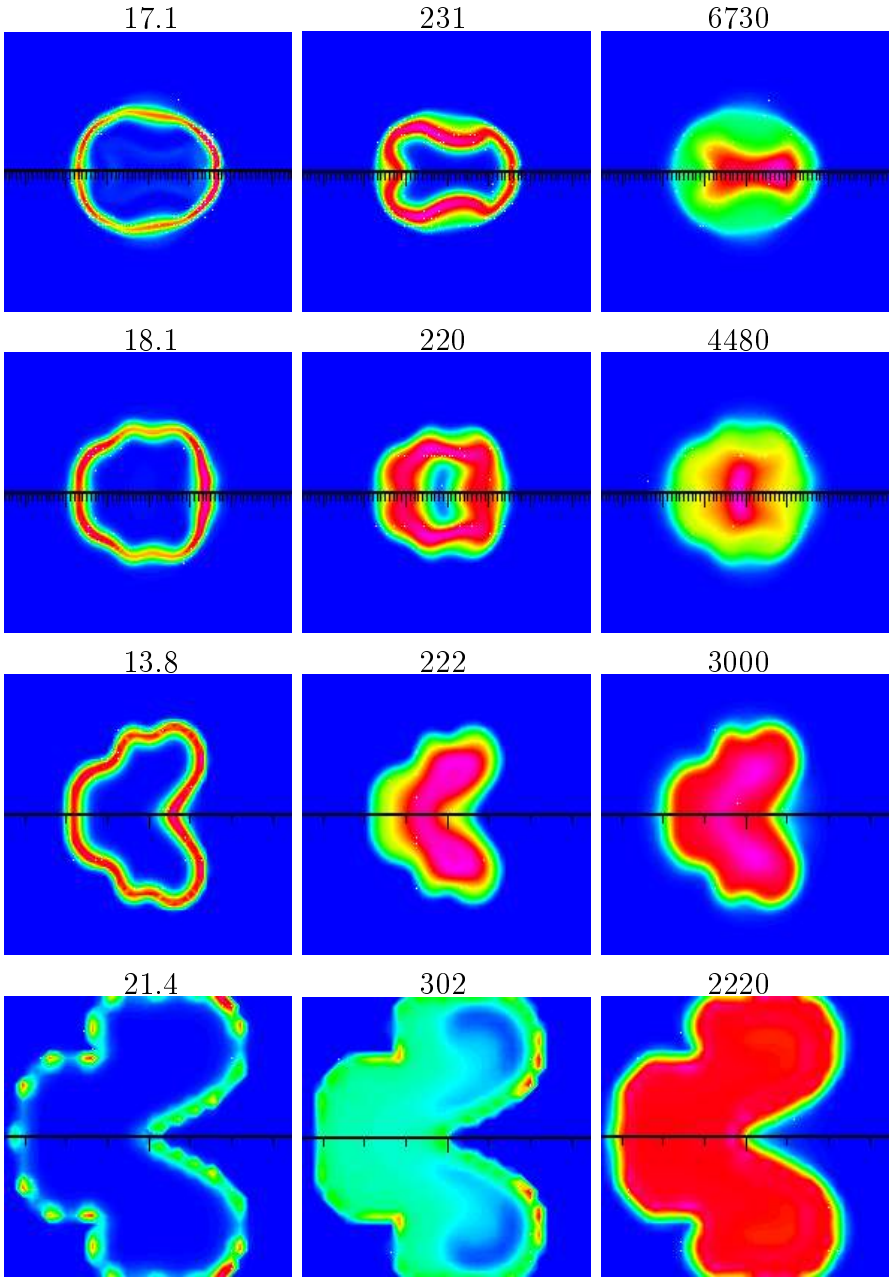

Figure 39: Simulated NH concentration (left), OH concentration (middle), and temperature profiles(right) for laser spark decay in an ammonia-oxygen mixture with an equivalence ratio of 1.0. The boundaries of each picture measures 7 mm square. The rows represent 3.2 μs, 10 μs, 32 μs, and 100 μs, respectively. All values are scaled for each profile to span the entire pseudo-color scale. Peak values are displayed on top of each profile with concentration in units of 10^{21} m^{-3} and temperature in units of Kelvin.

large deformation in the flame front. However, unlike the weaker case, the strength of the reactions are able to sustain the flame front and kernel as the flow field decays. The same phenomena occurs in the ϕ=1.0 case, but the deformation is less severe. In both $\phi = 0.7$ and ϕ=1.0 cases, the deformation is seen throughout the simulation.

5.3 Experimental Comparison

The laser spark simulation results for the $\phi = 0.1$, 0.7 and 1.0 cases are compared with planar laser induced fluorescence (PLIF) measurements of NH and OH concentrations [3, 4, 8, 21]. The profile of the NH concentration allows observation of the flame front deformations caused by the flow field interactions. The OH concentration profile gives additional information on the behavior of the region behind the flame front. The PLIF measurements are performed on laser spark ignition with the breakdown induced by the (f-number=5) focusing of a 10 ns pulse at 1064 nm wavelength. The laser energy deposited by the pulse is measured to be 25 mJ, which is twice that of the simulated laser spark energy deposition. Despite the difference in the energy of the initial laser spark, various similarities exist in the characteristic behaviors of the simulation and experimental measurement.

Figure 40 juxtaposes the measured OH concentration profiles at 3 μs, 10 μs, 30 μs, and 100 μs for fuel equivalence ratios of 0.1, 0.7, and 1.0. The hole in the center of the OH profile at early times agrees well with the simulation, and indicates that the position of the peak kernel temperature are effectively modeled. However, the larger hole in the simulated OH profiles indicate higher temperatures. The redistribution of

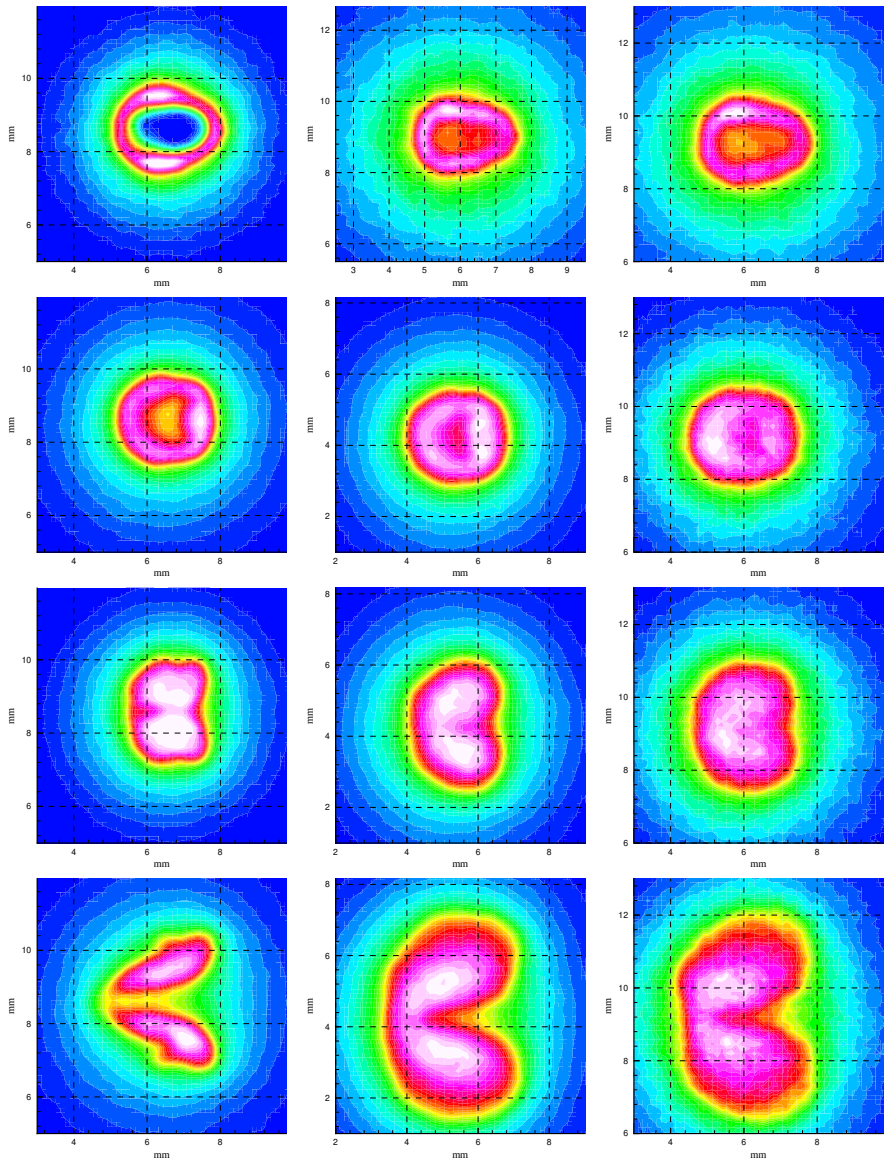

Figure 40: Experimental OH concentration profiles for laser-ignition of ammonia-oxygen mixtures with fuel equivalence ratios of 0.1 (left), 0.7 (middle), and 1.0(right). The boundaries of each picture measures 7 mm square. The rows represent 3 μs, 10 μs, 30 μs, and 100 μs, respectively.[3]

the OH concentration thickness from the top and bottom at 3 μs, to the right and left sides at 10 μs are in agreement with calculations. Unlike the simulation, the profiles between differing equivalence ratios are closer in spatial dimensions through 10 μs.

Figure 41 juxtaposes the measured NH concentration profiles at 3 μs, 10 μs, 30 μs, and 100 μs for fuel equivalence ratios of 0.7, and 1.0. Comparison of the NH and OH profiles indicate the confinement of NH on the periphery of the ignition kernel, and thereby allow the use of NH as a flame front indictor, as expected. The deformation of the NH profile from the horizontally-elongated shape at 3 μs, to a more spherical shape at 10 μs corresponds well to simulations. In both measured and simulated profiles, the NH concentration is seen to flatten on the right side at 10 μs due to flow field interactions.

At 30 μs and 100 μs, the deformation of the NH and OH profiles caused by the flow field are clearly seen. The ϕ=0.1 kernel is shown by the OH profiles to collapse in a manner similar to the non-ignition case, while the other profiles indicate the induction of ignition.

The measured deformation of the profiles is sharper than that of the simulations. The cause of this difference has not yet been determined, but could possibly be due to the factor of two difference in laser spark energy inducing a stronger flow field. Other possible reasons are the limited spatial resolution of the simulation and the reduced 30 step combustion reaction mechanism used.

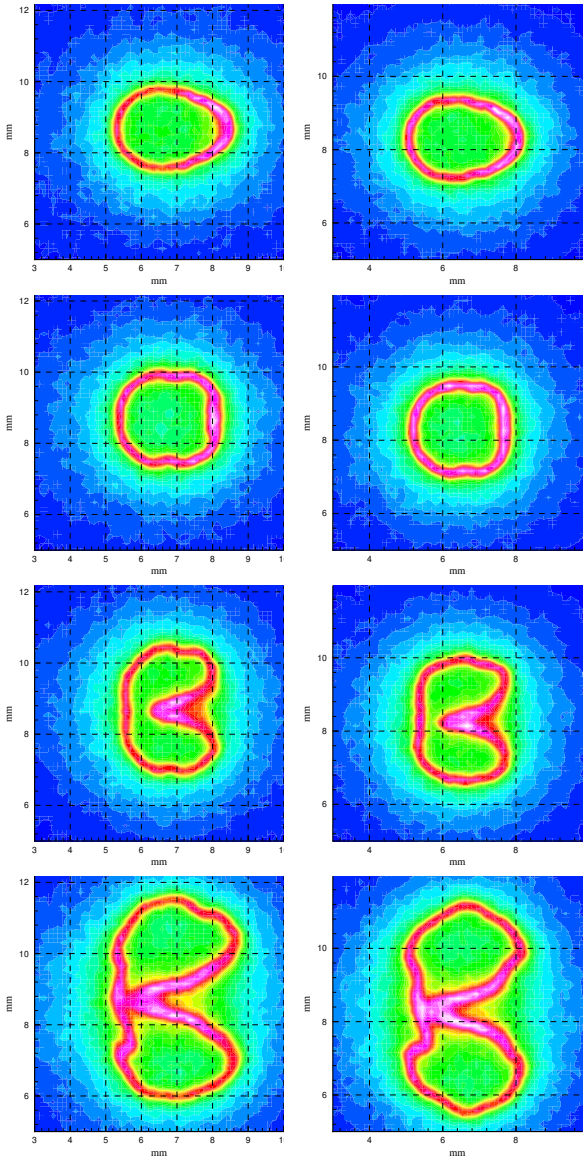

Figure 41: Experimental NH concentration profiles for laser-ignition of ammonia-oxygen mixtures with fuel equivalence ratios of 0.7 (left) and 1.0(right). The boundaries of each picture measures 7 mm square. The rows represent 3 μs, 10 μs, 30 μs, and 100 μs, respectively.[3, 4]

6 Summary

In this dissertation, a model that allows for the time-accurate simulation of laser spark decay in combustible and non-combustible gas mixtures was created. With this model, the fluid dynamics induced during laser spark decay and the cause of the experimentally measured flow patterns characteristic of laser spark decay are explained for the first time.

Due to the high temperatures inherent to laser sparks, thermodynamic and transport properties were extended to cover the 298 K - 35,000 K temperature range, accounting for ionization effects. Additionally, a novel kinetics mechanism, which allowed for the simultaneous modeling of equilibrium plasma and multi-step finite-rate combustion reactions, was devised and implemented. As a result of the kinetics mechanism, the computational model was able to use realistic fluid property values.

A difference in the computational and experimental spark energies arose from the length, width, and saturation temperature imposed on the initial temperature profile of the laser spark. There are several possible reasons for this energy discrepancy, including multiple breakdown locations, diffraction effects, and non-equilibrium concentrations. The existence of multiple breakdown locations along the optic axis has been observed in the breakdown of gases and shown to exist in the locations of peak irradiance caused by spherical aberration effects[20, 21]. The inclusion of such an effect in the temperature profile would increase the saturated locations and thereby increase the corresponding spark energy. It is possible that the coaxial nature of the

multiple breakdown locations will not change the overall cylindrical asymmetry of the laser spark. The diffraction of the laser pulse during the plasma formation, and the multi-mode nature of the non-Gaussian laser-pulse profile, could cause widening of the beam waist and the laser spark. The quantification of these effects should be examined, since it may indicate the requirement of an increased spark width, and thereby an increased spark energy. Lastly, with relaxation times on the order of a picosecond, it is possible that the initial laser spark has a non-equilibrium species concentration. A non-equilibrium plasma would contain an increased concentration of doubly- and triply-ionized species, which would cause a higher spark energy. Due to the possible existence of non-equilibrium, the saturation temperatures measured at delay times of 10 ns by Stricker et al.[22] may not properly describe the temperature saturation.

With the developed computational model, the characteristic fluid phenomena resulting from laser spark decay were related to the characteristics of the laser-induced plasma upon termination of the laser pulse. Specifically, the high peak pressure of the initial spark dominates the decay at early times giving rise to a blast wave. The characteristics of the simulated blast wave were found to be in good agreement with both experimental measurement and the Sedov model. The over-expansion caused during the pressure relaxation was shown to induce a collapse in the kernel region. Due to the geometry of the initial spark, the collapse was shown to be strongest in the direction of the focusing lens, in agreement with experiment. Additionally,

back-to-back vortices forming a ring were simulated during the collapse. This vortex structure was shown to be in agreement with experimental shadowgraphs. In the case of laser spark decay in combustible gaseous mixtures, the deformation of the flame front caused by the asymmetric flow-field during the collapse was simulated and showed many similarities with planar laser induced fluorescence measurements.

In summary, Section 1 introduces the purpose of this work, with a discussion of applications. A description of past electrode and laser spark-decay models was outlined along with the method used in this work.

In Section 2, the temperature profile used to model the laser spark upon termination of the 10 ns laser pulse was presented. The modeling of enthalpy, entropy, specific heat, equilibrium species concentrations, pressure, viscosity, thermal conductivity, and diffusion over the entire temperature range was discussed. The interface limitations placed on these properties by the computational fluid dynamic (CFD) software were presented.

In Section 3, the iterative method used by the CFD software to solve the nominal fluid transport equations was described along with the interfacing of modules designed specific to the modeling of laser spark decay. The choice of the spatio-temporal computational grid was discussed along with the applied initial and boundary conditions.

In Section 4, the results of the laser spark decay simulation in air were presented. The resultant temporal decay of peak temperatures and electron number densities are similar to those measured. Despite a factor of two difference in energy, the simulated

blast wave formation and propagation agreed with experimental measurement within the error bars over the entire temporal range investigated. The kernel dynamics also shows excellent agreement between synthetic and experimental ultra high speed shadowgraphs.

In Section 5, the ability of the model to simulate laser spark ignition of ammonia-oxygen mixtures was verified. The comparison of computed species concentration profiles with planar laser induced fluorescence measurements showed good agreement over all times and fuel equivalence ratios investigated. Additionally, the profile of the initial laser spark at 10 ns was shown to cause the flame front deformations characteristic to laser spark ignition. Specifically, the simulated interactions between the flow field and the combustion reactions are shown to lead to the deformation of the flame front.

In the future, this model should be applied to laser sparks induced by different focusing elements and laser pulses. This requires the development of a systematic way to generate an initial temperature profile given the laser pulse and focusing element specifications. Such a rigorous investigation must more explicitly model the breakdown physics as well as produce time-accurate simulations. With such a model, the optical element and laser pulse used to generate an optimal laser spark for a given application can be computationally determined.

The extension of the model to include other combustible gases such as hydrocarbons is of practical importance. Due to the characteristics of laser sparks in hy-

drocarbon mixtures, such an investigation requires extending the plasma model and thermodynamic properties to higher temperatures and more species. The 18 species limit on the CFD software may require the implementation of a reduced plasma model that relates the overall properties of an ionized gas to a generic gas. Such a reduction in the number of ionic species will allow for more species to be used in the combustion model.

Lastly, as computational speeds increase, this model should be applied to the simulation of multiple, non-coaxial laser spark ignition. Various interesting blast-wave-blast-wave, flame-front-flame-front, and blast-wave-flame-front interactions have been observed in the studies of multiple ignition locations[44]. These interactions can be modeled by extending the computational domain into three-dimensions. Such a computation today would take about 2 years of CPU time on the Silicon Graphics Computer Systems R10000 processor utilized in this investigation.

References

References

[1] Maher I. Boulos, Pierre Fauchais, and Emil Pfender. *Thermal Plasmas Fundamentals and Applications*, volume 1. Plenum Publishing Corporation, New York, New York, first edition, 1994.

[2] Ying-Ling Chen. Private Communications.

[3] Wenhong Qin. Private Communications.

[4] Y. Chen. *Laser-Induced Gas Breakdown and Ignition.* Ph.D. dissertation, The University of Tennessee, 1998.

[5] David R. Lide, editor. *Handbook of Chemistry and Physics.* Fast Computers. CRC Press, Inc., Ann Arbor, MI, seventy-fourth edition, 1993.

[6] E. Gutheil, G. Balakrishnan, and F. A. Williams. Structure and extinction of hydrogen-air diffusion flames. In Norbert Peters and Bernd Rogg, editors, *Reduced Kinetic Mechanisms for Applications in Combustion Systems*, part 11, pages 177–195. Springer-Verlag, New York, New York, first edition, 1993.

[7] V. Ya. Basevich and V. I. Vedeneev. Propagation of a laminar ammonia flame. *Combust. Explos. Shock Waves*, 27:559–564, 1991.

[8] David H. Plemmons. *Laser-Spark Ignition and the NH Radical.* Ph.D. dissertation, The University of Tennessee, 1996.

[9] D. Bradley and F. K-K. Lung. Spark ignition and the early stages of turbulent flame propagation. *Combustion and Flame*, 69:71–93, 1987.

[10] M. Kono, K. Niu, T. Tsukamoto, and Y. Ujiie. "Mechanism of flame kernel formation produced by short duration sparks". In *Twenty-Second Symposium (International) on Combustion*, pages 1643–1649, Pittsburgh, 1988. The Combustion Institute.

[11] Thompson M. Sloane. Numerical simulation of electric spark ignition in atmospheric pressure methane-air mixtures. *Combust. Sci. and Tech.*, 73:367–381, 1990.

[12] T. Kravchik and E. Sher. Numerical modeling of spark ignition and flame initiation in a quiescent methane-air mixture. *Combustion and Flame*, 99:635–643, 1994.

[13] Y. Tanaka and T. Sakuta. Modelling of a pulsed discharge in n_2 gas at atmospheric pressure. *J. Phys. D: Appl. Phys*, 32:3199–3207, 1999.

[14] CFD Research Corporation.

[15] David C. Smith. Laser induced gas breakdown and plasma interaction. *AIAA 38^{th} Aerospace Sciences Meeting & Exhibit*, 2000.

[16] Christian Parigger, Y. Tang, D. H. Plemmons, and J. W. L. Lewis. Spherical aberration effects in lens-axicon doublets: theoretical study. *Applied Optics*, 36(31):8214–8221, 1997.

[17] Guy M. Weyl. Physics of laser-induced breakdown: An update. In Leon J. Radziemski and David A. Cremers, editors, *Laser-Induced Plasmas and Applications*, part 1, pages 1–67. Marcel Dekker, Inc., New York, New York, first edition, 1989.

[18] Robert G. Root. Modeling of post-breakdown phenomena. In Leon J. Radziemski and David A. Cremers, editors, *Laser-Induced Plasmas and Applications*, part 2, pages 69–103. Marcel Dekker, Inc., New York, New York, first edition, 1989.

[19] C. Grey Morgan. Laser-produced plasmas. In Joseph M. Proud and Lawrence H. Luessen, editors, *Radiative Processes in Discharge Plasmas*, pages 457–507, New York, June 1985. NATO Advanced Study Institute on Radiative Processes in Discharge Plasmas, Plenum Press.

[20] C. Grey Morgan. laser-induced breakdown of gases. *Rep. Prog. Phys.*, 38:621–665, 1975.

[21] Y.-L. Chen, J.W.L. Lewis, and C. Parigger. Spatial and temporal profiles of pulsed laser-induced air plasma emissions. *JQSRT*, 67(2):91–103, 2000.

[22] J. Stricker and J. G. Parker. Experimental investigations of electrical breakdown in nitrogen and oxygen induced by focused laser radiation at 1.064 μ. *J. Appl. Phys.*, pages 851–855, 1982.

[23] G. Baravian, J. Godart, and G. Sultan. Multiphoton ionization of molecular nitrogen by a neodymium-glass laser. *Phys. Rev. A*, 25:1483–1495, 1982.

[24] R.L. Taylor and G. Caledonia. Experimental determination of the cross-sections for neutral bremsstrahlung. *J. Quant. Spectrosc. Radiat. Transfer*, 9:681–696, 1969.

[25] I. Dors, C. Parigger, and J.W.L. Lewis. Fluid dynamic effects following laser-induced optical breakdown. *AIAA 38th Aerospace Sciences Meeting & Exhibit*, 2000.

[26] Charlotte E. Moore. *Atomic Energy Levels*, volume 1 of *The Art of Computer Programming*. U.S. Government Printing Office, Washington, D.C., 15 June 1949.

[27] CFD Research Corporation, Huntsville, AL. *CFD-ACE Theory Manual*, 5 edition, October 1998.

[28] Sanford Gordon and Bonnie McBride. "Computer Program for Calculation of Complex Chemical Equilibrium Compositions and Applications". Technical Report Reference Publication 1311, NASA, 1994.

[29] Richard L. Burden, J. Douglas Faires, and Albert C. Reynolds. *Numerical Analysis*. PWS Publishers, Boston, Massachusetts, second edition, 1981.

[30] C. R. Wilke. A viscosity equation for gas mixtures. *J. Chem. Phys.*, 18(4):517–519, 1950.

[31] P. J. VanDoormal and G. D. Raithby. Enhancements of the simple method for predicting incompressible fluid flows. *Numerical Heat Transfer*, 7(2):147–163, 1984.

[32] R. J. Kee, J. F. Grcar, M. D. Smooke, and J. A. Miller. "A FORTRAN program for modeling steady one dimensional flames". Technical Report SAND85-8240, Sandia National Laboratories, 1985.

[33] Geoffrey Taylor. The formation of a blast wave by a very intense explosion. *Proc. Roy. Soc. A*, 201:175–186, 1950.

[34] L. I. Sedov. *Similarity and Dimensional Methods in Mechanics*. Academic Press, New York, New York, second edition, 1959.

[35] Harold L. Brode. Blast wave from a spherical charge. *Phys. Fluids*, 2(2):217–229, 1959.

[36] S. A. Bystrov, D. A. Mazalov, A. F. Filippov, and F. V. Shugaev. Dynamics of shock waves during optical breakdown in the plasma of a non-self-maintained discharge. *Plasma Physics Reports*, 24(1):32–39, 1998.

[37] V. Svetsov, M. Popova, V. Rybakov, V. Artemiev, and S. Medveduk. Jet and vortex flow induced by anisotropic blast wave: experimental and computational study. *Shock Waves*, 7:325–334, 1997.

[38] Z. Jiang, K. Takayama, K. P. B. Moosad, O. Onodera, and M. Sun. Numerical and experimental study of a micro-blast wave generated by pulsed-laser beam focusing. *Shock Waves*, 8:337–349, 1998.

[39] H. Steiner and W. Gretler. The propagation of spherical and cylindrical shock waves in real gases. *Phys. Fluids*, 6:2154–2164, 1994.

[40] H. Steiner, W. Gretler, and T. Hirschler. Numerical solution for spherical laser-driven shock waves. *Shock Waves*, 8:139–147, 1998.

[41] A. Loeb, M. Loebenstein, A. Lubmirsky, E. Eliezer, S. Maman, and Y. Gazit. Point explosion simulation by fast spark discharges. *J. Appl. Phys.*, 57(7), 1985.

[42] D. Nassif and L. Huwel. The influence of gas pressure and laser power on the dissipation of laser generated sparks. *submitted J. Appl. Phys.*, 1999.

[43] A. S. Dubovik. *Photographic Recording of High-Speed Processes*. Pergamon Press, New York, New York, first edition, 1968.

[44] I.G. Dors, C. Parigger, J.W.L. Lewis, and Y. Chen. Investigation of laser-induced shock-wave interactions. *OSA Annual Meeting*, 1998.

Vita

Ivan G. Dors was born on 16 October 1974 in Manchester, NH. He grew up in Bow, NH and graduated from Bishop Brady High School in June of 1992. In the fall of 1992 he entered The University of New Hampshire (UNH). Starting in his sophomore year he worked part time as a laboratory assistant at the Space Science Group of the UNH Institute for the Study of Earth, Oceans, and Space. During his tenor with the Space Science Group he contributed to the development of energetic particle analyzers for the ACE and Cluster satellites. In May of 1996, he completed his bachelor of science degree with a major in physics, university honors in physics, and a minor in applied mathematics. The following August he accepted a research assistantship at The University of Tennessee (UT) Space Institute Center for Laser Applications (CLA). In May of 1998 he earned a master of science degree in physics with a thesis entitled, "Experimental Investigations of Aluminum Monoxide in the Laser Ablation of Alumina". Following his masters degree, he remained at CLA investigating laser spark ignition modeling and was awarded a Space Grant Fellowship in August of 1999. In August of 2000, he earned a doctor of philosophy degree in physics at UT.